UNIVERSITAT DE BARCELONA

Procedures for improved weather radar data quality control

Patricia Altube Vázquez

Procedures for improved weather radar data quality control

Author
Patricia Altube Vázquez

Ph.D Thesis
Universitat de Barcelona

Supervisors
Joan Bech Rustullet
Tomeu Rigo Ribas

Cover designer

Garazi de Ayala Barguilla

Ph.D Thesis

Procedures for improved weather radar data quality control

Author

Patricia Altube Vázquez

Supervisors

Joan Bech Rustullet

Tomeu Rigo Ribas

Tutor

Maria Rosa Soler Duffour

September, 2016

University of Barcelona

Program of Ph.D in Physics

Dept. of Applied Physics

This Ph.D dissertation has been carried on under the framework of the Industrial Doctoral Programme, co-funded by the Autonomous Government of Catalonia (Generalitat de Catalunya) and the Meteorological Service of Catalonia (Servei Meteorològic de Catalunya).

Agradecimientos

"Lo importante es reír. Y reír juntos."
Eduardo Galeano, *El libro de los abrazos*

Aunque esta tesis ha sido escrita para la ciencia he querido llenar esta sección de subjetividad. Porque pese a los inevitables momentos difíciles, en estos años de doctorado me he divertido, he disfrutado y he sido muy feliz. Y esto ha sido posible gracias a todas las personas (y animales) increíbles con las que he tenido la suerte de contar incondicionalmente.

A ellas va dedicado este trabajo y todo mi cariño.

He desarrollado esta tesis con el equipo de teledetección del Servei Meteorològic de Catalunya, formado por tres compañeros excepcionales: *Nico Pineda*, *Oriol Argemí* y *Tomeu Rigo*. Desde la Universidad de Barcelona, he contado con la guía y el apoyo incansables de *Joan Bech*, probablemente el mejor supervisor del mundo. Gracias por vuestro tiempo y conocimiento, vuestra paciencia y confianza. Haberos conocido y haber compartido casi cada día de estos años es lo más importante que me llevo. He tenido además la gran suerte de coincidir con *Carles Cayuela* y *Anna del Moral*; gracias por compartir conmigo mucho, mucho más que "99 little bugs in the code". Gracias también a *Mercé Herrero*, *Agnés Mestre*, *Roger Pujolar*, *Isabel Martínez*, *Carme Farnell*, *Montse Aran*, *Helen Sansegundo* (y muchos más), quienes hacen del SMC un lugar más divertido y mejor. Mil viajes con la R3 valen la pena por trabajar con todos vosotros. Moltes gràcies, companys!

A *Laura Trapero* a *Josep Ramón Miró*, a *Xavier Ortiga* y a *Marc Berenguer*, quienes altruistamente han dedicado un pedacito de su tiempo, conocimiento y experiencia a este trabajo: gràcies!

During a brief research stay in 2015 I had the opportunity to work together with *Scott Collis* and *Jonathan Helmus* within their great team in Argonne National Laboratory (Illinois). It has been an awesome experience. Thank you all sincerely

for the time you spent teaching and helping me and for the encouragement, which I took back home. Beyond the science, I am wholeheartedly thankful to *Scott* and *Louise Collis*, and to *Katrina* and *Kenny Errant* for the warm welcome and for taking so good care of me so far from home.

Han sido tres años entre Barcelona, Torelló y Vitoria. Pero las distancias son pequeñas cuando no se cuentan en kilómetros. A tota la *colla d'esponges de Torelló*, que són molts però tots genials, gràcies per acollir-me com a una més, per donarme el vostre afecte cada dia i per la diversió! A los tres mosqueteros, mi hermano *Alex Altube*, mi primo *Sergio Cruz* y el insondable *Diego Román*, gracias por dejar de lado vuestros planes para compartir juntos, siempre, la vuelta a casa. Gracias a los mejores amigos y embajadores del mundo, *Sara Ruiz Arrugaeta*, *Nerea López de Lacalle*, *Hugo Feijoó*, *Marievi Souti*, *Irati Rodríguez*, *Gloria de las Heras* y *Raúl Nistal*; un breve encuentro con vosotros da vida. Y a *Garazi de Ayala*, que llena los momentos de arte, que escucha con mucho más que un oído atento, que viene de visita desafiando las leyes del espacio y del tiempo, a través de nuestro vínculo mágico: milesker!

En las largas horas de trabajo en casa... gracias a las pequeñas *Sake* y *Gin* por la compañía y la ayuda inestimable destrozando documentos irrelevantes, despejando la mesa de molestos bolígrafos y vasos, sesteando en el teclado y ¡ronroneando en mi barriga!

Un agradecimiento muy especial a *Jesús Picón*, compañero de vida, por muchos años llenos de viajes, música, baile, sonrisas, gamberradas y risas sin control. Estamos hechos de nubes y contigo todo es posible: $1 + 1 > 2$. Maite zaitut!

Y a quienes debo todo, mis padres *Begoña Vázquez* y *Jesús Altube*, que me guardaron el mes de abril. Gracias amatxu por entender más allá de palabras incomprensibles, por la fuerza y el apoyo sin condiciones. Gracias Su, aita, por la calma y la paciencia infinitas, por enseñarme a pensar; esta tesis es de los dos.

Abstract

Weather radar data and its downstream products are essential elements in weather surveillance and key parameters in the initialisation and validation of hydrological and meteorological models, among other downstream applications. Following the quality standards established by the European and global weather radar networking referents, the present thesis aims for the improvement of the base data quality control in the regional weather radar network operated by the Meteorological Service of Catalonia, the XRAD. This objective is accomplished through the analysis, development and implementation of new or existing procedures and algorithms for radar data quality assessment and improvement. Attending to the current radar technology and to the already implemented quality control procedures for the XRAD, the work is focused on the continuous evaluation of the radar system calibration status and on the correction of Doppler velocity data. The quality control algorithms and recommendations presented are easily translatable to any other operative weather radar networking environment.

A Sun-based, fully automatic procedure for online monitoring the antenna alignment and the receiver chain calibration is adapted and operationally implemented for the XRAD. This Sun-monitoring technique was developed at the Royal Netherlands and Finnish Meteorological Institutes and is included in the quality control flow of numerous weather radar networks around the world. The method is modified for a robust detection and characterisation of solar interferences in raw data at all scan elevations, even when only data at relatively short ranges is available. The modified detection algorithm is also suitable for detecting interferences from wireless devices, which are stored for monitoring their incidence in the XRAD. The solar interferences detected, in turn, are input observations for the inversion of a two-dimensional Gaussian model that yields estimates of the calibration parameters of interest. A complete theoretical derivation of the model establishes its validity limits and provides analytical estimates of the effective solar widths directly from radar parameters. Results of application of this Sun-monitoring methodology to

XRAD data reveal its ability to determine the accuracy of the antenna pointing and to detect changes in receiver calibration and radar system operation status.

In order to facilitate the usage of the Sun-monitoring technique and the interpretation of its estimates, the methodology is reproduced under controlled conditions based on the distributions of solar observations collected by two of the XRAD radars. The analysis shows that the accuracy of the estimated calibration parameters is conditioned by the precision, number and distribution of the solar observations which constitute key variables that need to be controlled to ensure reliable estimates. In addition, the Sun-monitoring technique is compared under actual operative conditions with two other common techniques for quantifying the antenna azimuth and elevation pointing offsets. Pointing bias estimates gathered in a dedicated short-term campaign are studied in a direct inter-comparison of the methods that reflects the advantages and limitations in each case. The analysis of the bias estimates reported by the methods in the course of a one-year period reveals that the performance of the techniques depends on the antenna position at the time of the measurement. After this study, a reanalysis of the Sun-monitoring method results is proposed, which allows to additionally quantify the antenna pedestal levelling error.

Finally, a post-processing, spatial image filtering algorithm for identification and correction of unfolding errors in dual-PRF Doppler velocity data is proposed. The correction of these errors benefits the usage of radar velocity data in downstream applications such as wind-shear and mesocyclone detection algorithms or assimilation in numerical weather prediction models.The main strengths of the proposed algorithm, in comparison with existing correction techniques, are its robustness to the presence of clustered unfolding errors and that it can be employed independently of post-processing dealiasing algorithms. By means of simulated dual-PRF velocity fields, the correction ability of the algorithm is quantitatively analysed and discussed with particular emphasis on the correction of clustered errors. The quality improvement in real dual-PRF data brought out by the new algorithm is illustrated through application to three selected severe weather events registered by the XRAD.

List of Acronyms

ACA	Agència Catalana de l'Aigua (Catalan Water Agency)
ADC	Analog-to-Digital Converter
AEMET	Agencia Estatal de Meteorología (Spanish Meteorological Agency)
ANL	Argonne National Laboratory
AP	Anomalous Propagation
ARM	Atmospheric Radiation Measurement program
CCOR	Clutter Correction
CDV	Creu Del Vent radar
CNAF	Centro Nacional de Asignación de Frecuencias (National Frequency Assignment Chart)
CRAHI	Centre de Recerca Aplicada en Hidrometeorologia (Center of Applied Research in Hydrometeorology)
CSAPR	C Scanning ARM Precipitation Radar
CSR	Clutter-to-Signal Ratio
DFS	Dynamic Frequency Selection
DFT	Digital Fourier Transform
DGTEL	Dirección General de Telecomunicaciones (General Telecommunications Management)
DRAO	Dominion Radio Astrophysical Observatory
DSD	Drop Size Distribution
DTEM	Digital Terrain Elevation Model
EHIMI	Hydrometeorological Integrated Forecasting Tool
EI	Efficiency Index

FFT	Fast Fourier Transform
FWHM	Full Width at Half Maximum
IF	Intermediate Frequency
IFD	Intermediate Frequency Digitiser
IP	Internet Protocol
IQR	Inter-Quartile Range
LLS	Linear Least Squares
LMI	La Miranda radar
LNA	Low Noise Amplifier
MAD	Median Absolute Deviation
MAFRAD	Mòdul d'Anàlisi de Funcionament de Radar (Radar Operation Analysis Module)
NWP	Numerical Weather Prediction model
OPERA	Operational Programme for Exchange of weather Radar information
PBE	Puig Bernat radar
PDA	Puig D'Arques radar
PDI	Programa de Doctorat Industrial (Industrial Doctoral Program)
PLC	Power Logic Control
PLL	Phase Lock Loop
POD	Probability Of Detection
POFD	Probability Of False Detection
PPI	Plan Position Indicator
PRF	Pulse Repetition Frequency
PRT	Pulse Repetition Time
QPE	Quantitative Precipitation Estimate
RF	Radio Frequency
RLAN	Radio Local Area Network
RMSD	Root Mean Squared Deviation
SFU	Solar Flux Units

SMC	Servei Meteorològic de Catalunya (Meteorological Service of Catalonia)
SNR	Signal-to-Noise Ratio
SQI	Signal Quality Index
STALO	STAble Local Oscillator
TCP	Transmission Control Protocol
TOA	Top Of the Atmosphere
TWT	Travelling Wave Tube
UB	Universitat de Barcelona (University of Barcelona)
UPC	Universitat Politècnica de Catalunya (Polytechnic University of Catalonia)
UPS	Uninterrupted Power Supply
UTC	Coordinated Universal Time
VRG	Vertical Refractivity Gradient
WAN	Wide Area Network
WAS	Wireless Access System
WLAN	Wireless Local Area Network

Contents

III RESULTS

Part I

Introduction

1

Motivation and framework

The characteristics of precipitation such as type, rate, amount, distribution, frequency and duration constitute key aspects to understand and feature climate and weather (Kunkel et al., 1999; Trenberth, 2011; Schneider et al., 2014). The freshwater availability, indispensable for the sustainability of life, is directly determined by the spatiotemporal distribution of precipitation. In effect, precipitation is a fundamental link between the water, energy and bio-geochemical cycles of the Earth. From an anthropocentric perspective, efficient management of water resources for socio-economical purposes requires accurate typification of the characteristics of precipitation. At the same time, extreme precipitation events (floods, droughts, hurricanes, hailstorms and landslides for instance) have a significative socioeconomic and environmental impact (Futrell et al., 2005; NRC, 2010; Botzen et al., 2010; Llasat et al., 2013). It is therefore a straightforward consequence that climatology, meteorology and hydrology sciences have historically focused on the observation and measurement of precipitation.

Direct measurement of the amount of precipitation is possible by means of ground based and localised rain-gauges (Frei and Schär, 1998; Yatagai et al., 2012). Rain gauges have been traditionally the choice tool for precipitation measurement mainly in hydrology applications. In addition, disdrometers allow the in-situ measurement of precipitation rate and type. However, these point measurements, even if accurate, are hardly representative for the estimation of precipitation over larger regions, due to the high spatial and temporal variability of precipitation characteristics and to the potential complexities of the surrounding terrain. Rain gauge data merging in networks improves coverage and representativeness but the network

resolution required for hydrological applications may be difficult to achieve (Berne and Krajewsky, 2013). As a counterpoint to the limited spatiotemporal resolution of the rain gauge networks, the weather radar has developed and consolidated as a complementary measurement tool for monitoring, characterisation and estimation of precipitation with high resolution and coverage (Steiner et al., 1999).

Weather radars are active remote sensing instruments that estimate precipitation rate based on the electromagnetic properties of the hydrometeors. Although the main purpose of weather radar systems is real-time weather surveillance and precipitation monitoring, the high resolution data provided and its downstream products are well suited for a wide variety of further applications (Atlas, 1990; Collier, 1996; Meischner, 2004). For instance, weather radar products have been used to develop convective storm structure tracking and short-term precipitation forecasting (nowcasting) techniques (Bellon and Austin, 1978; Browning and Collier, 1989; Dixon and Wiener, 1993; Pierce et al., 2004; Koistinen et al., 2004; Germann et al., 2009; Rigo et al., 2010; Rigo and Llasat, 2016). These precipitation nowcasting techniques based on radar measurements allow to generate key data for initialisation of distributed hydrological models, contributing to the improvement of flash flood forecasting, warning and control (Berenguer et al., 2005; Moore et al., 2005; Vivoni et al., 2006; Collier, 2007; Atencia et al., 2010). In addition, weather radar precipitation and wind products constitute high resolution input observations of high value in the assimilation process for initialisation of Numerical Weather Prediction (NWP) models (Rossa, 2000; Macpherson et al., 2004; Sun, 2005; Magaldi et al., 2009). Moreover these radar products are also valuable for verification and validation of the forecasts by NWP models and general circulation models (see Collier, 1993, for instance). It is, however, a well-known issue and a relevant question that, given the remote nature of radar estimates, primary weather radar data and downstream products are affected by various error factors (Wilson and Brandes, 1979; Zawadzki, 1984; Villarini and Krajewski, 2010). Exhaustive quality control of weather radar data and characterisation of the uncertainty of radar products are of major importance for their appropriate interpretation and use in the aforementioned applications and require accurate knowledge of the origin, nature and spatiotemporal structure and correlation of the errors in each case (Michelson et al., 2004; Holleman et al., 2006).

Attending to the requirements of weather radar data applications, the simultaneous processing and merging of data from several individual radars in composite products is advantageous for enlarging the coverage, homogenising the resolution, reducing the random error and improving the data quality of radar measurements

(Chandrasekar and Jayasumana, 2001; Berne et al., 2005; Chandrasekar and Lim, 2008). Indeed, thanks to the development of communication systems that allow long-range and high rate data exchange, deployment of weather radars in operational regional and national networks has became common practice all around the world in the few last decades. The data center of a weather radar network receives, in quasi-real time, large amounts of data which need to be efficiently managed and archived. As pointed out in Lakshmanan et al. (2006), compositing data from the different radars in the network requires quality proofed, inter-calibrated and harmonised data in a first instance. At this regard, both the OPERA programme (Operational Programme for the Exchange of weather RAdar information) within the EUMETNET framework (OPERA, 1999) and the BALTRAD project in the Baltic Sea region (BALTRAD, 2008) constitute exemplary instances of modern radar networking. The OPERA programme manages data from a total of 226 radars operating in 31 member states in Europe, with the aim of routinely generating and distributing weather radar composite products at the European scale, providing quality information and facilitating the harmonisation and the operational exchange of radar volume data (Köck et al., 2000). On a smaller spatial scale, BALTRAD is a partnership project in which currently 13 weather services and institutions from 10 different countries around the Baltic Sea are involved. BALTRAD weather radar network operates in real-time, exchanges data among members of the partnership and generates products using a common *toolbox* of data processing algorithms that is open-source and world-wide available for application.

The present thesis builds upon the framework of al regional weather radar network, established in the Northeastern area of the Iberian Peninsula and operated by the Meteorological Service of Catalonia (SMC), and aims for the proposal, development, implementation and analysis of standards of observational and quality control and correction practices that follow and complement those established by the aforementioned European referents.

1.1 Weather radar fundamentals

Conventional weather radars transmit microwave signal pulses and measure the power of the signal backscattered by the hydrometeors (raindrops, snowflakes, hailstones and cloud droplets) encountered by the emitted pulse in its propagation through the atmosphere. Weather radars transmit radiation at a fixed wavelength typically between 1 cm and 10 cm. These wavelengths are around 10 times the di-

ameters of the targets so that the backscattering mechanism lies in the Rayleigh regime. Radar measurements are remote in what the measured pulse echo power depends on the electromagnetic properties of the scattering targets, on the measurement setup and on the characteristics of the radar system itself. All these contributions are quantified in the so-called weather radar equation (*cf.* Probert-Jones, 1962; Doviak and Zrnič, 1984) which connects the mean return power from a range r from the radar, $\overline{p}(r)$, with the radar reflectivity factor z (which, for concision, will henceforth be referred to as reflectivity):

$$\overline{p}(r) = \frac{\pi^3 c|K|^2}{2^{10}\ln 2}\,\frac{p_t\tau}{\lambda^2}\,\frac{l^2}{r^2}\,g^2\theta\phi\,z\,, \tag{1.1}$$

where l is a loss factor accounting for the total attenuation of the signal along its path through the atmosphere and $|K|$ is a refraction coefficient related to the complex refraction index of the hydrometeors. It is common in the weather radar literature to express the radar equation in abbreviated form by means of the radar constant C, which encompasses all constants and radar parameters such as the transmitted peak power p_t, the pulse duration τ, the wavelength λ, the antenna gain g and the 3 dB antenna beamwidths in azimuth ϕ and elevation θ:

$$\overline{p}(r) = l^2 C\frac{|K|^2}{r^2}z\,. \tag{1.2}$$

The z reflectivity factor contains only the contributions to the measured power that are related to the backscattering characteristics of the hydrometeors and that are of meteorological relevance, and may be defined in terms of the Drop Size Distribution (DSD) within the radar sample volume (Battan, 1973). The rain rate R, which is the input variable for most weather radar downstream applications, is estimated from the reflectivity Z in dBZ units through a power law relationship (Marshall and Palmer, 1948; Smith and Krajewski, 1993; Torres et al., 1998):

$$Z = 10\log_{10}(z) = aR^b\,, \tag{1.3}$$

where this Z-R relationship may be parametrised depending on the local climatology and on the type and spatiotemporal scale of the precipitation (refer to Battan, 1973; List, 1988; Uijlenhoet, 2001, for instance).

Doppler weather radars, measure, besides the backscattered power, the phase shift between consecutive return pulses in order to provide estimates of the mean radial velocity (V) and the standard deviation of the distribution of the velocities

(i.e. the spectrum width, W) of the targets within the sample volume (Doviak and Zrnič, 1984). Traditionally, the quantities Z, V and W have been referred to as base radar data. Furthermore, the most modern and rapidly spreading operational Doppler radar technology also incorporates polarimetry capabilities. Polarimetric Doppler radars control the polarisation of the transmitted pulses and are capable to detect the return signal in two or more polarisation states, providing estimates of additional variables such as the differential reflectivity and the differential phase, the co-polar correlation coefficient and the linear depolarisation ratio (Bringi and Chandrasekar, 2001), which can also be regarded as base radar data. Polarimetric variables carry relevant information that has proven useful for identifying different precipitation types (rain, hail, graupel, snow) and for improving the quality of quantitative rain estimates (Zrnic and Ryzhkov, 1999; Illingworth, 2003).

Most operational weather radars incorporate a mechanically steered antenna and the microwave pulses are continuously emitted while the antenna is in motion. The range from which the backscattered echo is detected is determined in the radar processor based on the time lapse between the pulse emission and reception. In the case of ground-based radars, the antenna usually performs azimuthal scans at several fixed elevation angles to generate a series of polar maps of base radar data. With this setup, a wide atmospheric volume around a ground-based radar site is probed with a typical scanning duty-cycle or revisit time that lasts from 2 to 10 minutes, and even up to 15 minutes (Bech et al., 2004; Figueras i Ventura and Tabary, 2013; Cunha et al., 2015; Germann et al., 2016). The base radar data are stored as three-dimensional fields characterised by the three polar coordinates, i.e. range, azimuth and elevation (r, ϕ, θ). The scanned region can reach ranges up to 250 km or 300 km from the radar, depending on the Pulse Repetition Frequency (PRF) and on the wavelength and peak power of the transmitted radiation. The range resolution of the measurements is determined by the pulse duration and/or the timing of the sampling trigger clock in the radar processor and commonly ranges from 100 m to 1000 m. Radar measurements are averaged over a number of pulse samples which, together with the antenna scan speed and the PRF, determines the angular resolution in the scanning direction. This resolution is typically of 1°, corresponding to linear resolutions of around 50 m at short ranges and 4 km at the farthest ranges, accounting for a linear increase of the beam cross section with range.

These base radar data are used to derive radar site downstream products that are instead represented projected in Cartesian fields. Common operational site products such as constant altitude reflectivity, ground projected maximum reflectivity,

echo top, and vertical reflectivity profile are calculated directly from the base reflectivity. Precipitation products, that is, the surface rainfall rate and surface rainfall accumulations for various time intervals, require parametrisation and application of the relationship in Equation 1.3, or other more sophisticated relationships based on polarimetric data. Finally, the base radial velocity can be processed, generally under the assumption of a uniform or linear wind model, to estimate the vertical profile of the horizontal wind over the radar site (Browning and Wexler, 1968; Waldteufel and Corbin, 1979).

1.2 Error sources and quality control

Identification of the sources of error in weather radar measurements is the first step towards an improved user-oriented quality control for base radar data and downstream site products. The total error in the radar precipitation estimates can be evaluated in comparison with reference measurements (see Gjertsen, 2002; Germann et al., 2006; Trapero et al., 2009, for instance) but investigation of the individual error sources and their mutual interactions is essential for the design of quality control procedures and allows to characterise the goodness of the data according to the product and/or the requirements of the end user or application.

Quality control may be defined as the ensemble of methods designed to identify and treat errors in observational data in order to improve their quality (Michelson et al., 2004). Quality characterisation is a process tightly linked to quality control thought to facilitate the propagation of quality information between the weather radar data providers and the data users.

Figure 1.1 reproduces the generalised quality characterisation framework described in Holleman et al. (2006) and in Norman et al. (2010). Such a quality framework has been applied to weather radar base data in Friedrich et al. (2006) and Ośródka et al. (2014). In the core or interface of the framework are the quality indicators; physically meaningful quantities, flags or normalised indexes that quantify the affectation of the radar estimates by each of the recognised error sources and the improvement brought out by the applied correction algorithms. The quality indicators are the quantities of interest for the data user who, with the expertise in the weather radar data applications and the knowledge of their sensitivity to the different error sources, can combine them in an appropriately weighted way in order to derive the quality index relevant for each particular application. For instance, these tailored quality indexes can be used for visualisation of radar data (Peura et al.,

2006) and generation of cartesian site products (Ośródka and Szturc, 2015), for computing probabilistic Quantitative Precipitation Estimates (QPE) (Szturc et al., 2011) and for compositing data from different radars in a network (Fornasiero et al., 2006a; Sandford and Gaussiat, 2011)

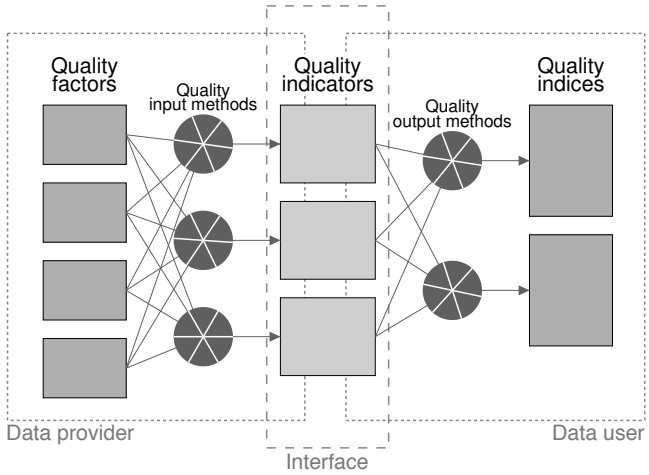

Figure 1.1: Quality characterisation framework proposed by Holleman et al. (2006) (adapted from Figure 3.1 and Figure 3.2 in Holleman et al. (2006)).

The task of the data provider, i.e. the weather radar operator, is to identify the group of factors that characterise the radar system, software and measurement (as listed in Holleman et al., 2003) and to combine them to define and evaluate the quality indicators. In the process of conversion of the quality factors into quality indicators (*quality input methods*), a detailed understanding of error sources associated to the instrument, to the radar siting and measurement technique and to the meteorological conditions is required (Gekat et al., 2004).

In the following, a brief relation of the main error sources affecting base weather radar data is presented. The focus on base data quality control includes all instrumental and methodical error sources and also several sources related to the external meteorological conditions but excludes those errors associated with the estimation of the rain rate and surface precipitation. Further information on the omitted error sources such as beam filling and overshooting, melting layer effects and the variability in the DSD and in the vertical distribution of precipitation can be found in Wilson and Brandes (1979); Zawadzki (1984); Michelson et al. (2004); Holleman et al. (2006) and in Villarini and Krajewski (2010), for instance.

1.2.1 Instrumental

Instrumental sources of error are those intrinsic to the complex electronic and mechanical radar system. In a first instance, any system component malfunction is an obvious source of error. Periodical maintenance tasks and *in-situ* or remote checks of the performance of the radar components (Beekhuis and Leijnse, 2012) are therefore essential for prevention and fast identification of potential failures. Along the same lines, monitoring and control of the temperature of the system gives assurance on the electronics stability.

Instrumental limitations related to the radar system design, even if not an error source *per se*, determine the ability of the weather radar to estimate precipitation (Kirstetter et al., 2010, 2012). At this regard, quality factors such as the operating wavelength, the transmit peak power and the dynamic range of the receiver must be taken into account. Indeed, the wavelength of the emitted radiation is related to the backscattering power of water droplets and to the attenuation of the signal throughout the medium and determines the trade-off between the maximum Doppler velocity and the maximum unambiguous range measurable by the radar.

The cornerstone for quality assurance at an instrumental level is the accuracy of the radar system calibration. Calibration encompasses the antenna positioning system as well as the radar transmit and receive chains. Accurate antenna alignment, including the alignment between the electrical and mechanical axis, is required for correct geolocation of radar estimates and can be achieved by comparing the positioning system readouts with reference positioning information from either active or passive targets (Divjak, 2009; Manz et al., 2000; Holleman and Beekhuis, 2004). Calibration of the transmitting chain includes monitoring and adjusting critical parameters of the electromagnetic pulse emission (pulse repetition frequency, pulse length, average and peak power) and of the antenna (beam width, side lobes and gain) as well as periodically measuring losses in transmission (waveguide and radome losses). The most common procedure for calibration of the receiving chain consists on measuring the response curve of the receiver by recording the receiver power output as a function of varying power levels inserted at the antenna feed. This response curve gives information on the receiver noise, gain and dynamic range. Modern weather radar systems and processors have built-in capabilities and provide means for calibration and parameter control in the transmit and receive chains; e.g. real-time measurements of transmitted pulse power, real-time system noise sampling and receiver response function testing tools (Vaisala, 2014b).

The accuracy of the weather radar reflectivity estimates is critically determined

by the calibration of the whole transmit-receive chain. The absolute accuracy of reflectivity estimates is commonly tested using passive targets of known backscattering cross-section or reflectivity, while the stability of the estimates can be assessed by monitoring mountain echo returns (Sempere-Torres et al., 2003; Silberstein et al., 2008). In addition, the relative calibration between radars in a network may be quantified by means of pair-wise comparisons (Huuskonen, 2001; Saltikoff et al., 2010).

1.2.2 Radar siting and measurement specific

Methodical errors are inherent to the weather radar measurement setup. These include error sources related to the geometry of weather radar measurements, the scanning strategy and also error sources that arise from the combination of the measurement setup and the radar siting, such as beam blockage and non-meteorological radar echoes.

Beam broadening is the main error source associated to weather radar measurement geometry. The radar beam is the virtual volume that envelops the emitted pulses in their propagation through the atmosphere and away from the radar site. Due to geometrical considerations, the beam cross-section expands with the distance from the radar and hence the linear resolution of the sampled volume varies as a function of range. At farther ranges, the resolution decreases and results in information loss and increased uncertainty due to averaging. Also, the probability of inhomogeneous beam filling is enhanced and the bright band correction is hindered by the beam broadening effect (Kitchen and Jackson, 1993).

Parameters defining the scanning strategy such as the antenna rotation speed, the number of pulse-average samples and the PRF constitute primary quality factors that determine the resolution of the probed atmospheric volume. Furthermore, these parameters influence the spectral width of the measured signal, affecting the variance of the radar velocity estimates. In particular, the PRF determines the maximum measurable unambiguous range and velocity. A too low unambiguous velocity increases the probability of obtaining biased velocity estimates when the true velocities exceed the maximum measurable velocity of the radar (Doviak and Zrnič, 1984).

Radar data, especially at the lowest scan elevations, are often contaminated by non-meteorological echoes from scattering targets as birds, insects, aircraft and ships. Electronic interferences from external emitters as microwave links and the sun are also often the cause of non-meteorological signatures in radar data. Aircraft

and ships appear as large discontinuous speckles in reflectivity data, while interfering signatures commonly reveal as radial spokes in the direction of the emitter. Conversely, low intensity widespread reflectivity fields close to the radar site are often attributable to contamination by biological targets. The latter constitute in most cases targets with autonomous motion and hence have a significative impact on Doppler velocity estimates, increasing their variance and hampering the quality of wind products (Holleman, 2005). In addition, weather radar imagery is often contaminated by clutter resulting from the nearby presence of wind mills (Norin and Haase, 2012; Argemí et al., 2012). Due to the blade rotation, wind turbines have a potentially strong impact on Doppler radar capacities. Moreover, wind turbines can prevent the radar beam from shaping correctly causing down-range estimation errors (Belmonte and Fabregas, 2010).

Non-precipitation echoes also appear in the form of clutter from ground or sea. Ground clutter echoes resulting from the interception of the radar beam with the discontinuities in the surrounding terrain (e.g. mountains, trees, buildings, masts) are commonly identified and suppressed using static or modelled clutter maps (Delrieu et al., 1995) or Doppler filtering procedures based on the measured velocity spectra (Doviak and Zrnič, 1984; Vaisala, 2014b). Sea clutter filtering, on the other hand, is challenging as it generally appears in the form of large areas of high reflectivity echo patterns and with Doppler velocities that resemble those of precipitation. Further methods proposed for detection of non-meteorological echoes in radar data rely on image processing algorithms (Peura, 2002) or on identifying radar variables that allow echo differentiation for application in decision tree, neural network, fuzzy-logic or threshold based echo classification procedures (see Berenguer et al., 2006; Gourley et al., 2007; Lakshmanan et al., 2007; Chandrasekar et al., 2013, and references therein).

Elevated topographical features such as mountains and buildings can also cause partial or total beam blockage, critically limiting the radar horizon, notably in areas of complex orography (Gjertsen and Dahl, 2002; Germann et al., 2006). In this situation, precipitation in the shielded region is a priory undetectable and gives rise to beam filling errors. The shielded fraction of the beam can be relatively simply estimated from a detailed knowledge of the surrounding topography assuming a geometric-optics approach (Bech et al., 2003) and can be used to determine the possibility and accuracy of the correction (Fulton et al., 1998; Gabella and Perona, 1998; Bech et al., 2007b). Beam blockage is a major issue to consider when selecting the radar siting and the parameters defining the radar horizon constitute primary quality factors; for instance, the accuracy of the antenna pointing readings is crucial

for beam shielding assessment and correction.

1.2.3 Meteorological conditions

Several errors affecting the accuracy of weather radar estimates arise from the external meteorological conditions (temperature, pressure, humidity, presence of precipitation, precipitation type and distribution, etc.) at the time of the measurement. At this regard, the two main error sources affecting radar base data are anomalous atmospheric propagation conditions and the attenuation of the signal.

The propagation path of the radar beam is conditioned by the refractive properties of the atmosphere. In particular, the degree of refraction of the beam is determined by the Vertical Refractivity Gradient (VRG), which depends on the temperature, pressure and humidity conditions of the atmosphere at the corresponding atmospheric layer. Anomalous Propagation (AP) of the radar beam takes place when these atmospheric conditions differ significantly from the established standard, which assumes a negative and uniform VRG with increasing elevation, resulting in super-refraction or sub-refraction of the trajectory of the emitted signal (Doviak and Zrnič, 1984). For example, under super-refractive conditions the radar beam bends towards the ground, increasing the incidence of both ground or sea clutter echoes and beam blockage by topographical obstacles (Fornasiero et al., 2005). Anomalous propagation conditions can be diagnosed using complementary measurements such as satellite or radiosonde observations and may be forecast by means of NWP modelling of the vertical refractivity profile (Fornasiero et al., 2006b; Bech et al., 2007a; Bebbington et al., 2007).

In their path through the atmosphere, the microwave signals emitted by the radar are attenuated due to absorption and scattering by atmospheric gases and hydrometeors. The degree of attenuation depends mainly on the wavelength of the signal and on the size and composition of the targets. For the wavelengths at which weather radars operate, gaseous attenuation is small and does not vary strongly. Indeed, modern radar processors implement automatic gaseous attenuation correction, typically applying a user defined constant value or a functional range-height dependence. On the other hand, attenuation by precipitation can cause significative inaccuracies in the reflectivity estimates, particularly for radars operating at relatively low wavelengths such as C-band (3.75 - 7.5 cm) and X-band radars (2.5 - 3.75 cm). For C-band radars, the attenuation of the signal in heavy rain can reach 10 dB per 100 km, which translates into inaccuracies ranging from 2 dBZ to 20 dBZ in reflectivity. Hitschfeld and Bordan (1954) derived an analytical equation for

quantification and correction of the along-path attenuation based on the estimated reflectivity. However, due to the ill-conditioning of the problem, particularly with regard to small errors in the radar calibration constant, the solution to the equation is unstable and needs to be constrained using additional measurements (Delrieu et al., 1997; Iguchi et al., 2000; Berenguer et al., 2002; Meneghini et al., 2004). Alternative attenuation corrections rely on double-frequency (Meneghini et al., 1992) or polarimetric radar measurements (Bringi and Chandrasekar, 2001; Vulpiani et al., 2008), for instance.

1.3 Conclusions

Weather radars are essential instruments for real time weather surveillance and precipitation monitoring with high spatiotemporal resolution and coverage. The advent and spread of radar networking in the last decades has fostered the usage of primary weather radar data and downstream products in a wide variety of meteorological, hydrological and climatological applications of great socio-economical relevance. The quality of radar data is however affected by various error sources that derive from the radar instrument characteristics and operation, that are inherent to the measurement setup and that arise from external environmental and meteorological conditions. Data management in weather radar networks has raised awareness about the need for establishing standardised and, when possible, worldwide available quality control procedures for radar data quality assessment and improvement. These quality control procedures should preferably be designed within a framework that allows for a quality characterisation tailored for the particular weather radar end product and/or application.

The present thesis addresses quality control procedures in the regional weather radar network of the SMC based on the quality standards proposed by the European radar networking referents. As will be detailed in the following chapter, the quality factors and procedures tackled focus on instrumental and measurement specific error sources, complementing the already existing quality control framework in the network, with the aim of lying the groundwork for the establishment of a robust quality characterisation framework.

2

Objectives and structure

In 2012 the Autonomous Government of Catalonia launched the Industrial Doctoral Programme (PDI), which opened a new channel in the Catalonia region for the transference of knowledge between the university and private companies and public agencies. The main purpose of the PDI is to fuel the competitiveness and the internationalisation of the Catalonian industry. Promoted by the PDI, the present Ph.D thesis is the result of a three-year project developed, jointly with the Department of Astronomy and Meteorology of the University of Barcelona (UB), within the work environment of the Remote Sensing group which operates the regional weather radar network (XRAD) of the Meteorological Service of Catalonia (SMC).

2.1 Main objectives

The general objective of the Ph.D research is to propose standardised quality control tools and procedures, relevant for the quality assessment by weather radar network operators, that complement and/or improve the existing ones according to the state of the art of radar data quality control in the international weather radar community. In particular, the project aims to improve the quality control for the online data collected by the single-polarisation C-band radars constituting the XRAD weather radar network of the SMC. Following the guidelines of the PDI, the main objectives of the doctoral work have been defined attending to the development and innovation priorities and needs of the XRAD and of the SMC:

1. To develop and implement, for the XRAD, methodologies that allow the radar operators at the SMC to remotely monitor, on a periodic or continuous basis,

the calibration state and the performance of the radar system.

2. To improve the quality of the Doppler velocities estimated by the XRAD radars, focusing on the presence of outliers that arise from the dual-PRF processing scheme applied.

3. To provide guidelines for application of the proposed quality control methodologies and resources for the interpretation of their results, aiming to facilitate the task of the radar operators and technicians.

The outlined objectives are defined under the framework of an operational weather radar network and therefore require, for a real-time data and product supply, that the strategies and algorithms to be implemented consider and respect, when applicable, the continuous and uninterrupted operation and the maximum processing time allowed by the scanning strategy. In addition, the main objectives stablished and the results derived are exportable, with slight modifications, to weather radar networks other than the XRAD. On behalf of affordability, flexibility, transparency and interoperability, the algorithms are required to be developed and implemented using open source programming languages (Python, 2001; R Core Team, 2016) and, when available, open source modules and libraries specific for weather radar data processing.

2.2 Specific objectives

Based on the main objectives defined above, the following specific objectives have been established:

(a) To adapt a solar interference detection algorithm for its application under the scanning settings of the XRAD.

(b) To implement for the XRAD the Sun-based technique for online monitoring of weather radar antenna alignment and receiver chain calibration.

(c) To study the accuracy of the Sun-monitoring technique under varying observation conditions.

(d) To compare the solar technique with methodologies for antenna alignment calibration already implemented for the XRAD.

(e) To devise and implement an algorithm that identifies and corrects dual-PRF outliers in Doppler velocity data.

2.3 Structure of the thesis

This Ph.D. thesis report is structured in four main parts.

Part I: Introduction. The introductory part, covering up to the present chapter (Chapter 1 and Chapter 2), has laid the groundwork for the project, presenting a general overview of the fundamentals of weather radar measurements and applications with the focus on the relevance of quality control and characterisation in radar networking environments.

Part II: Data. The upcoming second part, featuring Chapter 3, pictures the data framework, introducing the XRAD weather radar network, specifying its system characteristics and scanning settings and describing the quality control procedures applied.

Part III: Results. The third part collects the results of the thesis, organised in four extended chapters whose structure follows the specific objectives outlined above. In particular, in Chapter 4 the adaptation and modification of the solar interference identification algorithm is presented and the application of the algorithm for monitoring the incidence of electronic interferences in the XRAD is exemplified. Chapter 5 thoroughly describes the online solar monitoring methodology and shows how it has been adjusted and applied for monitoring the calibration status of the XRAD radars. This chapter also includes a simulation and performance analysis of the solar monitoring method under controlled conditions. In the next Chapter 6, three widespread methodologies for antenna pointing calibration are reviewed and comparatively assessed. Finally, Chapter 7 presents and evaluates a new algorithm for improved identification and correction of outliers in dual-PRF velocity data, with examples applied to both XRAD data and to radar data provided by the Atmospheric Radiation Measurement (ARM) radar group at the Argonne National Laboratory (ANL) in the United States.

Part IV: Conclusions. The fourth and final part comprising Chapter 8 summarises the thesis results, providing specific recommendations based on the conclusions extracted during the thesis work.

Part II
DATA

3

The XRAD radar network

According to the current legal framework, the SMC is, together with the Spanish Meteorological Agency (AEMET), the public agency responsible for providing meteorological information to civil defence authorities of the autonomous region of Catalonia. Catalonia, covering an area of about 32 000 km^2 in the Northeastern territory of the Iberian Peninsula, displays a complex topography with relatively small catchment basins prone to flash flooding by severe rainfall events frequent in the dominant torrential Mediterranean regime (Llasat et al., 2005; Barnolas and Llasat, 2007; Ricard et al., 2012; Llasat et al., 2016). At this regard, the XRAD weather radar network operated by the SMC constitutes a key tool for weather surveillance and short-term forecasting, for quantitative precipitation estimation and

for the study of heavy precipitation events in the region (see Pineda et al., 2006; Trapero et al., 2009; Velasco-Forero et al., 2009, for instance).

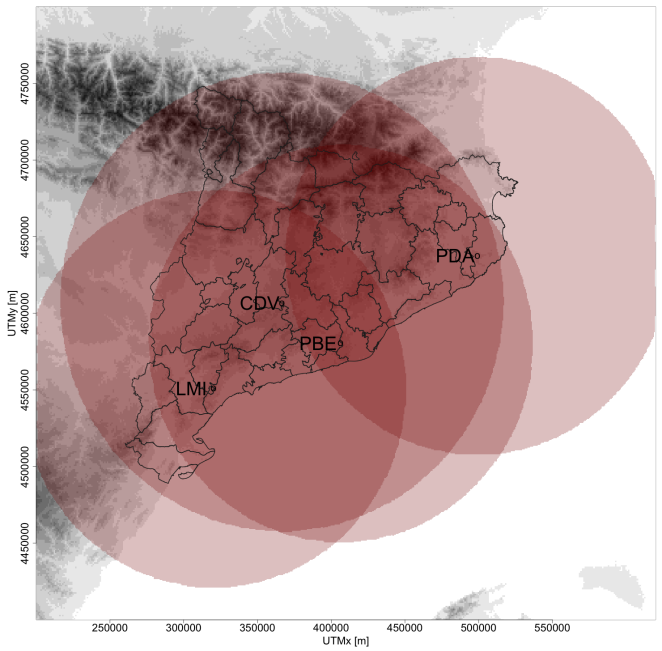

Figure 3.1: XRAD network weather radars and their coverage of the Catalonia region at the lowest elevation of the short-range volumetric scan.

Table 3.1: Site name, abbreviated radar designation, installation year, altitude and location coordinates of the XRAD radars.

Name	Abbrev.	Year	Latitude	Longitude	Altitude
Creu del Vent	CDV	2003	41.69° N	1.40° E	825 m
La Miranda	LMI	2008	41.09° N	0.86° E	910 m
Puig Bernat	PBE	1996	41.37° N	1.39° E	610 m
Puig d'Arques	PDA	2002	41.89° N	2.99° E	542 m

The XRAD is a high density network composed of four C-band single-polarisation Doppler weather radars: Creu del Vent (CDV), La Miranda (LMI), Puig Bernat (PBE) and Puig d'Arques (PDA). The network was completed be-

tween 2002 and 2008 years, conceived to complement the already existing PBE radar located near Barcelona. The location and coverage of the four radars is shown in Figure 3.1. The altitude and location coordinates of each of the radar sites are listed in Table 3.1. The operation of PBE radar temporarily ceased in 2012 and is expected to be operative in 2016 again. The data and results presented in this report correspond to the three radars operative in the 2013-2015 period (CDV, LMI and PDA) during which the thesis work was developed. As detailed in the following, the three operative radars are very similar regarding their technical characteristics.

3.1 Technical characteristics

Modern Doppler weather radars are complex electro-mechanical instruments that consist of five main subsystems (Doviak and Zrnič, 1984; Gekat et al., 2004): the antenna, which shapes and transfers the transmitter energy to signals in space; the transmitter, where the microwave pulses are modulated, amplified and transmitted; the receiver, which amplifies the received signal and removes the carrier radio frequency, splitting the signal into its in-phase and quadrature-phase components; the processor, which samples, digitises and processes the signal components, rendering the radar spectral moments (reflectivity Z, velocity V and/or spectrum width W); and the controller, which manages the various electrical signals that are required to control and operate the radar and antenna system. The XRAD radars are fully coherent Doppler systems operating at 5600 MHz frequency (≈5.36 cm wavelength). The block diagram in Figure 3.2 details the subsystems and relevant components of the XRAD radar systems.

3.1.1 Antenna

The typical XRAD antenna system is based on a C-band linear polarisation feed design (manufactured by ORBIT Co.). It comprises an antenna/feed unit and an azimuth-elevation tracking pedestal with an outdoor controller hosted in the radar rack. The antenna/feed unit consists on a 3.8 m parabolic main reflector with a pyramidal horn antenna. The feed horn is attached with an offset from the centre of the disk. This *off-axis feed* configuration, in comparison to an *axial feed* Cassegrain configuration (Skolnik, 1980), reduces the side lobes in the radiation pattern. The nominal antenna gain is 44 dB and the nominal beamwidths are 1.20° and 1.10° in the horizontal and vertical planes respectively, given up to a precision of ±0.05°. The antenna disk is mounted on an elevation-over-azimuth positioner, assembled on

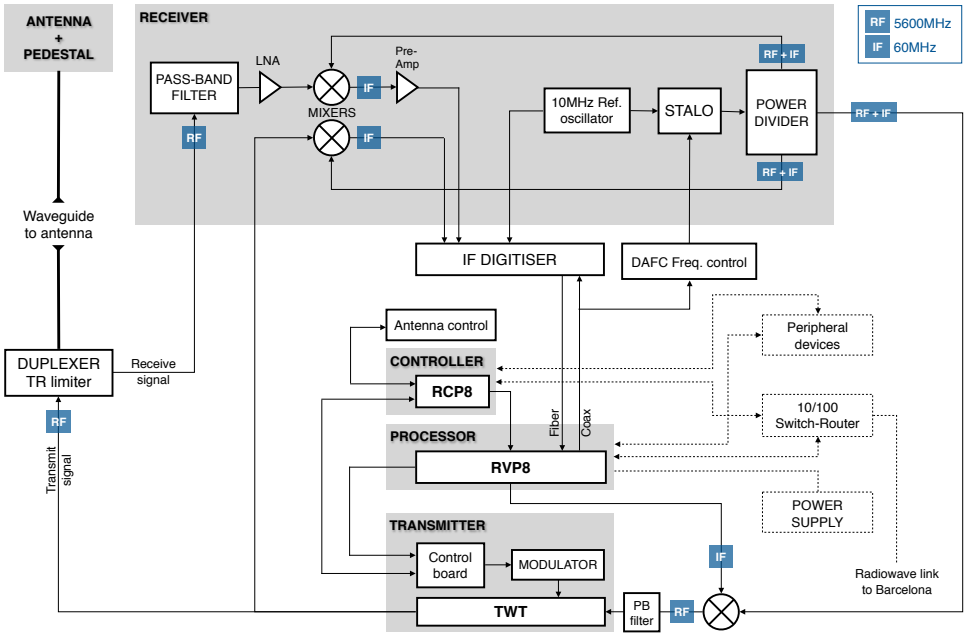

Figure 3.2: Block diagram of the XRAD radar systems' components. Figure adapted from Bech et al. (2004) by Oriol Argemí.

a base raiser, that allows independent movements in azimuth and elevation with an orthogonality error of 0.04°. Manufacturer specifications assign the pointing system an accuracy of 0.03°. The antenna positioning control is managed by a RCP8 unit manufactured by SIGMET, Inc (Vaisala, 2014c). The antenna is connected to the transmit/receive systems through the waveguide and then the duplexer. The latter is responsible for routing the transmit signal to the antenna and the backscattered signal to the receiver and incorporates a Transmit/Receive limiter for isolation of the receiver during the high power transmission stage.

3.1.2 Trasmission

The transmitters in the XRAD radars use a coherent helix Travelling Wave Tube (TWT) for amplification of the 5600 MHz carrier Radio Frequency (RF) signal. The RF input to the TWT is supplied by up-conversion of the 60 MHz Intermediate Frequency (IF) signal generated in the front-end circuitry of the receiver. The TWT is a pure amplifier which, coupled to a modulator, produces a modulated high power output from a low power input. The pulses generated in the transmit system of the

XRAD radars have a width of 5 µs and a nominal transmit peak power of 7500 kW.

3.1.3 Reception and processing

The backscattered signal collected at the antenna is routed to the receiver, which in the case of XRAD radars is based on superheterodyne architecture. The front end of the receiver consists of a pass-band filter matched to the transmitter bandwidth (see Table 3.2) followed by a Low Noise Amplifier (LNA) for optimisation of the Signal-to-Noise Ratio (SNR) of the system and a traditional single RF to IF downconversion stage. The RF signal is supplied by a digital STAble Local Oscillator (STALO), a frequency synthesiser that uses a Phase Lock Loop (PLL) to produce the RF by multiplying up a 10 MHz reference oscillator. After splitting and downconversion to IF, the resulting in-phase and quadrature-phase signal components are sampled in the Intermediate Frequency Digitiser (IFD), whose trigger and sampling timing is synchronised with the 10 MHz reference oscillator for enhanced coherency. The IF transmit signal is also sampled, supplying the reference phase for Doppler processing. The dynamic range of the XRAD receivers is about 95 dB, accounting for the saturation limits of the analog components and the resolution of the Analog-to-Digital Converters (ADCs) in the digitiser. The maximum resolution allowed by the transmit pulse width and the receiver bandwidth is of 125 m but the sampling is set for an effective resolution of 250 m.

Table 3.2: Bandwidth of the receivers in the operative XRAD radars.

Receiver bandwidth		
CDV	LMI	PDA
232 kHz	232 kHz	227 kHz

The sampling data is input to the processing flow, which is controlled by a digital SIGMET RVP8 processor (Vaisala, 2014b). The processing flow (see Doviak and Zrnič, 1984; Gekat et al., 2004, for a detailed description) is designed for estimation of the spectral moments (Z, V, W) through pulse autocorrelation processing but also includes quality control procedures such as Doppler clutter filtering and interpolation, range averaging, thresholding and noise power correction. The XRAD processors estimate the autocorrelation moments using Digital Fourier Transform or Fast Fourier Transform (DFT/FFT) processing. The final output of the RVP8

are quality controlled digital spectral moment data which are sent over the network to the central radar computers in Barcelona via a Transmission Control Protocol/Internet Protocol (TCP/IP) based Wide Area Network (WAN) connection.

3.2 Scanning strategy

The operative scanning strategy of XRAD radar systems consists of a main task named *PPIVOL* which is divided in three sub-tasks during which each of the radars perform Plan Position Indicator (PPI) scans at several fixed elevations (see Table 3.3). This duty cycle is repeated continuously on a 6-minute basis and consists of a long range single-PRF scanning sub-task at 0.6° elevation, designed for fast weather surveillance, and two short range, dual-PRF, multiple elevation volumetric sub-tasks. Short range sub-tasks are preset at fixed elevations ranging from 0.6° to 27°. For each of the sub-tasks, the radar processor outputs a file containing the corresponding raw base radar data in polar coordinates (RAW volume data). The output files are compressed in raw IRIS format and the data is stored in 1-byte binary units. The user may select which base radar data are stored in the RAW files; in the case of the XRAD, the spectral width (W) is computed and used for quality control filtering in the processor but only uncorrected reflectivity (T, i.e. noise corrected but without application of the Doppler clutter filter), reflectivity (Z) and Doppler velocity (V) are stored.

Table 3.3: Name, description and scanned elevations for each of the sub-tasks defined in the scanning strategy of the XRAD radars.

Sub-task	Description	Data output	Elevation(s) [°]
VOL_A	Long range (surveillance)	T, Z	0.6
VOL_B	Short range (volumetric)	T, Z, V	0.6, 0.8, 1.0, 1.3 1.7, 2.0, 3.0
VOL_C	Short range (volumetric)	T, Z, V	4.0, 5.0, 6.0, 8.0, 10.0 13.0, 16.0, 21.0, 27.0

The antennas of the XRAD radars scan continuously at a fixed speed Ω_{scan} of $24\,^{\circ}\,\text{s}^{-1}$ (4 rpm). However, as specified in Table 3.4, other sampling settings such as

the PRF, the corresponding maximum range and the number of pulses averaged in the autocorrelation processing, vary for each of the sub-tasks depending on the radar considered. For instance, in short range volumetric sub-tasks the dual-PRF scanning and processing scheme is applied for extension of the maximum measurable velocity (Vaisala, 2014b). In the particular case of the CDV radar, the corresponding high and low PRFs chosen allow to enlarge its coverage up to a range of 150 km, in order to supply the Vall d'Aran region at the Northwestern extreme of Catalonia with volumetric radar data including the Doppler velocity estimates (see Figure 3.1).

The azimuthal or radial resolution of the polar products derived from the scheduled sub-tasks is determined by the antenna scan speed, the PRF and the number of pulse samples. The radar processor allows the user to set all four parameters so that, if desired, a higher number of samples can be used borrowing samples from the previous radial to decrease the standard deviation of the estimated radar moments. The nominal radial resolution set in the processor for the XRAD radars is 1° and the number of pulse samples is chosen, according to the scan speed and the PRF in each case, in order to achieve this resolution. In the case of the dual-PRF short range volumetric sub-tasks the high PRF is used as reference, which ensures that the angular resolution is close to the nominal for all radials in the scan. Regarding range resolution, range averaging in the processor is performed over four range samples, each corresponding to a 250 m resolution, resulting in a final resolution of 1000 m.

Table 3.4: Scanning and sampling settings of the operative XRAD radars for the long and short range sub-tasks: antenna scan speed (Ω_{scan}), Pulse Repetition Frequency (PRF), number of pulse averaging samples (M) and maximum range (R_{max}).

Task	Description	Radar	Ω_{scan} [$^\circ\,\text{s}^{-1}$]	PRF [Hz]	M	R_{max} [km]
VOL_A	Long range	CDV	24	450	19	250
		LMI				
		PDA				
VOL_B VOL_C	Short range	CDV	24	1000/750	42	150
		LMI		1150/862	48	130
		PDA		1150/862	48	130

3.3 Quality control

The cornerstone for fulfilment of the SMC civil duties is continuous weather surveillance. Consequent to this principle, the XRAD network operators are responsible for ensuring the correct and uninterrupted performance of the weather radars, particularly when a precipitation event is expected and also during and after the event itself. These responsibilities encompass the establishment and supervision of *in-situ* radar system maintenance tasks and the development and evaluation of remote performance monitoring tools. The quality control process also concerns radar data and the product generation chain. Quality control of radar data in the XRAD starts at the radar processor and is complemented by *ad-hoc* methodologies designed for real-time quality assessment and correction.

3.3.1 Radar maintenance

In-situ maintenance tasks of XRAD radar systems are commended to specialised technicians from a subcontractor company. These tasks are either *preventive*, designed in advance to ensure the correct performance of the radar and to anticipate and/or detect any possible anomalies; or *corrective* and hence *ad-hoc* devised for the particular radar malfunction or problem detected. Preventive maintenance tasks are stipulated in the binding contract between the SMC and the subcontractor and are classified based on their periodicity. Weekly maintenance tasks include assessing the condition of the radar infrastructure and verifying the correct operation of auxiliary systems such as power supplies (Uninterrupted Power Supply, UPS, and Genset), climate control devices and the Power Logic Control (PLC) unit. During bimonthly maintenance tasks, the response curve of the radar receiver is measured and the resulting front-end noise of the receiver is set in the processor. Also, the antenna pointing biases in azimuth and elevation are estimated by means of offline scans of the solar disk; if any of these biases exceeds 0.1° the offset is corrected in the controller. Biannual tasks include, in addition, the measurement of the antenna waveguide losses. Finally, during the annual maintenance tasks the antenna pedestal levelling error is measured and corrected and measurements of the antenna power diagram are carried on using a fixed, point-like target located in the far field of the antenna, in order to validate the azimuthal and zenithal antenna patterns and to estimate the main lobe beamwidths.

3.3.2 Processor filters

As pointed out in Subsection 3.1.3, a series of quality control filters are automatically applied by the radar processor during the spectral moment data estimation (Vaisala, 2014b). The thresholding is carried on independently for each range bin (i.e. resolution volume). In a first instance, before pulse autocorrelation processing, in-phase and quadrature phase components of the received signal are clutter filtered in the frequency domain. For the XRAD radars, the clutter correction is performed using a filter that removes spectral components in a variable width stripe around 0 valued frequencies and linearly interpolates the spectrum between the removed clutter boundaries. The corrected signal components yield the corrected reflectivity (Z), the Doppler radial velocity (V) and the spectrum width (W) estimates. The uncorrected reflectivity (T) is instead estimated from the incoming uncorrected signal components.

Table 3.5: Threshold values of the processor filters applied to each of the scanning subtasks of the XRAD radars.

Radar	Task	LOG [dB]	CSR [dB]	SQI
CDV	VOL_A	2.50	18	–
	VOL_B	2.50	18	0.35
	VOL_C	2.50	18	0.35
LMI	VOL_A	3.00	26	–
	VOL_B	3.00	26	0.35
	VOL_C	2.50	26	0.35
PDA	VOL_A	2.25	24	–
	VOL_B	1.50	24	0.40
	VOL_C	0.50	24	0.42

After spectral moment estimation, the processor calculates the SNR (LOG), the Clutter-to-Signal Ratio (CSR) and the Signal Quality Index (SQI) for each range bin using the autocorrelation moments and discards those bins with values below the indicated thresholds. The LOG filter serves to quality control uncorrected and clutter corrected reflectivity data (T, Z) based on the signal strength. The LOG threshold is not exactly the SNR but the ratio of Signal plus Noise to Noise, which

always yields a positive value in dB. In the case of clutter filtered data, i.e. Z and V, a clutter correction filter (CCOR) is also applied. The CCOR value is calculated from the CSR value, which is, in turn, computed from the clutter power. The clutter power is estimated from the comparison of the total clutter filtered and unfiltered powers at each range bin. The SQI value is a measure of the coherence of the signal which varies between 0 (incoherent, white noise) and 1 (complete coherency, pure-tone) and can be related to the SNR and to the spectral width. Therefore, the SQI is an indicator of the uncertainty in the velocity estimates and the corresponding filter is commonly applied only to Doppler velocity data V.

The user chooses which filters are applied to each spectral moment data and tunes the threshold levels of the filters for each radar and task, since their optimal values depend on the system characteristics and on external factors such as topography and surrounding interfering elements. The filter threshold values for the XRAD radars and tasks are specified in Table 3.5

3.3.3 Operative quality control

Operative quality control refers to post-processing tools and methodologies for radar system performance monitoring and radar data correction that operate in real-time or with uninterrupted periodicity.

XRAD radar operators have at their disposal an application named MAFRAD (Radar Operation Analysis Module) for remotely monitoring radar system performance, developed and implemented for the SMC by the Center of Applied Research in Hydrometeorology (CRAHI) of the Polytechnic University of Catalonia (UPC). MAFRAD is a modular application that collects the data generated by the XRAD radars, processes them with varying purposes and stores the results a in database that can be queried at any moment through a displayable web interface (Sancho Alcázar, 2009). As illustrated in Figure 3.3, MAFRAD allows the operator to monitor the number of complete volumes per day output by the radar, the efficiency in terms of the correlation between data in two consecutive radar images and the number of completed radials at each elevation scan as well as to compare the antenna elevation readings with the nominal elevations for these scans. Moreover, MAFRAD has a module devoted to the estimation of the antenna pointing biases in azimuth and elevation that uses mountain clutter returns as reference.

Radar system performance monitoring procedures for the XRAD also include an hourly noise test radar task, during which radar measurements (1000 samples) are carried on at fixed azimuth (0.5°) and elevation (30°) while fixed power noise

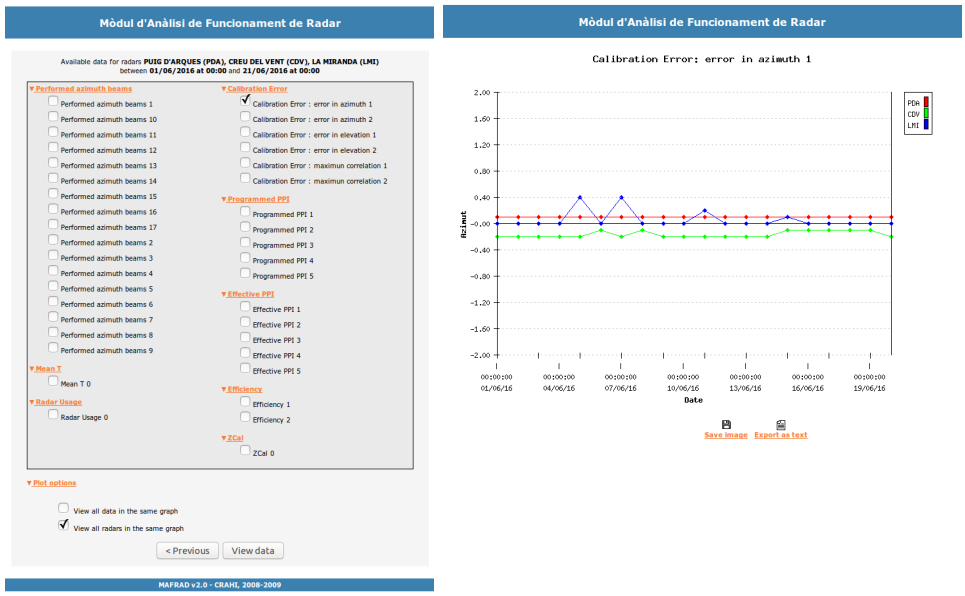

Figure 3.3: Radar performance query options available from MAFRAD web interface and example of azimuthal antenna pointing bias output display.

is injected at the waveguide coupler. The results can be remotely visualised in an IRIS range-time display.

In addition, the stability of radar measurements can be quickly assessed by means of an operative tool that monitors the average reflectivity of selected mountain clutter echoes for each XRAD radar (see Figure 3.4). Strong changes in the average reflectivity from these echoes are often indicative of instabilities or malfunction of the transmit-receive chain or the pointing system.

The atmospheric propagation conditions are operationally assessed on a daily basis using radiosonde data. Soundings are carried on at the Barcelona rawinsonde station (WMO code: 08190) (41.38°N, 2.12°E, 98 m ASL) using Meteomodem M10 sondes. Launches are programmed twice a day at 0000UTC and 1200UTC (Coordinated Universal Time). The soundings include surface data at the station location and temperature and humidity measurements at significant and mandatory levels that are used to estimate the vertical refractivity gradient of the first kilometre of air (VRG_{1000}) and a Ducting Index (I_D) in order to detect the occurrence of anomalous propagation events, following the guidelines in Bech et al. (2007a).

An operative tool for radar-gauge comparison is also available for the XRAD. This tool is based on the work by Trapero et al. (2009) and evaluates the accuracy

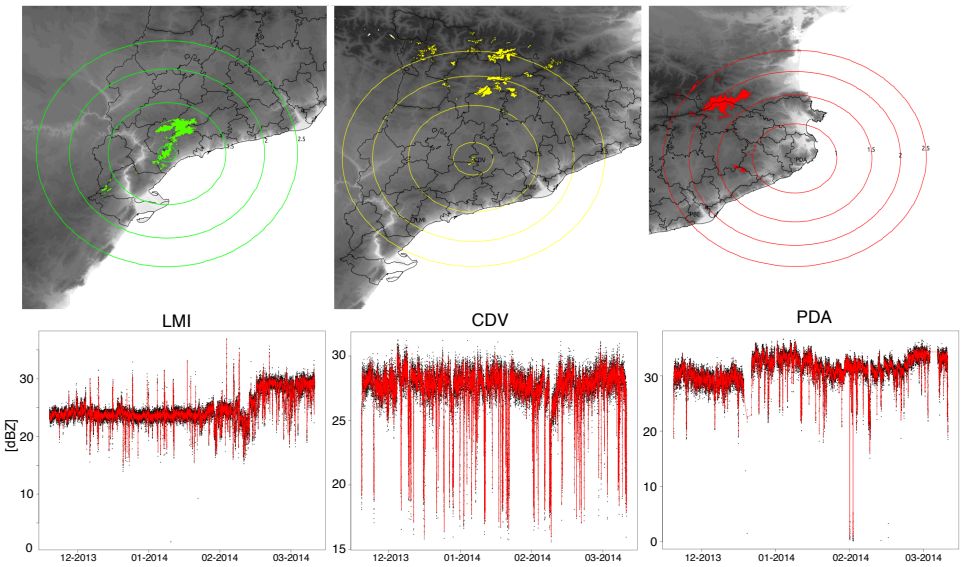

Figure 3.4: Operative monitoring of the transmit-receive chain and pointing system stability of the XRAD radars using ground clutter echoes. Top panels depict the ground clutter echoes selected for each of the radars at a 0.6° scan elevation and bottom panels exemplify the visualisation of the results, displaying the average ground clutter reflectivity for the individual scans on a 6-minute basis (black dots) and the daily average (red line). Figure source: Argemí et al. (2014)

of the daily precipitation estimates in QPE products of the XRAD by comparing them with the measurements from the rain-gauge network of the SMC. As shown in Figure 3.5, the QPE products evaluated are a short range daily rainfall accumulation directly estimated from the reflectivity data output by the radars (UNC QPE) and two other daily rainfall accumulation products (COR QPE and R+G QPE) which are generated, after correction of reflectivity data for the main radar error sources, by an *ad-hoc* software package.

Indeed, the raw polar data output by the XRAD radars is sourced to the EHIMI (Hydro-meteorological Integrated Forecasting Tool) software package, which corrects them in real time for their use in hydro-meteorological applications (Sánchez-Diezma, 2001; Sánchez-Diezma et al., 2002). The EHIMI software has been developed by the CRAHI and implemented operationally for the XRAD through a collaborative project funded by the Catalan Water Agency (ACA) and the SMC (Bech et al., 2005). The corrections applied by EHIMI can be summarised as: interpolation of lost azimuths, beam blockage correction and estimation and adjustment

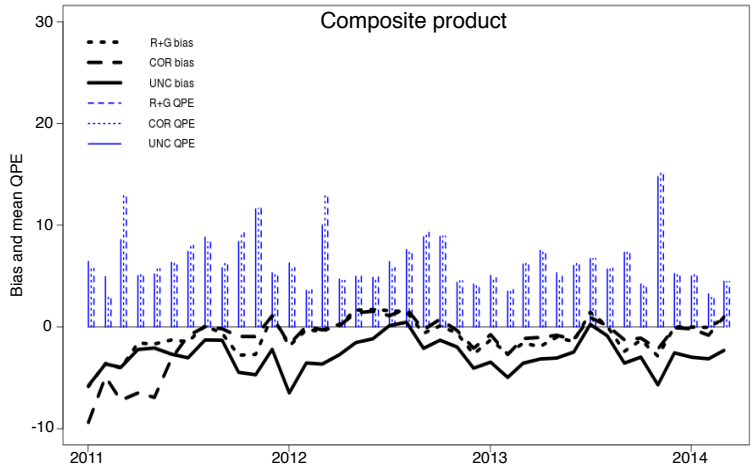

Figure 3.5: Example of monthly monitoring of radar-QPE composite products and the estimated biases with respect to rain gauge measurements (*cf.* Trapero et al., 2009). Figure source: Argemí et al. (2014)

of antenna pointing errors, secondary lobe contamination (Bellon and Kilambi, 1999) and speckle removal, identification and substitution of ground and sea clutter echoes (Sánchez-Diezma et al., 2001; Berenguer et al., 2006) and correction of the stability of radar rainfall estimates using mountain returns (Sempere-Torres et al., 2003). Furthermore the EHIMI system identifies bright band and convective areas and issues warnings for precipitation attenuation and severe rainfall in areas of interest. The real-time radar products generated by EHIMI include: corrected polar data (corrected RAW volumes) and cartesian PPI products, composite reflectivity products, 1 h and 24 h rainfall accumulations for the individual radars and for the composite and a 24 h accumulation product of gauge adjusted radar rainfall. These constitute key quality controlled products for meteorological and hydrological surveillance, modelling and forecasting in the Catalonia region.

Part III
RESULTS

4

Interferences from external emitters

* Section 4.1 of the present chapter has been adapted from: Altube, P., J. Bech, O. Argemí and T. Rigo, 2015: Quality control of antenna alignment and receiver calibration using the sun: adaptation to mid range weather radar observations at low elevation angles. *J. Atmos. Oceanic Technol.*, 32, 927-942, doi: 10.1175/JTECH-D-14-00116.1

Weather radar receivers are very sensitive, designed for the detection of the relatively weak signal backscattered by raindrops. In this context, signals from external sources emitting within the radar bandwidth are likely to be detected and interfere with the weather echo. These interfering signals can cause severe degradation of weather radar data quality and sensitivity. For instance, the radar precipitation estimates can be largely biased in regions where the external emitters are interfering

with the radar operation, as exemplified in Figure 4.1 for the XRAD. Consequently, interferences from external emitters compromise the efficacy of weather radar operations and derived applications, with particular concern about short-term forecasting and severe weather warning decision making processes (EUMETNET, 2008; Saltikoff et al., 2016; Joe et al., 2012).

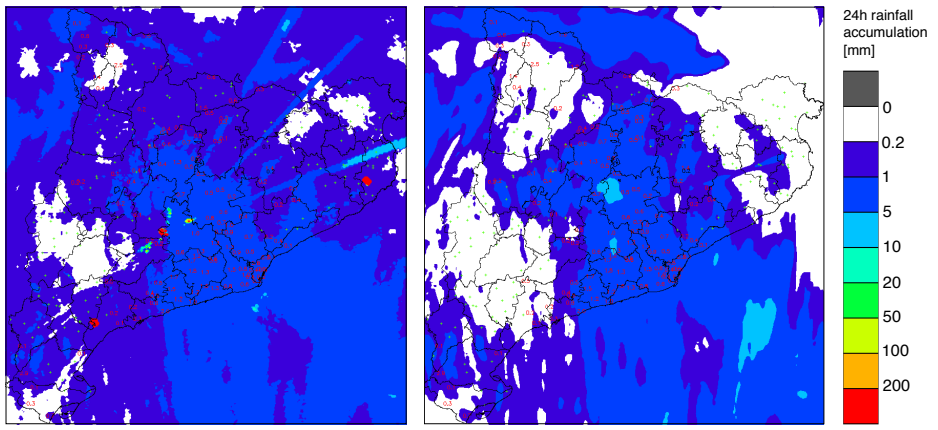

Figure 4.1: Example of affectation of radar QPE on 6 May 2016 by three persistent external radiowave emitters which interfere with the CDV radar operation at the Northeastern Catalonia region: (left) 24h accumulated radar rainfall XRAD composite and (right) 24h accumulated radar rainfall XRAD composite output by the EHIMI software after application of quality control corrections (see Chapter 3, Subsection 3.3.3).

Among the most frequently reported external interfering sources are the Sun, other radars and nearby Wireless Access Systems (WAS) including Radio Local Area Networks (RLANs). In particular, the latter have become a major threat for weather radar operations, mainly in the C-band (EUMETNET, 2008). Interferences by both the Sun and RLAN appear commonly in radar imagery in the form of characteristic radial spokes (Peura, 2002). In effect, since the radar estimates the distance to the scattering target from the time difference between the transmitted pulse and the received echo, continuous emissions, or high-rate bursty transmissions arriving at the receiver will give a signal in all or most of the range gates. In addition, the emission by these sources can be regarded as broadband compared to the bandwidth of the weather radar and is detected at the receiver as incoherent additive noise. Consequently, the interferences caused by the Sun and RLAN can in most cases be regarded as both continuous in range and constant in power.

The continuity feature of solar interferences was used by Holleman and Beekhuis (2004) to derive a main criterion for identification of these interferences in opera-

tional radar data. The criterion consisted on finding the continuity signature in long range (beyond 200 km) reflectivity data and the objective of their work was to collect and characterise solar signatures for online monitoring of weather radar receiver chain calibration and antenna alignment. In the present chapter the adaptation for application to mid-range data of the solar interference detection algorithm by Holleman and Beekhuis (2004) is presented. The modification of the original algorithm has allowed the implementation of the online Sun-monitoring method for the XRAD radar network, which is explained in detail in Chapter 5. The algorithm has been modified by introducing an additional identification criterion that accounts for the constant power characteristic of the solar signatures. In addition, the adapted algorithm is shown to be effective for simultaneous online identification of strong and persistent interferences from external emitters of non-solar nature and is currently being successfully applied to monitor the location and incidence of these interferences in the XRAD, which most frequently derive from RLAN devices. This information is periodically transmitted to the competent Radio Administration, for a case-by-case identification and regulation of the individual devices causing the interference.

4.1 Solar interferences

During sunrise and sunset, non-precipitation signatures related to the solar radio emission appear in volumetric scans. These solar interferences are recognisable in PPI displays as spokes spanning all ranges in the direction of the Sun (Holleman and Beekhuis, 2004; Peura, 2002). Seen from the Earth, the solar radio-emission disk subtends an angle of approximately 0.57° in diameter. The sampling settings of the XRAD weather radars result in an azimuthal resolution of ca. 1°. Hence, usually no more than one or two radial rays are affected by the solar signal in each PPI sweep. In general, the number of interferences occurring per day depends on the scanning strategy in combination with the solar trajectory and speed across the local sky, determined by the date and the site of the radar, the sensitivity of the receiver and the orography, among others. Plots in Figure 4.2 show the evolution of a Sun interference at sunset on the 16th of June 2013, as observed in the PDA radar displays. As time goes by and sunset evolves, the solar signal is detected at decreasing elevations, while the azimuthal position slightly changes.

The solar emission at centimetre wavelengths may be classified into three components attending to the timescale of its intensity variations (Tapping, 2001): a

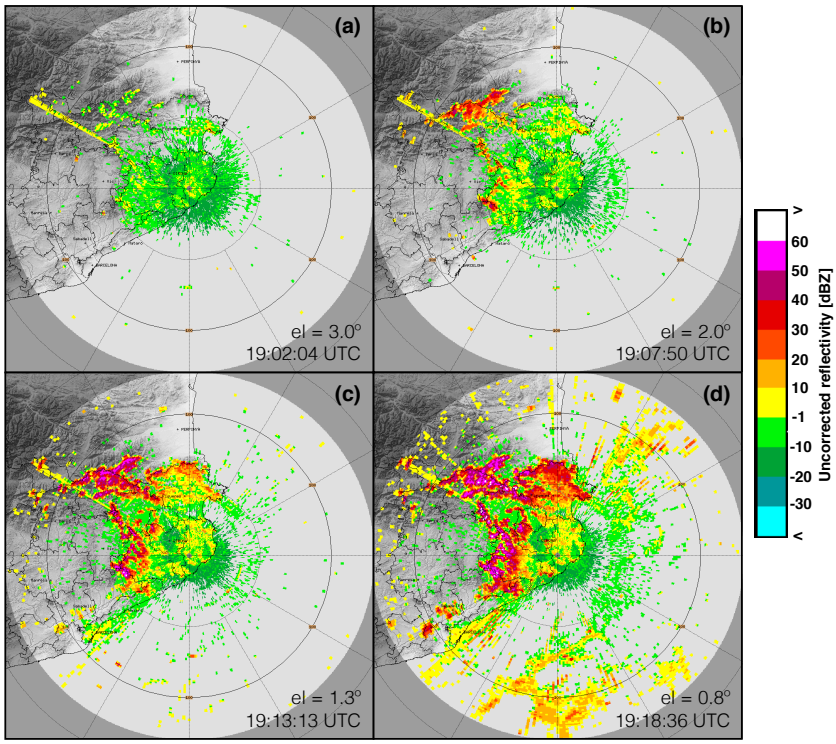

Figure 4.2: PDA radar displays of solar interferences observed in a series of PPI scans during sunset on 16 June 2013. The interferences appear as stripes in the direction of the solar position around 300° North.

rapidly-varying component with a timescale of seconds to minutes, generated by fast transient phenomena like solar flares; a slowly varying component with origin in active regions and a timescale of hours to decades; and an always present background component, the quiet-Sun (non-active) emission. Assuming that there are no transient phenomena taking place, only the quiet-Sun and the slowly varying components contribute to the solar signal detected by the weather radar. The time needed for the radar to complete a single radial ray scan is around a fourth part of a second (for a radial resolution of 1° and an antenna scan speed of $24°s^{-1}$). Therefore, the solar signal causing the interferences may be considered not only continuous in time but also constant in intensity. As introduced previously, these two characteristics as well as the proximity of the interference to the known position of the sun can be used to derive criteria that allow the identification of the radial rays affected by the solar signal in the PPI scans.

4.1.1 Identification

Since the weather radars are configured for operation with pulsed transmission, a continuous signal is interpreted by the processor as an echo power coming from all ranges, as seen for the solar interferences in Figure 4.2. A radial ray with a reflectivity value in all or most of its range gates constitutes a continuous interference candidate. Therefore, the fraction of range gates in the ray with a consistent signal is a main signature for identification of continuous interferences.

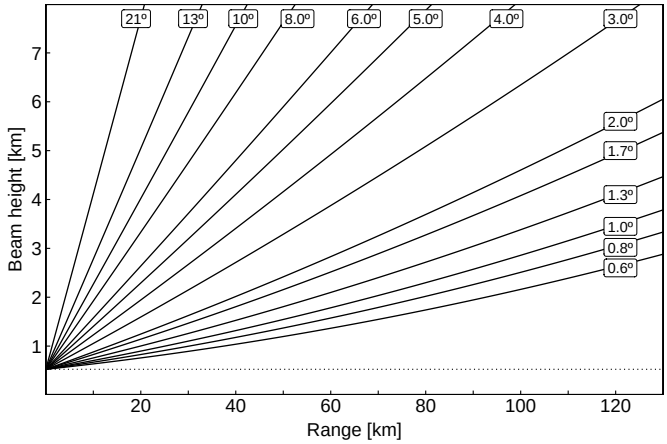

Figure 4.3: Height of the beam centre as a function of range along beam for the PDA radar for programmed scan elevations, calculated using the refraction k-model with $k = 4/3$.

The original Sun interference detection algorithm by Huuskonen and Holleman (2007) was designed to use the fraction of gates for ranges beyond 200 km as identification signature. The reason to focus on long ranges is that the detected signal is unlikely to come from precipitation or ground clutter echoes, due to the height the radar beam achieves. The choice of an appropriate minimum range threshold that ensures the absence of precipitation echoes depends on the elevation of the scan and is conditioned by the maximum range reached by the system. In typical midlatitude storms, echo heights can reach and easily exceed 8 km (Rigo et al., 2010). According to k-model beam propagation under standard conditions (Bean and Dutton, 1966; Doviak and Zrnič, 1984), in the case of the XRAD radar located at lowest height above sea level (the PDA radar at 525 m), the centre of the beam exceeds the 8 km altitude before reaching the maximum range of 130 km only for elevations of 3° and above, as shown in Figure 4.3. In this situation, setting a minimum range-height criterion would imply to exclude scanned elevations up to 3° from the analysis.

To avoid exclusion of the lowest elevations, the original identification methodology has been modified for application to mid range radar data (80-150 km), attending to the characteristics of the XRAD radar network. As explained in detail in the following, additional criteria based on robust statistical estimators are imposed in the solar interference detection process, excluding only those signatures dominated by ground clutter or precipitation echoes.

4.1.2 Adaptation to midrange observations

In the operational algorithm, the reflectivity data in RAW polar files is read on a daily basis and analysed radial by radial in search of solar interferences. In a first consideration, potential continuous signals are detected in raw data files by applying a loose range threshold for the calculation of the fraction of gates, in order to detect solar interferences in as many scanned elevations as possible. In particular, radial rays having a valid reflectivity value in 90 % or more of the range gates located further than 50 km away from the radar are selected, independently of their elevation. A valid reflectivity value means that a significant echo has been measured, with a reflectivity value above the minimum of −31.5 dBZ. The 50 km range threshold is chosen so that the gates close to the radar site most affected by ground clutter are skipped. Once a radial potentially affected by a solar interference is identified, the reflectivity values in dBZ units of each of its range gates are individually back-converted to power at antenna entrance in dBZ units through application of the radar equation as implemented in the processor (Vaisala, 2014b):

$$P = Z - \hat{C} - 20\log_{10} r - 2ar \,, \tag{4.1}$$

where the constant $\hat{C}$ includes the radar constant, the refraction coefficient (*cf.* Equation 1.2) and also the transmit line losses. The last two terms in Equation 4.1 relate to the propagation of radio-waves in the atmosphere and correspond, respectively, to the geometric and atmospheric attenuation corrections as a function of range r, with a the one-way gaseous attenuation coefficient.

The median value of the power of all range gates farther than 80 km away from radar site is calculated and recorded as the characteristic power at antenna port of the solar interference, $\overline{P_{\mathrm{det}}}$. The 80 km range threshold is selected to minimise the possibility of obtaining a biased median estimate by the presence of ground clutter or precipitation affected gates. As an example, in Figure 4.4, the along-range power values of two selected solar interferences are displayed. In both cases,

a constant power signal is revealed after conversion of the reflectivity values through Equation 4.1. For the solar interference in the bottom panel of Figure 4.4, ground clutter traces are found even beyond 80km. Since these traces are usually limited to relatively narrow range intervals, the median value of power calculated in their presence gives still an unbiased estimate of the constant solar signal.

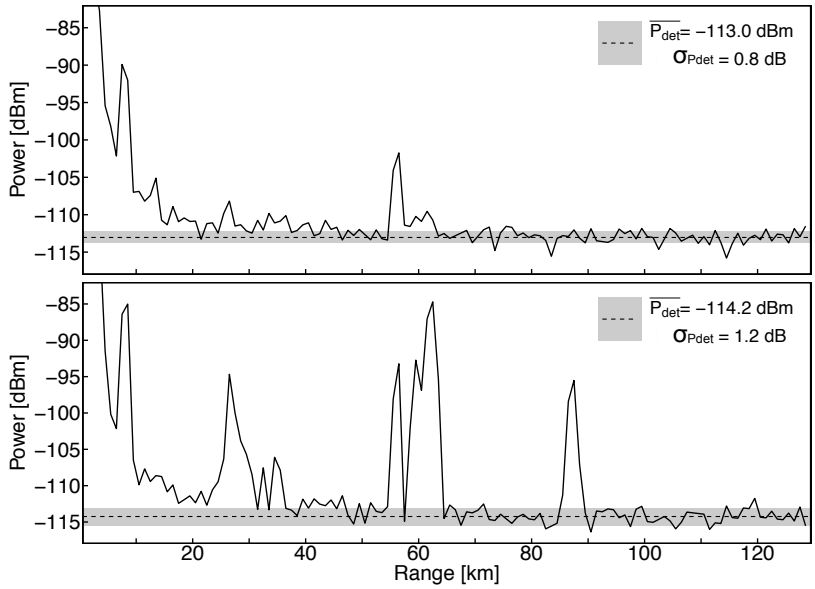

Figure 4.4: A-scope plots displaying the power at antenna entrance for two solar interferences detected on 16 June 2013 by the PDA radar at: (top panel) 1902UTC, 3° elevation and 299° azimuth and (bottom panel) 1907UTC, 2° elevation and 300°. The dashed horizontal line indicates the median characteristic power of the interference ($\overline{P_{\mathrm{det}}}$) and the shaded area encloses its $\pm\sigma_{P\mathrm{det}}$ interval estimated from the MAD, both calculated only for bins at ranges beyond 80 km.

At this point, a maximum threshold for the statistical deviation ($\sigma_{P\mathrm{det}}$) from the median is established. Interference radials with an estimated $\sigma_{P\mathrm{det}}$ of power below the threshold are kept for future processing steps. This constraint is designed to identify interferences resulting from constant signals; it allows to discard interferences strongly affected by ground clutter or precipitation echoes. If the gate power deviations derive only from random effects as expected for a constant signal, the $\sigma_{P\mathrm{det}}$-distribution is assumed to be normal. As a robust estimator of $\sigma_{P\mathrm{det}}$, the Median Absolute Deviation (MAD) of the bin-ensemble is used, scaled so that it conforms to the underlying distribution (Reimann et al., 2008).

An *ad hoc* analysis of the distributions of $\sigma_{P\mathrm{det}}$ values of solar interferences

collected during 12 months has led to the choice of a static maximum threshold of 2 dB for the MAD of power. In this analysis, only continuous interference signatures located within ±1° from solar position have been considered. As shown in Figure 4.5, the bulk of the $\sigma_{P\mathrm{det}}$ estimations lies, for all three radars, within an interval of (1.0 ± 0.5) dB values. The density distributions appear slightly skewed towards large $\sigma_{P\mathrm{det}}$ values and with several outlying observations. The PDA radar reveals a larger number of outliers, related to the presence of ground echoes beyond 80 km, as indicated by Figure 4.4, and to a greater influence of interfering RLAN signals (see Section 4.2 in the present chapter and Subsection 5.4.2 in Chapter 5).

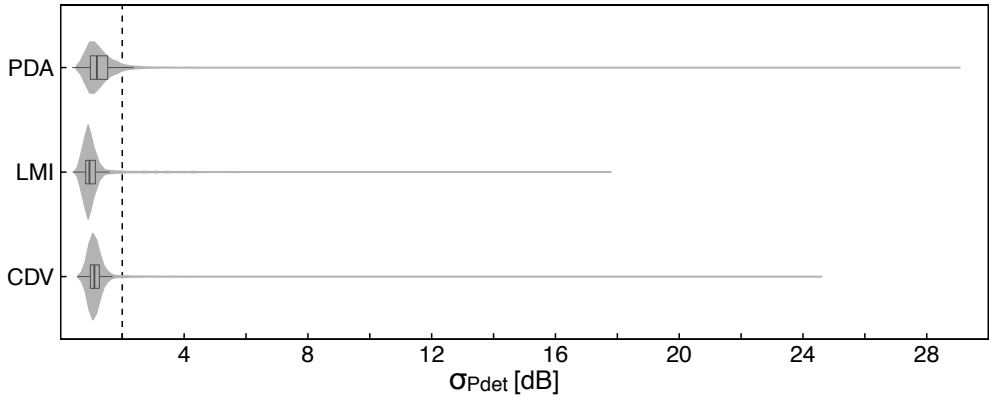

Figure 4.5: Box-plots of the $\sigma_{P\mathrm{det}}$ (calculated from the MAD of power) for solar interferences detected throughout 2013 for each of the radars conforming the operative XRAD. The boxes enclose the Inter-Quartile Range (IQR), while the whisker lines delimit outlier-free range (1.5 times the IQR). Shadowed shapes depict the corresponding distributions. The vertical dashed line indicates the maximum $\sigma_{P\mathrm{det}}$ threshold of 2 dB imposed in the identification of constant interferences.

4.1.3 Solar positioning

The last and definitive condition that discriminates solar interferences among the set of constant and continuous interferences is the relative position between the interference ray and the Sun; only interference rays located within ±5° from the actual solar position are considered. Recalling that the angular radio-emission width of the Sun is ca. 0.57° and assuming that the beamwidth of the antenna is typically close to 1°, the ±5° threshold is loose, but allows for the detection of the solar interferences in the presence of a significant antenna pointing bias.

The relative position is calculated as the difference between the centre of the

interference ray and the centre of the solar disk. Antenna readings at start $(\mathrm{az}_i, \mathrm{el}_i)$ and end $(\mathrm{az}_f, \mathrm{el}_f)$ of the measurement are read from raw data files and transformed to ray centre coordinates, $(\mathrm{az}_R, \mathrm{el}_R)$, and width, Δ_R, for practicality:

$$\begin{aligned} \mathrm{az}_R &= \frac{1}{2}\left(\mathrm{az}_i + \mathrm{az}_f\right) \\ \mathrm{el}_R &= \frac{1}{2}\left(\mathrm{el}_i + \mathrm{el}_f\right) \\ \Delta_R &= \mathrm{az}_f - \mathrm{az}_i \end{aligned} \tag{4.2}$$

The solar position, $(\mathrm{az}_S, \mathrm{el}_S)$, relative to the radar site is calculated using the astronomical equations given in WMO (2008) and local date, time, latitude and longitude information. Given the maximum local speed of the Sun across the sky, it has been estimated that the interference detection time needs to be accurate within 8 s to 10 s for an accuracy of 0.1° in the solar positioning. The time of the interference is estimated from the volume start time and the antenna scan velocity, using the known sweep number within the volume and ray position within the sweep in which the interference has been detected. The volume start time is the radar time at the start of the volume scan, being all XRAD radars synchronised with a common time server. The interference time estimation does not consider the time needed for the antenna to reach the nominal elevation once a sweep has been performed and the next one is to start, but the resulting timing error is estimated to be less than a couple of seconds.

Due to the effect of atmospheric refraction, the so calculated exoatmospheric solar elevation el_S may differ significantly from the solar elevation actually observed from the Earth's surface, i.e. the *apparent* elevation, el_S^a (Holleman and Huuskonen, 2013). The apparent elevation of the Sun may be expressed as the sum of the exoatmospheric elevation and the refraction angle τ_S:

$$\mathrm{el}_S^a = \mathrm{el}_S + \tau_S \,. \tag{4.3}$$

For the estimation of the refraction angle several empirical and theoretical formulas have been proposed (see Holleman and Huuskonen, 2013, and references therein). In the present case it has been calculated using the theoretical formulas derived in Holleman and Huuskonen (2013), using the recommended value of

$k = 5/4$ for the k-model constant and a reference surface refractivity $N_0 = 313$:

$$\tau_S = \frac{k-1}{2k-1}\cos(\mathrm{el}_S)\cdot \left[\sqrt{\sin^2(\mathrm{el}_S) + (4k-2)\left(\frac{N_0 \cdot 10^{-6}}{k-1} + \frac{H_0}{kR_E}\right)} - \sin(\mathrm{el}_S)\right] \quad , \tag{4.4}$$

where R_E is the Earth's radius. The height of the radar antenna above sea level H_0 has been included in Equation 4.4, but an accuracy error below 0.03° in the refraction angle is associated to neglecting a 910 m a.s.l radar height, i.e. the height of the highest XRAD radar, the LMI.

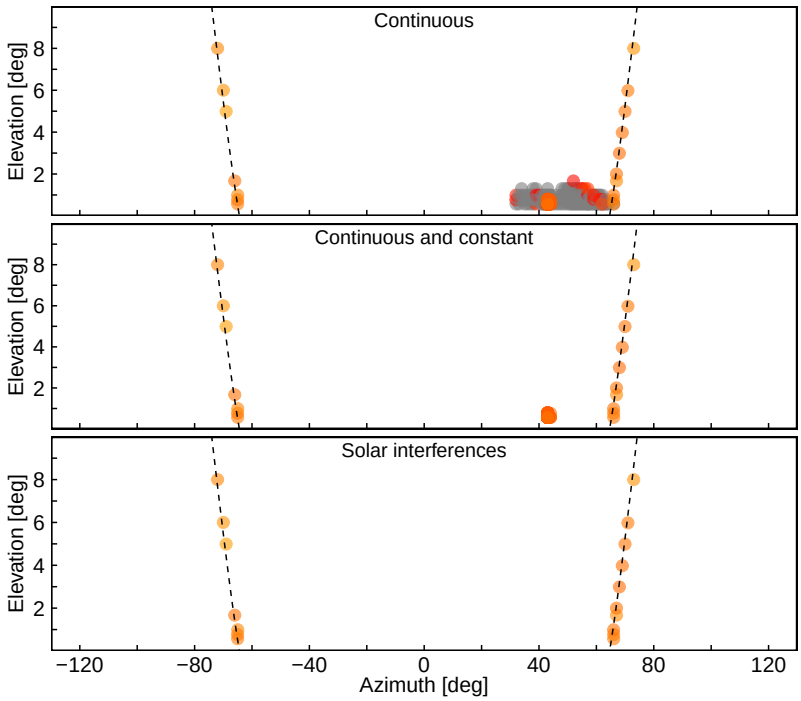

Figure 4.6: Elevation and azimuth position of interferences detected for the LMI radar on 13 May 2014. The colour fill of the observations is an indicator of the median power of the interference, ranging from yellow (−120 dBm) to dark red (−105 dBm). Interferences with a median power higher that −105 dBm are grey coloured. Dashed lines depict the local solar trajectory. Each panel shows the interferences detected in a particular step of the solar interference identification procedure: (top panel) continuous interferences after application of the fraction of valid gates threshold, (centre panel) constant interferences after application of the $\sigma_{P\mathrm{det}}$ threshold and (bottom panel) solar interferences after application of the Sun proximity threshold.

Holleman and Huuskonen (2013) tested the k propagation model to find that the best fitting effective k factor in the case of radio-waves emitted from exoatmospheric sources is closer to 5/4 than to the 4/3 factor used in the modelling of the radar beam propagation through the troposphere. In this case, the source being out of the atmosphere, the radiation propagation path is longer through higher atmospheric layers where the refractivity is lower, resulting in a smaller effective refractive index gradient. Using $k = 5/4$ and assuming an exponential humidity profile, a maximum accuracy error of 0.1° in the refraction angle calculation is expected from the study by Holleman and Huuskonen (2013).

Figure 4.6 illustrates the performance for the LMI radar on the 13 May 2014 in each of the stages in the solar interference identification procedure. The date chosen corresponds to a rainy day. In addition, the LMI radar was affected by a persistent RLAN interference at an azimuth of 43°. As exemplified in Figure 4.6 the continuity criterion based on the fraction of gates with a valid reflectivity value constitutes a good initial sieve but may also pass rays whose signal actually corresponds to precipitation. The constancy threshold applied to the $\sigma_{P\mathrm{det}}$ along range effectively removes these observations, leaving only the solar interferences and the non-solar interferences of constant nature. Finally, the solar proximity criterion effectively filters out these non-solar interferences, which are in most cases attributed to RLAN devices. The stages and thresholds applied in the solar interference identification algorithm are summarised in Figure 4.7. The figure also indicates how continuous and constant non-solar interferences detected by the algorithm, identified excluding the solar proximity criterion, are collected for monitoring and localisation of persistent RLAN interferences affecting the radars of the XRAD, as explained in detail in the upcoming section.

4.2 RLAN interferences

The decision made in the 2003 World Radio-communication Conference to open the 5150-5350 and 5470-5725 MHz frequency bands for the implementation of WAS (ITU-R 229, 2003) has compelled C-band radar operations to bandwidth sharing with RLAN. The weather radar community has addressed this issue by thoroughly analysing the characteristics of RLAN interferences and the degradation brought upon radar data (Brandão et al., 2005; Joe et al., 2005; Keränen et al., 2013) and also by detailing and proposing specific procedures for undisturbed coexistence (EUMETNET, 2008; Horváth and Varga, 2009).

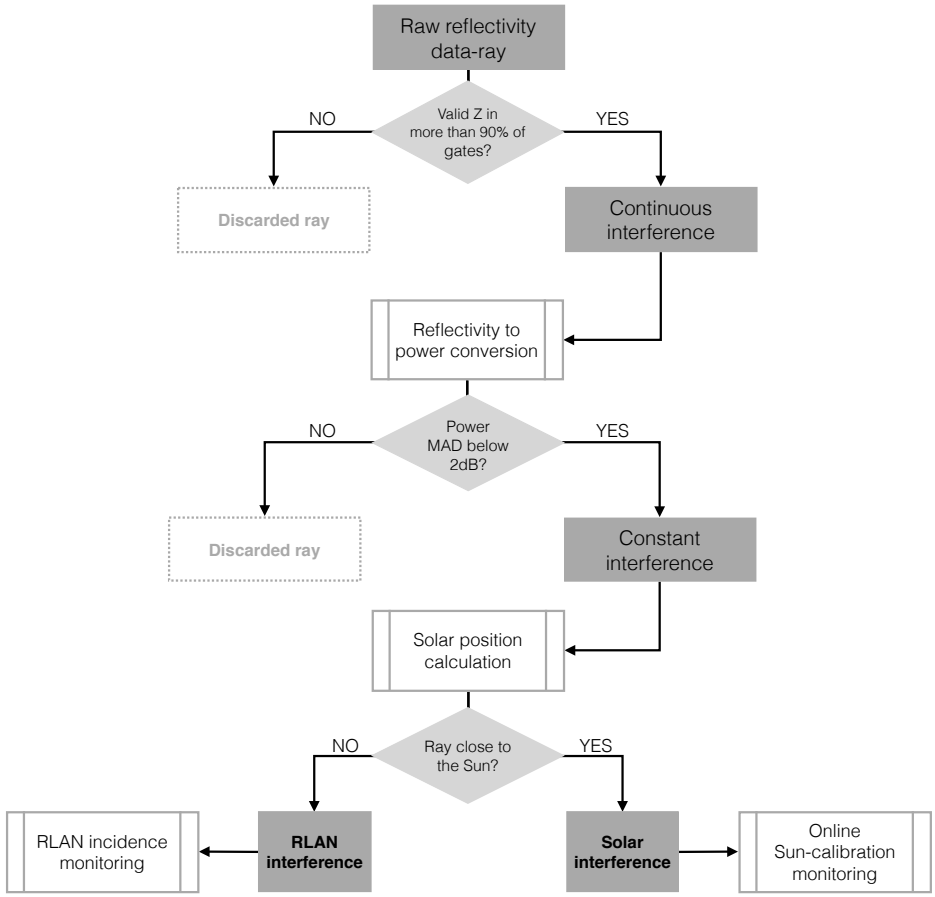

Figure 4.7: Identification of interferences resulting from continuous and constant external signals in raw reflectivity radar data and separation into solar and electronic origin for further processing with independent quality management purposes.

4.2.1 Bandwidth sharing

The radar bandwidth protection regulation against interference by secondary wireless devices relies in the incorporation by the latter of a Dynamic Frequency Selection (DFS) mechanism. The DFS mechanism searches for weather radar signals in shared frequency channels and, in case a radar signal is detected, the device is required to ensure channel avoidance and monitoring prior to bandwidth occupation. Within this framework, the EUMETNET (2008) recommendation issued a series of guidelines for the OPERA network members to ensure that weather radars ope-

rating in the C-band transmit a minimum number of DFS detectable signals over their duty cycle. As argued by Saltikoff et al. (2016), wireless traffic has significantly increased in the last decade and RLAN interferences are increasingly observed over the world. However, the effectiveness of the DFS protocol has revealed to be unsatisfactory, attributed to difficulties of the DFS algorithm to detect the wide variety of weather radar emission schemes but mainly due to non-compliant use of the wireless devices (Saltikoff et al., 2016).

The weather radar community is increasing efforts to develop methodologies that allow identification and mitigation of RLAN interferences. For instance, Rojas et al. (2012) showed that texture properties of selected dual-polarisation variables can be used to design a non-meteorological signature classifier, including radio-frequency signal interferences. More general approaches, applicable to single polarisation radars, rely on the distinctive features of RLAN interference for identification, either at the processing level (Keränen et al., 2013) or based on their visual appearance in weather radar imagery (Peura, 2002). Interference studies indicate that RLAN signal manifests at the radar receiver as additive uncorrelated noise, independently of modulation, power and packet inter-arrival time (Brandão et al., 2005). The RLAN signal adds to the noise of the radar decreasing the sensitivity and hampering the detection of weak targets (Joe et al., 2005). This also implies that, in most cases, recovering the relatively weak weather echo is not feasible. Under these circumstances, the weather radar community recommends individual operators to identify and monitor RLAN interferences to immediately and continuously report back to their corresponding National Radio Administration, responsible for the regulation of non-compliant devices.

With regard to the status of radio-electric network, the XRAD has to comply with the legislation that regulates the use of the radio-electric domain. In accordance with it, the XRAD operates within the 5600-5650 MHz frequency sub-band and keeps both its equipment and operation characteristics certified by the concerning organisations. In addition, the XRAD scanning settings fulfil the requirements stated in EUMETNET (2008) that ensure the transmission of a minimum number of DFS detectable signals.

Each of the XRAD radars has a reserved channel within the 5600-5650 MHz band, which is assigned for meteorological radar use by the National Frequency Assignment Chart (CNAF). The validity of the expedient that legally guarantees the exclusive use of these channels by the XRAD according to the specified frequencies and range scopes listed in Table 4.1 is annually updated through the payment of the corresponding taxes. The competent authority, responsible of ensuring that

the use of the radio-electric spectrum is made according to the current legislation is the General Telecommunications Management (DGTEL) located in Barcelona, subject to the Industry, Energy and Tourism Ministry.

Table 4.1: Frequency channels of the public radio-electric spectrum reserved for the meteorological radars of the XRAD and range scope of the corresponding channel reserves.

Radar	Assigned frequency [GHz]	Range scope [km]
CDV	5.632	250
LMI	5.610	250
PBE	5.648	250
PDA	5.625	250

4.2.2 Monitoring RLAN interference incidence in the XRAD

Any wireless operator within the radar horizon and transmitting directly in the reserved frequency or which occupies partially the radar emission band generates an interfering signal at the radar receiver. As illustrated in Figure 4.8, these interfering signals are often recognisable in operational PPI images. Due to the high directivity of radar antennas, the disturbance is limited to an specific azimuth sector around the position of the external emitter, whose width generally depends on the proximity to the radar. If the emission is strong the disturbance can also be detected by the radar antenna pattern side lobes (Joe et al., 2005). Depending on the throughput of the external emitter, the interference signal will appear continuously or intermittently along the affected radial(s) (Keränen et al., 2013).

As anticipated in Section 4.1, non-solar interferences of continuous and constant nature are also collected and stored during the daily application of the solar interference identification algorithm for further monitoring and localisation of persistent RLAN interferences affecting the radars of the XRAD. The basic monitoring analysis consists on accumulating, depending on the azimuth affected, RLAN interferences detected during a significative time period, typically one month. In this way, statistics on the incidence of each of the interferences are derived and information about the location of persistently interfering operators is extracted. Figure 4.9 shows the histogram output of the RLAN monitoring application for the XRAD

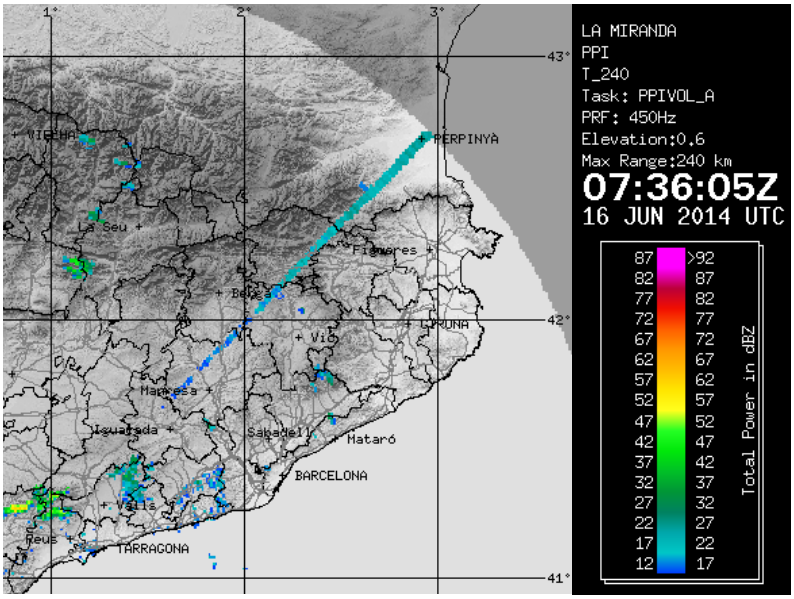

Figure 4.8: Example of persistent RLAN interference recognisable at an azimuth of 43° North in an operational PPI reflectivity image for the LMI radar on the 16 June 2014.

during May 2014, for the lowest elevation of 0.6°. The incidence is quantified by the percentage of affected sweeps out of the total corresponding to the selected elevation. A second output of the monitoring routine is a map indicating, as in the case of the histograms, the frequency of incidence of each of the interferences. As shown in Figure 4.10, these plots are very useful for comparing the azimuth position of the interferences with known locations of RLAN nodes.

The information on incidence and positioning of persistent RLAN interferences provided by the histograms and corresponding maps is reported to the DGTEL competent authority. If necessary, the information on the interferences stored by the identification algorithm allows to perform additional analyses such as incidence by hour of the day or by elevation. The DGTEL administration, in response to these reports, sends technicians to perform *in-situ* measurements at each of the radars in search of the particular operator interfering in the reported azimuth regions. If the interfering device is identified, the operator is contacted and compelled to completely abandon the reserved channel and to eliminate any possible generation of adjacent frequency harmonics that may enter the channel and generate unwanted noise. In case the operator were emitting in a frequency multiple of that of the radar,

compliance with the in-force legislation regarding emission power is required.

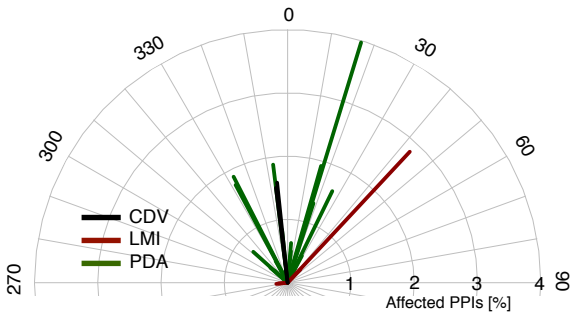

Figure 4.9: Polar histogram of the frequency of incidence of constant and continuous interferences by external emitters during May 2014 for each of the operative XRAD radars. The frequency is expressed as the percentage of sweeps affected during the studied period.

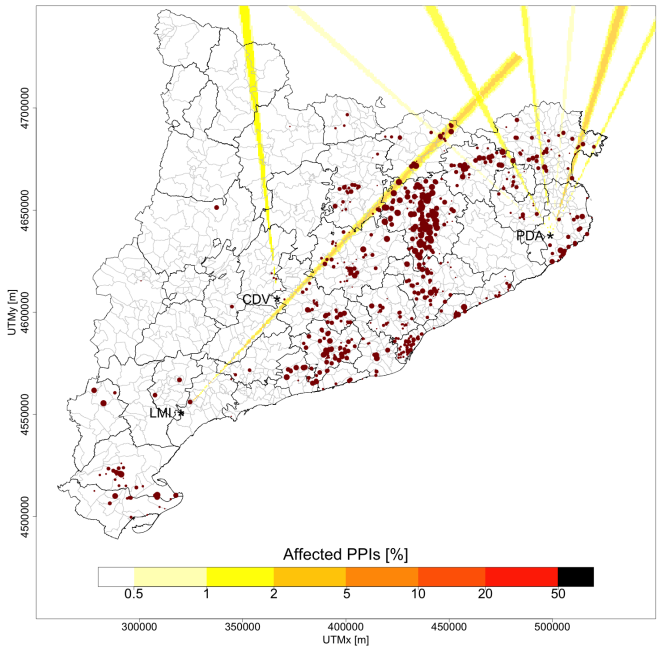

Figure 4.10: Map of the frequency of incidence in the XRAD of constant and continuous interferences by external emitters during May 2014. The location of the operative XRAD radars is indicated by an asterisk. The interferences are colour coded as a function of the percentage of sweeps affected during the studied period. The dots indicate the position of the RLAN nodes operated in the Catalonia region by the *guifi.net* open community telecommunications network (https://guifi.net/en/).

4.3 Conclusions

Interferences from external radiowave sources can cause a severe quality degradation of weather radar estimates. In particular, interferences from Wireless Local Area Network (WLAN) devices including RLAN, emitting within or close to the radar frequency band have become a major quality issue in the last decade for weather radars all around the world. RLAN interferences insert high levels of noise in the radar reception chain and constitute a handicap for the detection of weak weather echoes. Given the difficulty for recovering the weather signal in the contaminated azimuths, the best practice up to date regarding RLAN interferences is to operationally identify and monitor the interferences.

Another external radiowave emitter that interferes with the radar operation is the Sun. However, interferences from the Sun, which are daily encountered in radar imagery during sunrise and sunset, can give very useful information regarding the radar system calibration status. Identification of these solar interferences in radar operational data on a daily basis is the first stage of a quality control method for combined online monitoring of weather radar antenna pointing biases and receiver calibration which was first presented in Holleman and Beekhuis (2004). In this chapter the solar interference identification algorithm proposed in the cited work has been adapted for application to midrange radar data (80 km to 150 km). Originally, the algorithm was designed for operation with long-range radar scans and relied in the continuity characteristic of the solar emission for identification. In the case of the XRAD the use of shorter range scans poses additional difficulties with the detection of solar interferences and characterisation of their power. Hence, to discard precipitation signatures and to obtain unbiased estimates of the solar interference power even in the presence of traces of ground clutter or precipitation, an additional maximum along-range statistical deviation threshold for the power of the interference is imposed in the detection process. This condition exploits the constant nature of the solar emission. The threshold is set to 2 dB, attending to the typical deviations presented by solar interference observations as derived from an *ad hoc* analysis. The so adapted identification algorithm has proven effective to detect all interferences of continuous and constant nature. Indeed, the algorithm is able to detect both solar interferences and persistent and constant RLAN interferences, which may be differentiated by the proximity of the interference to the solar position, derived from astronomical formulae. Solar interferences are stored for further use in the solar monitoring methodology explained in detail in the upcoming

Chapter 5. Conversely, RLAN interferences can be cumulatively stored in order to determine the location of the emitting operators and to monitor the incidence of these harmful emissions. This is key information to appeal to the local administrations responsible for preserving the reserved frequencies of the weather radars and for a case-by-case identification and regulation of the individual devices causing the interference.

5

Online Sun-monitoring

* Section 5.1 to Section 5.4 of the present chapter have been adapted from: Altube, P., J. Bech, O. Argemí and T. Rigo, 2015: Quality control of antenna alignment and receiver calibration using the sun: adaptation to mid range weather radar observations at low elevation angles. *J. Atmos. Oceanic Technol.*, 32, 927-942, doi: 10.1175/JTECH-D-14-00116.1

The use of weather radars in national and global networks has increased awareness and efforts towards the establishment of common procedures and standards in data quality and calibration (Saltikoff et al., 2010; Huuskonen, 2001; Huuskonen et al., 2009; Chandrasekar et al., 2014). Within this framework, the Sun is regarded as a well-known, reliable and worldwide available reference target that can be used for a number of calibration purposes.

After the first proposal by Whiton et al. (1976), the use of the Sun as reference microwave source for offline inspection of weather radar system gain and antenna pointing accuracy is currently of widespread employment and has been extensively discussed in the literature; see for instance Frush (1984), Pratt and Ferraro (1989) and Eastment et al. (2001). Tapping (2001) introduced the 10.7 cm wavelength solar radio emission measurements at the Dominion Radio Astrophysical Observatory (DRAO, Penctincton, Canada) and described their adaptation to other frequencies for the gain estimation of small beamwidth antennas when statically pointing at the Sun. Leskinen et al. (2002) estimated the antenna pointing bias and beamwidth by manually fitting a theoretical model to power observations collected in an offline passive scan through the centre of the Sun.

Darlington et al. (2003) established criteria for automated identification, at long ranges, of solar signatures detected in weather radar volumetric scans. They showed that, through polynomial fits of the individual solar interferences, statistical information about the antenna pointing bias in azimuth could be retrieved on a regular basis. Holleman and Beekhuis (2004) reinforced the criteria for identification of the solar signatures and presented a fully automatic procedure for online and simultaneous monitoring of weather radar receiver chain calibration and of antenna alignment in both azimuth and elevation. This online Sun-monitoring method consists on fitting, to daily detected solar interferences, a theoretical model for the power of the solar signal detected by an operational scanning radar. The paper was the precursor of a series of works by Huuskonen and Holleman (2007) and Holleman et al. (2010b) in which the method was consolidated by addressing the difficulties in solar positioning due to the effect of atmospheric refraction and by a more detailed insight into the theoretical model. Further developments and applications of the technique are tackled in Muth et al. (2012), Frech (2009), Holleman et al. (2010a), Frech (2013) and Huuskonen et al. (2014).

The Sun-monitoring method by Holleman and Beekhuis (2004) has been implemented and is currently operational for the XRAD network, constituting a handy tool for remote and daily monitoring of the quality of both the receiver chain calibration and antenna alignment accuracy. This has been made possible adapting

the solar interference identification algorithm to mid range radar data, as detailed in the previous Chapter 4. The present chapter reviews the operation of the Sun-monitoring method and describes its implementation for the XRAD. In particular, a non-iterative and simple procedure is proposed, designed to remove strongly outlying observations which often correspond to non-solar interferences. In a thorough theoretical derivation, the validity ranges of the physical model characterising the solar interferences are explicitly defined and an equation for estimation of the effective scanning width in reception is provided. The results of applying the Sun-monitoring technique to operational data obtained with three XRAD radars during one year reveal the sensitivity of the method to changes in the antenna pointing accuracy and receiver calibration. The performance of the proposed methodology under the effects of the presence of ground clutter and RLAN interferences is discussed in the results presented. A comparative study on the goodness of fit between a three and a five-parameter model inversion analyses the stability of the calibration parameters retrieved for two selected XRAD radar systems, considering the dissimilar information content of the observations collected by each radar. Along these lines, the key aspects to be considered in order to ensure the accuracy of the method results are investigated through a performance study that reproduces the Sun-monitoring methodology under controlled conditions.

5.1 Methodology

Solar interference observations resulting from the automatic detection process detailed in Chapter 4 are input for a theoretical model inversion. The power of the solar signal is modelled considering the radar antenna sensitivity pattern and its continuous scanning motion. The derivation of the solar interference model is explained in detail in the upcoming Section 5.2. The resulting model is a 2-dimensional Gaussian function for the detected power in W units, p_{det}, dependent of the relative displacement between the centre of the interference ray and the Sun-disk centre (*cf.* Huuskonen and Holleman, 2007):

$$p_{\mathrm{det}} = l_{\mathrm{gas}}\, l_{\mathrm{scan}}\, p_{\mathrm{TOA}}\, \exp\left\{-4\ln 2\left[\frac{(x-x_0)^2}{\Delta_x^2} + \frac{(y-y_0)^2}{\Delta_y^2}\right]\right\}, \tag{5.1}$$

where the unit-less factor l_{gas} is the transmissivity of the gaseous atmosphere and l_{scan} is a power loss factor due to the convolution between the antenna sensitivity pattern and the solar disk while in scanning motion. The calibration parameters to

be retrieved are: the solar power at the Top Of the Atmosphere (TOA), p_{TOA}; the azimuth and elevation solar image widths, Δ_x and Δ_y; and the systematic antenna pointing biases in azimuth and elevation, x_0 and y_0. The independent variables (x, y) represent the relative position coordinates in azimuth and elevation between the centre of the interference ray and the position of the solar disk centre:

$$\begin{aligned} x &= \mathrm{az}_R - \mathrm{az}_S \\ y &= \mathrm{el}_R - \mathrm{el}_S^a \,. \end{aligned} \tag{5.2}$$

As described in Chapter 4, Subsection 4.1.3, the coordinates of the ray centre (az_R, el_R) are available from the antenna positioning system readings (see Equation 4.2) while the position of the solar disk centre (az_S, el_S^a) may be calculated using astronomical formulae.

Equation 5.1 constitutes a, generally overdetermined, nonlinear inverse problem. However, in the case of a Gaussian function fit, a linear treatment and direct inversion by means of a Linear Least Squares (LLS) procedure is possible (Caruana et al., 1986; Holleman and Beekhuis, 2004), taking into account that the errors in the observations may be assumed multiplicative (Guo, 2011). Logarithmic transformation of the Gaussian function yields a 2-dimensional parabolic model:

$$P = P_{\mathrm{det}} - L_{\mathrm{gas}} = a_x\, x^2 + a_y\, y^2 + b_x\, x + b_y\, y + c\,, \tag{5.3}$$

where P is the power in dBm units of the solar signal corrected for the atmospheric gaseous attenuation, with:

$$P_{\mathrm{det}} = 10 \log_{10} p_{\mathrm{det}}\,, \tag{5.4}$$

$$L_{\mathrm{gas}} = 10 \log_{10} l_{\mathrm{gas}}\,. \tag{5.5}$$

The quadratic form in Equation 5.3 represents a concave down parabola with its maximum located at the same position as the maximum of the original Gaussian function. The model is linear in the parameters a_x, a_y, b_x, b_y and c, which can be retrieved in a LLS fit and are related to the calibration parameters through:

$$\begin{aligned} a_x &= -\frac{40 \log_{10} 2}{\Delta_x^2} \\ a_y &= -\frac{40 \log_{10} 2}{\Delta_y^2} \end{aligned} \tag{5.6}$$

$$b_x = 80 \log_{10} 2 \cdot \frac{x_0}{\Delta_x^2}$$
$$b_y = 80 \log_{10} 2 \cdot \frac{y_0}{\Delta_y^2} \tag{5.7}$$

$$c = P_{\mathrm{TOA}} + L_{\mathrm{scan}} - 40 \log_{10} 2 \cdot \left(\frac{x_0^2}{\Delta_x^2} + \frac{y_0^2}{\Delta_y^2} \right) . \tag{5.8}$$

The calibration parameters can be derived from the parameters retrieved in the linear fit through reversion of the set of equations from Equation 5.6 to Equation 5.8. It must be noted, though, that physically meaningful results require that the retrieved a_x and a_y parameters are negative. Comparison of the P_{TOA} estimation with reference data from a solar observatory allows the assessment of the receiver calibration status.

5.1.1 Gaseous atmospheric attenuation

Prior to model inversion, the detected power of each solar interference has to be corrected for the gaseous attenuation along the signal path through the atmosphere. In the microwave region, molecular scattering can be neglected and, for frequencies below 10 GHz, the atmospheric extinction is dominated by oxygen and water vapour molecular absorption:

$$l_{\mathrm{gas}}(\lambda) = \exp \left\{ - \int_{\mathrm{path}} \left[\sigma_{O_2}(\lambda)\, n_{O_2}(s) + \sigma_w(\lambda)\, n_w(s) \right] ds \right\} , \tag{5.9}$$

where σ_{O_2}, σ_w and n_{O_2}, n_w are the spectral absorption cross sections and along-path molecular densities of oxygen and water vapour, respectively.

The magnitude of the gaseous attenuation of a solar signal that has traversed the whole atmosphere can be estimated from integration of Equation 5.9, assuming a model atmosphere of z_0 equivalent height with constant effective oxygen and water vapour densities. In this way, l_{gas} depends uniquely on the length of the optical path through the atmosphere $r(z_0, \mathrm{el}_S)$:

$$l_{\mathrm{gas}}(\lambda, z_0, \mathrm{el}_S^a) \approx \exp \left\{ - \left[\sigma_{O_2}(\lambda)\, \bar{n}_{O_2} + \sigma_w(\lambda)\, \bar{n}_w \right] r(z_0, \mathrm{el}_S^a) \right\} . \tag{5.10}$$

Under these approximations, the gaseous attenuation correction factor for the power of the solar interference, L_{gas}, introduced in the previous Section 5.1 is given

by:

$$L_{\text{gas}}(\lambda, z_0, \text{el}_S^a) = 10\log_{10}(l_{\text{gas}}) = -a(\lambda)\, r(z_0, \text{el}_S^a)\,, \tag{5.11}$$

where $a(\lambda)$ is the gaseous attenuation coefficient in $\text{dB}\,\text{km}^{-1}$ and accounts for the absorption cross sections and effective densities of oxygen and water vapour molecules. The attenuation coefficient for a 5 cm wavelength signal is estimated in $0.08\,\text{dB}\,\text{km}^{-1}$ (see Rinehart, 1997, and references therein).

The gaseous attenuation has to be calculated and corrected for each solar interference because the length of the optical path depends on the apparent elevation of the Sun. Considering that the solar signal traverses the whole height of the model atmosphere, the path length can be estimated through the optical propagation k-model as:

$$r(z_0, \text{el}_S^a) = R_{\text{eff}} \left[\sqrt{\sin^2(\text{el}_S^a) + \left(\frac{z_0 - H_0}{R_{\text{eff}}}\right)^2 + 2\left(\frac{z_0 - H_0}{R_{\text{eff}}}\right)} - \sin(\text{el}_S^a) \right]\,, \tag{5.12}$$

where $R_{\text{eff}} = kR_E$ is the equivalent Earth's radius, with R_E the Earth's radius and H_0 is the height of the radar above mean sea level. The equivalent height of the atmosphere in the constant-density model is chosen such that the integrated density is conserved, obtaining a value of $z_0 \approx 8.4\,\text{km}$ for an atmosphere in hydrostatic equilibrium (Huuskonen and Holleman, 2007; Holleman et al., 2010b).

The k coefficient in the k-model is related to an effective constant refractive index gradient of the atmosphere. For modelling the propagation of the radar microwave signal, the refractive index gradient in the first kilometre or two of the atmosphere, $-1/4R_E$, is generally used, which yields a $k = 4/3$ (Doviak and Zrnič, 1984). However, as pointed out in the previous chapter, Holleman and Huuskonen (2013) have found that a factor of $k = 5/4$ might be more accurate for modelling the propagation in the case of signals from exoatmospheric sources like the Sun. In the refraction angle estimation for the calculation of the Sun's apparent elevation presented in Chapter 4, Subsection 4.1.1, the choice of the k coefficient is fundamental, as it can lead to inaccuracies of more than 0.1° in the solar positioning (Holleman and Huuskonen, 2013). In the case of the beam path length estimation, although the inaccuracy due to the choice of k may reach 50 km for the lowest elevations, given the small attenuating efficiency of molecular oxygen upon centimetre wavelength signals, the maximum possible accuracy error in the estimation of L_{gas} is below 0.5 dB for a 5 cm wavelength radar, which is the precision of the radar data. Moreover, this error is lower than 0.06 dB for elevations above 3°.

5.1.2 Reference solar flux

The solar flux data measured at the Dominion Radio Astrophysical Observatory (DRAO) and distributed by the National Research Council of Canada (DRAO, 1990) is used as reference for assessment of the receiver-chain calibration.

The DRAO database provides the disk-integrated solar flux density at the TOA measured at 10.7 cm wavelength, $F_{10.7}$. The conversion of 10.7 cm solar flux measurements to other radio frequencies relies on the separation of the integrated flux density into two distinct components (Tapping, 2001): a quiet-Sun background component at the desired wavelength and a slowly-varying component, which is shape-stable to changes in wavelength and whose absolute value may be determined through an appropriate scaling factor. The integrated solar flux density at 5 cm given in Solar Flux Units (SFU), F_5, may be estimated from the DRAO reference flux $F_{10.7}$ using the corresponding values of the scaling factor and quiet-Sun components, tabulated in Tapping (2001):

$$F_5 = 0.71\ (F_{10.7} - 64) + 126\,. \tag{5.13}$$

For a direct comparison of the estimated P_{TOA} with the reference power in dBm units, P_{DRAO}, multiplication by the receiver bandwidth, $\Delta\omega$ [Hz], and antenna effective area, A_{eff} [m^2], together with a change of units has to be applied to the reference solar flux:

$$P_{\mathrm{DRAO}} = 10 \log_{10} \left(\frac{1}{2}\, \Delta\omega\, A_{\mathrm{eff}}\, F_5\, 10^{-22} \right)\,. \tag{5.14}$$

The 1/2 factor in Equation 5.14 is introduced to consider that the radar is sensitive to a single polarisation direction in reception (e.g. horizontally polarised radiation in the case of single-polarisation radars) while the Sun is an unpolarised source. The effective collection area of the antenna is defined through the along-axis antenna gain, g, and the radar wavelength, λ (Doviak and Zrnič, 1984):

$$A_{\mathrm{eff}} = g\lambda^2/4\pi\,. \tag{5.15}$$

5.1.3 Inversion approach

The main calibration parameters to be retrieved in the inversion of the theoretical model are the solar power at the TOA (P_{TOA}) and the systematic antenna pointing biases in azimuth and elevation (x_0, y_0). The other two model parameters, that is,

the solar image widths in azimuth and elevation (Δ_x, Δ_y), arise from the convolution of the antenna sensitivity pattern with the solar emission disk and are related to the antenna beamwidth and solar-disk diameter. Therefore, the values of the solar image widths are known or can be estimated, as detailed in the upcoming Section 5.2. Based on this parameter classification, two different approaches to the inversion are possible: a full-parameter quadratic function fit, considering all 5 parameters unknown as described in Section 5.1 (5P model); and a three-parameter linear function fit with fixed Δ_x and Δ_y (3P model), in which the quadratic terms in Equation 5.3 are treated as constants for each of the observations.

Huuskonen and Holleman (2007) proposed the latter approach as optimal for improvement of the stability of the fit. Since the quality of the observational data and its information content are variable (depending on the radar system characteristics, on environmental factors and on the combination of the scanning strategy and solar motion), a lower number of model parameters are more likely to be independently determined by the collected data in the inversion. On the other hand, fixing the values of the widths may have an effect on the goodness of the fit and hence in the accuracy of the parameter estimates. Also, Huuskonen et al. (2010) and Huuskonen et al. (2014) pointed out that the width estimates from the 5P model fit may give additional information on the radar system performance and on the pointing stability of the antenna.

5.2 Sun image width estimation

In this section, the derivation of the theoretical model for solar interference observations is presented. The assumptions undertaken in each derivation step are examined in detail with the aim to provide an explicit formal framework for estimation of the expected solar image widths in azimuth and elevation, Δ_x and Δ_y, based on the radar antenna characteristics and scanning parameters. As pointed out in Subsection 5.1.3, knowledge of the expected or nominal width values is essential for the application of the 3P model inversion and for extraction of additional information in comparison with the widths estimated in a full 5P model inversion.

During the scan process, the weather radar repeats its pulse emission-reception sampling consecutively while the antenna is in motion. The derivations henceforward assume that the antenna motion is azimuthal and that solar interferences are collected in PPI scans. A radial ray in a PPI scan corresponds to the collection of a user defined number of pulse samples and hence, its angular resolution depends on

the number of samples and the antenna rotation speed. In the case of solar interferences, the signal at the receiver has, ideally, no contribution from the pulse-echo and corresponds only to solar emission. The derivation of the solar interference model is divided in two steps; first, the detected solar power fraction for a single sample is computed as a function of the angular distance between the antenna axis and the Sun-disk centre and then, this power fraction is integrated for the number of samples collected in a radial ray, taking into account that, with the azimuthal motion, the antenna-Sun angular distance changes from sample to sample.

5.2.1 Detected solar power in a single pulse-sample

The solar power fraction detected in a single reception sample indexed by j (p^j_{det}), is quantified by the convolution between the solar power flux pattern $S(\phi,\theta)$ and the antenna sensitivity pattern $f(\phi-\phi^0_j,\theta-\theta^0)$ functions:

$$p^j_{\text{det}} = l_{\text{gas}}\Delta\omega\, A_{\text{eff}} \int_{-\pi}^{\pi}\int_{-\pi/2}^{\pi/2} S(\phi,\theta)\, f(\phi-\phi^0_j,\theta-\theta^0)\, \cos\theta\, d\phi\, d\theta\,, \tag{5.16}$$

where (ϕ,θ) denote azimuthal and zenithal (spherical) coordinates and (ϕ^0_j,θ^0) give the instantaneous position of the antenna radiation field centre in a reference system with origin in the radar and with its reference axis pointing at the Sun-disk centre, as depicted in Figure 5.1. The l_{gas} factor is the transmissivity of the gaseous atmosphere described in Subsection 5.1.1, $\Delta\omega$ is the receiver bandwidth and A_{eff} is the effective collection area defined in Equation 5.15.

For most applications, the solar power pattern function for microwave emission may be modelled as a uniform disk of Δ_S diameter and S_0 integrated power flux density in $\frac{\text{W}}{\text{m}^2\,\text{s}}$ units (Tapping, 2001):

$$S(\phi,\theta) = \frac{4S_0}{\pi\Delta_S^2} \quad \text{for: } (\phi,\theta) \in \left[-\frac{\Delta_S}{2},\frac{\Delta_S}{2}\right]. \tag{5.17}$$

In turn, the antenna sensitivity pattern function, assumed symmetric and normalised for unity axial gain, can be represented as a 2-dimensional Gaussian, with Δ_B the 3-dB beamwidth (Probert-Jones, 1962):

$$f(\phi-\phi^0_j,\theta-\theta^0_j) = \exp\left[-4\ln 2\frac{(\phi-\phi^0_j)^2+(\theta-\theta^0)^2}{\Delta_B^2}\right]. \tag{5.18}$$

Variation intervals of (ϕ,θ) are small enough, with Δ_S =0.57°, to assume the

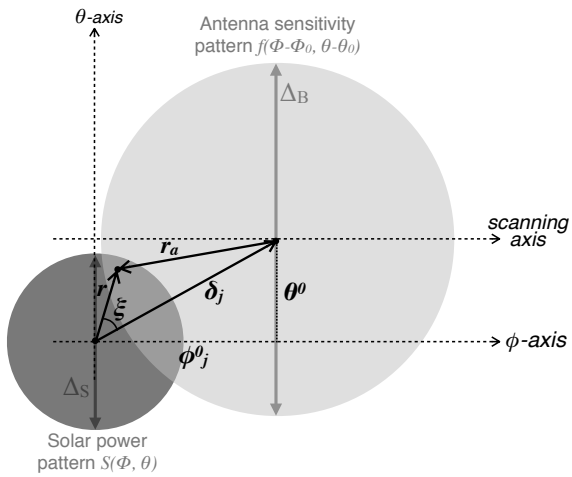

Figure 5.1: Instantaneous overlapping of the antenna beam sensitivity pattern and the solar disk in a plane perpendicular to the beam axis. Coordinates and angles relevant for the computation of the detected power fraction in the convolution of the antenna and solar patterns are explicitly drawn.

integration region of the convolution to be lying in a plane. Hence, plane trigonometry instead of spherical one may be applied. Integration of Equation 5.16 with Equation 5.17 and Equation 5.18 is simplified considering the antenna and the solar pattern functions each in a polar reference system of their own (Holleman et al., 2010b):

$$S(r) = \frac{4S_0}{\pi\Delta_S^2} \quad \text{for } r \leq \frac{\Delta_S}{2} \,, \tag{5.19}$$

and:

$$f(r_a) = \exp\left(-\frac{4\ln 2}{\Delta_B^2} r_a^2\right) \,, \tag{5.20}$$

where r and r_a are the radial distances from any point of the solar disk and the antenna patterns to their respective centres, as sketched in Figure 5.1. The expression in Equation 5.20 may be written in terms of the solar polar coordinates (r, ξ) applying the cosine theorem:

$$r_a^2 = r^2 + \delta_j^2 - 2\,\delta_j\, r \cos\xi \,, \tag{5.21}$$

where δ_j is the relative displacement between the Sun-disk centre and the antenna axis. After these considerations, the convolution integral in Equation 5.16 trans-

forms into:

$$p_{\text{det}}^{j} = l_{\text{gas}}\, p_{\text{TOA}}\, I(\delta_j)\,, \tag{5.22}$$

where the solar power at the TOA in W units is given by (*cf.* Equation 5.14):

$$p_{\text{TOA}} = \Delta\omega\, A_{\text{eff}}\, S_0\,, \tag{5.23}$$

and with:

$$I(\delta_j) = \frac{4}{\pi\Delta_S^2} \int_0^{\frac{\Delta_S}{2}} \int_0^{2\pi} \exp\left[-\frac{4\ln 2}{\Delta_B^2}\left(r^2 + \delta_j^2 - 2\,\delta_j\, r\cos\xi\right)\right] r\, dr\, d\xi\,. \tag{5.24}$$

An exact analytical solution of the convolution integral in Equation 5.24 expressed using elementary functions is not possible. Holleman et al. (2010b) proposed an approximate solution, obtained equalling to one the cosine exponential term in a first order Taylor approximation:

$$p_{\text{det}}^{j} = l_{\text{gas}}\, l_0\, p_{\text{TOA}}\, \exp\left(-4\ln 2\, \frac{\delta_j^2}{\Delta_B^2}\right)\,, \tag{5.25}$$

with:

$$l_0 = \frac{1}{\ln 2}\, \frac{\Delta_B^2}{\Delta_S^2} \left[1 - \exp\left(-\ln 2\, \frac{\Delta_S^2}{\Delta_B^2}\right)\right]\,. \tag{5.26}$$

In the present derivation, $I(\delta_j)$ has been numerically integrated for varying antenna beamwidths using the adaptive Genz-Malik algorithm (Genz and Malik, 1980), implemented in *cubature* library for R software (Johnson and Narasimhan, 2015). The computations indicate that, for beamwidths greater than approximately 0.3°, the detected power in a single sample p_{det}^{j} may indeed be approximated by a Gaussian function analogous to the one proposed in Equation 5.25, but with a convolution width Δ_C which is slightly larger than the Δ_B antenna beamwidth:

$$p_{\text{det}}^{j} = l_{\text{gas}}\, l_0\, p_{\text{TOA}}\, \exp\left(-4\ln 2\, \frac{\delta_j^2}{\Delta_C^2}\right)\,. \tag{5.27}$$

Figure 5.2 shows that the approximate solution in Equation 5.27 (*Approx. 2*) fits better the numerically integrated solution than the analytical approximation in Equation 5.25 (*Approx. 1*). Estimates of the convolution width Δ_C can be obtained by direct measurement of the Full Width at Half Maximum (FWHM) of the numerically derived function. However, as seen in Figure 5.3, for beamwidths

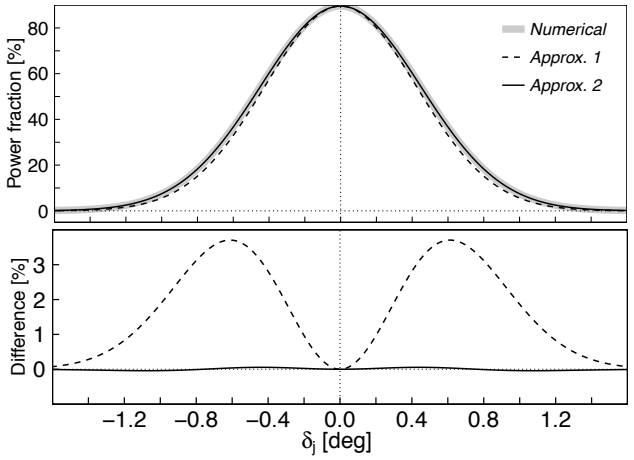

Figure 5.2: (Top) Fraction of detected solar power for a single echo-sample as a function of angular distance between the antenna axis and the Sun-disk centre, calculated from the convolution integral between the radar antenna sensitivity pattern and the solar-disk pattern, for an antenna beamwidth of 1°. The convolution has been computed numerically (*Numerical*; thick grey line) and using two analytical approximations, Equation 5.25 (*Approx. 1*; dashed black line) and Equation 5.27 with an effective width of 1.057° (*Approx. 2*; solid black line). (Bottom) Difference between the fraction of detected solar power calculated numerically and using *Approx. 1* and *Approx. 2*.

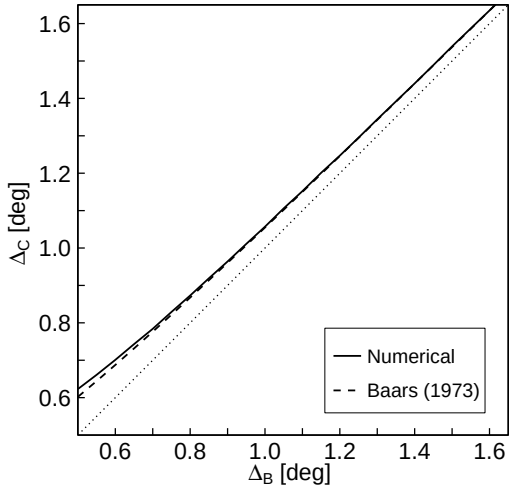

Figure 5.3: Antenna-Sun convolution width Δ_C as a function of the antenna beamwidth Δ_B. The Δ_C values are estimated by direct measurement of the half-peak width of the numerically computed convolution function (solid line) and from the formula given in Baars (1973) (dashed line).

approximately larger than 0.7°, the analytical formula proposed by Baars (1973) can be used instead of the numerical computation, with an accuracy better than 1 %:

$$\Delta_C = \sqrt{\Delta_B^2 + \left(\frac{\ln 2}{2}\right)\Delta_S^2}\,. \tag{5.28}$$

From Figure 5.3, note that the convolution width Δ_C approaches the antenna beamwidth Δ_B as the antenna beamwidth increases, indicating that the approximation in Equation 5.25 is valid for $\Delta_B >> \Delta_S$, as expected from the implications of assuming $\cos\xi \approx 0$.

5.2.2 Detected solar power in a scanning ray

The detected power expression in Equation 5.27 corresponds to the solar power measured in a single radar sample (p_{det}^j). However, the power detected in a complete ray scan (p_{det}) is calculated by the radar processor as the (weighted) average of the power values measured in the collection of consecutive samples performed while the antenna is in motion across the radial ray:

$$p_{\mathrm{det}} = \frac{1}{N}\sum_{j=1}^{N} p_{\mathrm{det}}^j(\delta_j)\,, \tag{5.29}$$

where equally weighted sample integration, i.e. finite time block integration (Zrnič and Doviak, 1976), is assumed.

As sketched in Figure 5.1, the relative distance between the Sun-disk centre and the antenna axis (δ_j) may be expressed as a function of the antenna coordinates (ϕ_j^0, θ^0). In a scanning setup, the instantaneous azimuthal position of the antenna ϕ_j^0 may be expressed as the sum of a fixed coordinate (the central position of the axis within the whole scanned ray; ϕ^0) and a variable coordinate χ_j that reproduces, for each instantaneous sample, the displacement of the axis with respect to the fixed coordinate, as sketched in Figure 5.4:

$$\delta_j^2 = \phi_j^{0\,2} + \theta^{0\,2} = (\phi^0 + \chi_j)^{\,2} + \theta^{0\,2}\,. \tag{5.30}$$

When the total number of samples taken during a ray scan (N) is large, or the azimuthal displacement of the antenna between samples is small compared to the total width of the ray (Δ_R), the variable χ_j in Equation 5.30 may be assumed continuous and the pulse average in Equation 5.29 can be approximated by an

integral (Zrnič and Doviak, 1976; Doviak and Zrnič, 1984):

$$p_{\text{det}} \approx \frac{1}{\Delta_R} \int_{-\frac{\Delta_R}{2}}^{\frac{\Delta_R}{2}} p^j_{\text{det}}(\chi)\, d\chi\,, \quad \text{if}\, \Delta_R >> \frac{\Omega_{\text{scan}}}{\text{PRF}}\,. \tag{5.31}$$

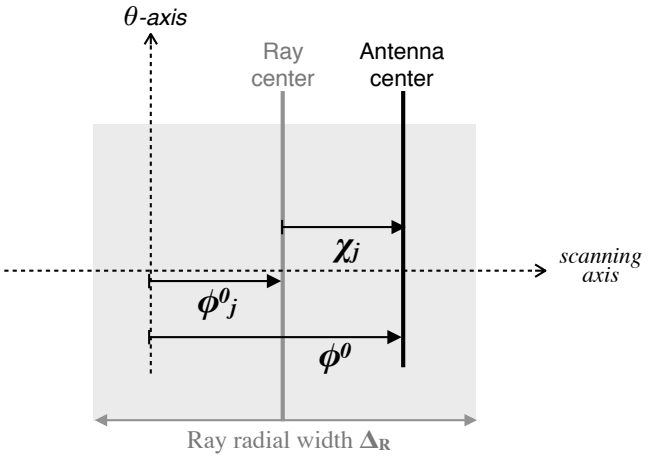

Figure 5.4: Graphical relation between fixed and moving coordinates in an azimuthally scanning setup.

The general solution of Equation 5.31 with Equation 5.27 and Equation 5.30 is given in terms of the *Error Function*:

$$p_{\text{det}} = l_{\text{gas}}\, l_0\, \frac{p_{\text{TOA}}}{4}\, \frac{\Delta_C}{\Delta_R} \sqrt{\frac{\pi}{\ln 2}}\, \exp\left(-4 \ln 2\, \frac{\theta^{02}}{\Delta_C^2}\right)\, F\left(\phi_0; \Delta_R, \Delta_C\right)\,, \tag{5.32}$$

with:

$$F\left(\phi_0; \Delta_C, \Delta_R\right) = \left\{ \text{erf}\left[\frac{\sqrt{4\ln 2}}{\Delta_C}\left(\phi^0 + \frac{\Delta_R}{2}\right)\right] - \text{erf}\left[\frac{\sqrt{4\ln 2}}{\Delta_C}\left(\phi^0 - \frac{\Delta_R}{2}\right)\right]\right\}\,. \tag{5.33}$$

The function $F(\phi_0; \Delta_C, \Delta_R)$ has a well defined maximum value given by:

$$F(\phi_0; \Delta_C, \Delta_R)_{\text{max}} = 2\,\text{erf}\left(\sqrt{\ln 2}\frac{\Delta_R}{\Delta_C}\right)\,. \tag{5.34}$$

The overall shape of the non-elemental function $F(\phi_0; \Delta_C, \Delta_R)$ is controlled by the Δ_R/Δ_C ratio and, as exemplified in Figure 5.5, closely resembles a Gaussian for

values $\Delta_R/\Delta_C < 1.5$ (Blahak, 2008). The FWHM of the Gaussian, i.e. the scanning convolution width ($\Delta_{C,\mathrm{scan}}$), can be estimated from the solution of the following transcendental equation, in analogy to Section 7.8 in Doviak and Zrnič (1984):

$$\left[F\left(\phi_0;\Delta_R,\Delta_C\right) - \frac{2}{e}\,\mathrm{erf}\left(\sqrt{\ln 2}\,\frac{\Delta_R}{\Delta_C}\right)\right]_{\phi_0=\pm\phi_0^\star} = 0\,, \tag{5.35}$$

being $\phi_0^\star$ the positive root of Equation 5.35 and $\Delta_{C,\mathrm{scan}} = 2\sqrt{\ln 2}\,\phi_0^\star$.

Under these conditions, the detected solar power is expressed as:

$$p_{\mathrm{det}} = l_{\mathrm{gas}}\, l_{\mathrm{scan}}\, p_{\mathrm{TOA}}\, \exp\left[-4\ln 2\left(\frac{\theta_0^2}{\Delta_C^2} + \frac{\phi_0^2}{\Delta_{C,\mathrm{scan}}^2}\right)\right]\,, \tag{5.36}$$

with:

$$l_{\mathrm{scan}} = l_0\sqrt{\frac{\pi}{4\ln 2}}\,\frac{\Delta_C}{\Delta_R}\,\mathrm{erf}\left(\sqrt{\ln 2}\,\frac{\Delta_R}{\Delta_C}\right)\,. \tag{5.37}$$

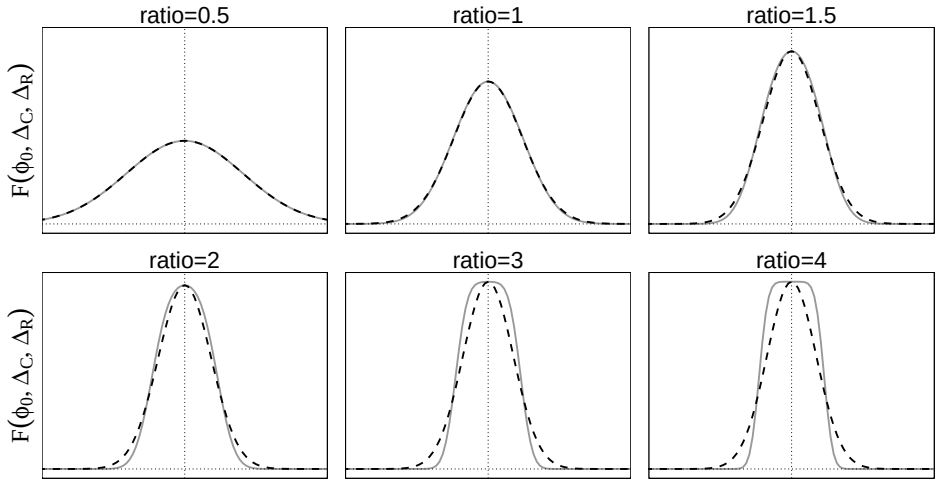

Figure 5.5: Numerically calculated $F\left(\phi_0,\Delta_R,\Delta_C\right)$ (solid grey line) compared to a Gaussian function with an equivalent value of the FWHM (dashed black line), for different values of the $\frac{\Delta_R}{\Delta_C}$ ratio and using a fixed value for the radial resolution Δ_R =1°.

As indicated in Equation 5.2, the available relative position coordinates (x, y) are given with respect to the Radar's reference system. The transformation between (ϕ_0, θ_0) and (x, y) sets of coordinates would require spherical geometry calculations. Nevertheless, for elevations below 50° and for (ϕ, θ) varying within ±5°, the relationship $\phi_0 = \cos(el_R)\,x$ can be used with an accuracy better than 1 %, according

to Blahak (2008). In addition, the effective width is assumed independent of elevation ($\Delta_{C,\mathrm{scan}}/\cos(el_R) \approx \Delta_{C,\mathrm{scan}}$), with an accuracy error below 1 % for $\mathrm{el}_R \leq 8°$. Accounting for the possibility of a systematic bias in antenna pointing (x_0, y_0), all these considerations lead to the model equation solution:

$$p_{\mathrm{det}} = l_{\mathrm{gas}}\, l_{\mathrm{scan}}\, p_{\mathrm{TOA}}\, \exp\left\{-4\ln 2\left[\frac{(x-x_0)^2}{\Delta_x^2} + \frac{(y-y_0)^2}{\Delta_y^2}\right]\right\}, \tag{5.38}$$

where, for an azimuthally scanning antenna, the solar image width in elevation is given by the convolution width and the solar image width in azimuth is given by the scanning convolution width:

$$\begin{aligned} \Delta_x &\equiv \Delta_{C,\mathrm{scan}} \\ \Delta_y &\equiv \Delta_C\,. \end{aligned} \tag{5.39}$$

Table 5.1 gives the values of the solar image widths for various antenna beamwidths, estimated applying the procedures and formulae presented in the current section and assuming that the width of the radial rays is 1°.

Table 5.1: Antenna-Sun convolution widths as a function of the antenna beamwidth Δ_B. The Δ_y values have been estimated by direct measurement of the half-peak width of the numerically integrated convolution function and the Δx values are computed from the numerical resolution of the transcendental equation in Equation 5.35, using a fixed ray width of Δ_R =1°. The accuracy of the estimates is within ±0.001° from the resolution of the numerical computations.

Δ_B [°]	Δ_y [°]	Δ_x [°]	Δ_B [°]	Δ_y [°]	Δ_x [°]
0.700	0.784	1.093	1.200	1.247	1.439
0.800	0.873	1.150	1.250	1.295	1.479
0.900	0.964	1.215	1.300	1.344	1.521
1.000	1.057	1.285	1.350	1.392	1.563
1.050	1.106	1.323	1.400	1.440	1.605
1.100	1.152	1.360	1.450	1.489	1.648
1.150	1.201	1.400	1.500	1.539	1.693

5.3 Outlier removal

In the Sun-monitoring method, the calibration parameters are estimated from the LLS fit of Equation 5.1. However, least squares estimates are highly sensitive to model outliers, i.e. observations that do not appropriately follow the pattern of the theoretical model to be fitted. In the case of the solar interference model inversion, such problematic observations may be present due to precipitation or ground echoes affecting the majority of the radial range bins considered or due to attenuation by precipitation, yielding an inaccurate estimation of the power of the interference. Also, continuous interferences of non-solar origin, being close enough to the solar position, may go all through the identification process. In a less likely situation, model outliers may be present if interference corresponds to a transient state of strong solar activity.

The choice of the median as an estimator of the power of the solar interference is decisive in minimising the effect of range bins with a power value deviating from the along-range constant value expected. However, the median has a breakpoint of 50 % and constitutes a robust estimator as long as more than half of the range bins are unaffected by ground clutter or precipitation. At this regard, the constancy criterium based on robust statistical estimators introduced in the solar interference detection and characterisation algorithm allows to discard observations strongly biased by ground clutter or precipitation (see Chapter 4, Subsection 4.1.2).

A common procedure to discard outliers is to do the fitting of data to the model twice. After the first fit, observations lying too far from the fitted curve are removed and a second and fit it is performed for the remaining observations (Holleman et al., 2010b). However this procedure may fail when *leverage* outliers are present; i.e. observations found at (x, y) positions far from the mean $(\overline{x}, \overline{y})$ defined by the bulk of observations. These observations have a large weight in the minimisation of the cost function by the LLS regression and a single leverage point can distort the initial fit.

Here, a non-iterative method for the removal of biased observations prior to inversion is proposed. The criterion is based on the assumption that, when the pointing bias is approximately below 0.1°, the detected powers of the solar interference observations, corrected for the distance to the Sun and for the atmospheric and scanning losses, P_{corr}, should display a normal distribution with $\hat{P}_{\mathrm{TOA}}$ as its expected value. The P_{corr} for each of the solar interferences is estimated from their detected power P_{det} by reverse application of Equation 5.1 with $(x_0, y_0) = 0$:

$$P_{\text{corr}} = P_{\text{det}} - L_{\text{gas}} - L_{\text{scan}} - \hat{L}\,, \tag{5.40}$$

where:

$$\hat{L} = a_x\, x^2 + a_y\, y^2 = -40 \log_{10} 2 \cdot \left(\frac{x^2}{\Delta_x^2} + \frac{y^2}{\Delta_y^2} \right)\,. \tag{5.41}$$

Note that for computation of the corrected power through Equation 5.40 and Equation 5.41 estimates of the solar image widths are needed, which can be derived from the antenna beamwidth and the radial resolution, as described in Section 5.2, or can be extracted from Table 5.1 if the ray resolution is the typical 1°.

The median $\overline{P_{\text{corr}}}$ and its corresponding $\sigma_{P\text{corr}}$ estimator (derived from the MAD) are computed for the target solar interference collection. Solar observations whose estimated P_{corr} is not within the 2-$\sigma_{P\text{corr}}$ interval around $\overline{P_{\text{corr}}}$, are considered outliers and rejected. The value of 2 is the standard score or "z-score" corresponding to a confidence interval of approximately 98 % for the normal distribution. The width of the limiting σ-interval, i.e. the value of the threshold standard score, may be adjusted to match the desired level of strength in the outlier removal.

When a significative antenna pointing bias is present, the P_{corr} calculated for each interference is no longer a realisation of $\hat{P}_{\text{TOA}}$ but is instead a realisation of the more general quantity:

$$P_{\text{corr}} = \hat{P}_{\text{TOA}} + \frac{40 \log_{10} 2}{\Delta_x^2} \left(2x_0\, x - x_0^2\right) + \frac{40 \log_{10} 2}{\Delta_y^2} \left(2y_0\, y - y_0^2\right)\,. \tag{5.42}$$

Consequently, the basic assumption of a normal statistical distribution of the P_{corr} is no longer reliable and its shape depends on the particular (x, y) distribution of the dataset as well as on the magnitude of the pointing biases (x_0, y_0).

Figure 5.6 shows P_{det} and their corresponding P_{corr} values for a simulated set of observations in 1-dimension and for three different pointing offsets. As observed, the filtering window gets wider as the pointing offset increases. When the pointing offset is small, the outlier identification procedure removes sporadical observations whose P_{corr} lies out of the filtering window, usually observations with a low signal compared to their standard deviation. When the pointing offset is larger, the outlier removal procedure keeps these observations but thanks to the use of robust estimators the procedure is still effective in the removal of leverage outliers.

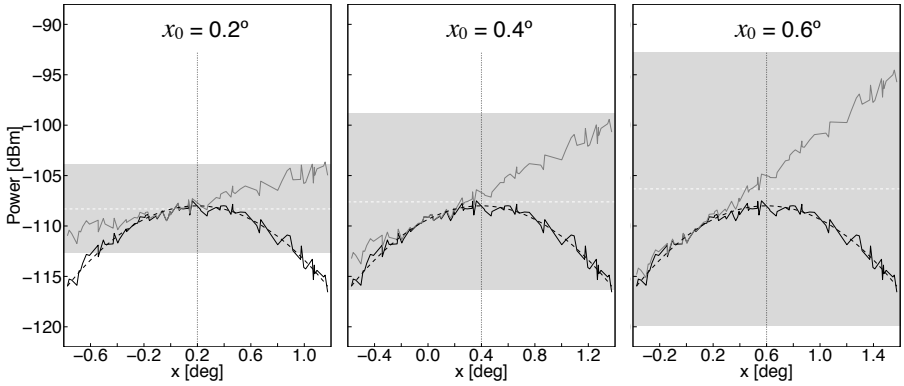

Figure 5.6: Simulated solar observations in 1-dimension for Δ_x =1.2° and for three different values of the pointing bias x_0: (left panel) 0.2°, (centre panel) 0.4° and (right panel) 0.6°. The dashed black curve depicts the nominal power from the theoretical model. The black solid line indicates the power of random observations with ±0.5 dB standard deviation error. The grey solid line gives the P_{corr} calculated for these observations and the grey shaded area limits the filtering window in the outlier removal procedure.

5.4 Application to XRAD

In the present section, results of application of the Sun-monitoring method for the three operative XRAD radars during selected study periods of year 2013 are presented and briefly analysed. The goodness of the inversion for both the 5P and the 3P models (Subsection 5.1.3) is studied. The goodness of fit is quantified through the Root Mean Squared Deviation (RMSD); that is, the square root of the unbiased estimator for the variance of the fit residuals:

$$\text{RMSD} = \sqrt{\frac{1}{(N_{\text{intf}} - p - 1)} \sum_{i=0}^{N_{\text{int}}} \left(P_i - P_i^{\text{fit}}\right)^2}. \tag{5.43}$$

The scale factor for the unbiased estimator is $(N_{\text{int}} - p - 1)$, with N_{int} the number of observations and p the number of model parameters. In the optimal case, the RMSD should be of the order of the random error of the data set. The lower limit for the RMSD is estimated in 0.3 dB, as an approximation for the standard error of the median power $\overline{P_{\text{det}}}$, calculated from the maximum 2 dB standard deviation threshold applied in the solar interference identification process (Chapter 4, Subsection 4.1.2). As a means for assessing the comparison between inversion approaches, the adjusted R-squared value of the fit, R^2_{adj}, is used. The adjusted R-squared value

is the relative decrease of the unbiased variance of the residuals with respect to the total unbiased variance of the dataset:

$$R^2_{\text{adj}} = 1 - \left(\frac{RMSD}{\sigma}\right)^2 , \tag{5.44}$$

with:

$$\sigma = \sqrt{\frac{1}{(N_{\text{intf}} - 1)} \sum_{i=0}^{N_{\text{int}}} \left(P_i - \bar{P}\right)^2} , \tag{5.45}$$

where $\bar{P}$ is the mean value of the P_i detected powers of the observations. Consequently, R^2_{adj} quantifies the improved predictive power of the fitted model with respect to a model that is the mean of the observations.

In the case of the XRAD radars, the identification algorithm presented in Chapter 4 is not able to detect solar interferences for antenna elevations above 8°, because radar data above 10 km are not recorded by the processor. Also the condition expressed in Equation 5.31 is fulfilled for the XRAD radars, since the 1° radial resolution is significantly higher than the maximum angular sampling interval of 0.032° (for the nominal Ω_{scan} =24 °s^{-1} and the minimum PRF of 750 Hz in the short range volumetric scans). Hence, the assumptions undertaken in the derivation of the theoretical model hold valid.

Table 5.2 summarises the results of application of the Sun-monitoring method to each of the XRAD radars studied. Apart from the retrieved calibration parameters, the table also gives the average SNR of the solar signal with respect to the sensitivity of each radar, the average number of daily observations collected and the average RMSD as indicator of the goodness of the model inversion. The effective solar image widths given as fixed parameters in the 3P model fit, which are also used to calculate the scanning losses L_{scan}, have been estimated based on *ad hoc* antenna pattern measurements, as explained in the following section.

5.4.1 Solar image widths

Accurate estimations of antenna beamwidths in azimuth and elevation are required for an improved application of the Sun-monitoring method. Indeed, beamwidth estimates are needed for calculation of the scanning losses and of the solar image widths. The latter are, in turn, essential for the estimation of the solar power at the TOA and for application of the outlier removal method and of the 3P model inversion.

Table 5.2: Statistics of Sun-monitoring method results for XRAD radars during selected study periods: CDV - from 01 May 2013 to 30 September 2013, LMI - from 20 September 2013 to 09 December 2013 and PDA - from 01 April 2013 to 19 June 2013. Median and MAD values are given for: the maximum signal-to-noise ratio (SNR), estimated as the ratio between the maximum peak solar power (from the DRAO reference) and the minimum detectable power P_{mds}; daily number of detected solar interferences ($\mathrm{N_{intf}}$); antenna pointing biases in azimuth (x_0) and elevation (y_0); peak solar power difference between the estimate and the reference from DRAO (ΔP_{TOA}) and solar image widths in azimuth (Δ_x) and elevation (Δ_y).

Radar	SNR [dB]	N_{int}	Model	x_0 [°]	y_0 [°]	Δ_x [°]	Δ_{y} [°]	ΔP_{TOA} [dB]	RMSD [dB]
CDV	7.0 ± 0.8	20 ± 9	3P	-0.06 ± 0.04	-0.13 ± 0.06	1.44	1.15	-0.55 ± 0.90	0.58 ± 0.17
			5P	-0.07 ± 0.04	-0.13 ± 0.07	1.46 ± 0.25	1.42 ± 0.27	-0.66 ± 1.07	0.54 ± 0.13
LMI	5.0 ± 0.6	16 ± 9	3P	-0.21 ± 0.06	-0.14 ± 0.04	1.29	1.15	-0.29 ± 0.33	0.38 ± 0.12
			5P	-0.22 ± 0.06	-0.14 ± 0.04	1.28 ± 0.28	1.21 ± 0.16	-0.39 ± 0.31	0.37 ± 0.10
PDA	8.7 ± 0.7	47 ± 12	3P	-0.05 ± 0.03	0.06 ± 0.03	1.36	1.20	-1.45 ± 0.18	0.61 ± 0.15
			5P	-0.05 ± 0.01	0.05 ± 0.03	1.32 ± 0.06	1.20 ± 0.09	-1.38 ± 0.24	0.57 ± 0.13

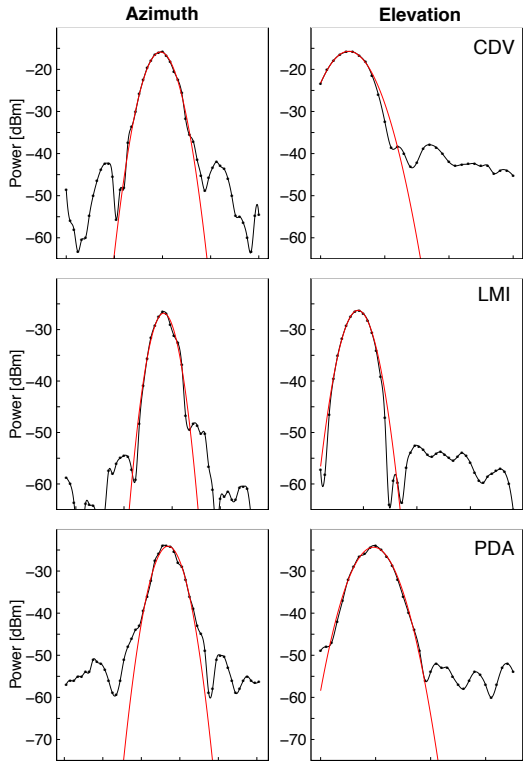

Figure 5.7: Antenna pattern measurements carried out in December 2012 for XRAD radars (black dots) using selected fixed ground targets. The black solid line depicts the spline interpolation of actual measurements to a resolution of 0.01°. The red curve displays the second order polynomial fit to points close to the maximum, used to estimate the antenna main lobe beamwidths.

Table 5.3: Beamwidth estimates from the antenna pattern measurements in Figure 5.7. The beamwidth values chosen for application of the Sun-monitoring method and their corresponding solar image widths are also given, for a nominal scanned ray resolution $\Delta_R = 1°$.

Radar	$\Delta^{\mathrm{az}}_{B,\mathrm{est}}$ [°]	$\Delta^{\mathrm{el}}_{B,\mathrm{est}}$ [°]	Δ^{az}_{B} [°]	Δ^{el}_{B} [°]	Δ_{x} [°]	Δ_{y} [°]
CDV	1.199 ± 0.03	1.106 ± 0.003	1.20	1.10	1.44	1.15
LMI	0.946 ± 0.006	1.099 ± 0.002	1.00	1.10	1.29	1.15
PDA	1.089 ± 0.008	1.14 ± 0.01	1.10	1.15	1.36	1.20

Nominal antenna beamwidths set in the processor are 1.2° and 1.1° in azimuth and elevation for all XRAD radars. These values are given by the antenna manufacturer and have a precision of 0.05°. Figure 5.7 displays the results of antenna pattern measurements carried on December 2012 for the CDV, the LMI and the PDA radars, during the annual routine maintenance tasks (see Chapter 3, Subsection 3.3.1). The measurements are taken with a resolution of 0.2° and have been afterwards spline-interpolated to 0.01° resolution. A second order polynomial fit has been applied to interpolated data that lied within ±1.5° and with a power not lower than 5 dB from the maximum. The FWHM of this polynomial constitutes the antenna beamwidth estimate. Table 5.3 summarises the estimated beamwidths in azimuth and elevation and the corresponding effective solar image widths for each of the radars. These results indicate that the actual beamwidths differ from the nominal values in the cases of the LMI and the PDA radars. The solar image widths given in Table 5.3 are the ones used in the application of the Sun-monitoring method to the XRAD (see Table 5.2).

5.4.2 Leverage outliers: the PDA radar

The Puig d'Arques (PDA) radar has proven to be prone to present outlying observations, mainly due to contamination by emission from RLAN devices located close to the radar site (see Chapter 4, Subsection 4.2.2). The interferences by these external electronic devices often show constancy and continuity characteristics similar to the solar ones. Daily, several constant and continuous interferences of presumed non-solar nature are detected by PDA. These are easily recognisable because they generally occur at low elevation scans and because their positioning does not follow the solar trajectory. The Sun proximity criterion is very effective in removing them but few non-solar interferences may still remain.

Observations detected far from the Sun with a strong power signal have the potential to cause large disturbances in the LLS fit, constituting leverage outliers. Figure 5.8 gives evidence of the effect of such type of observations on the result of the fit for two particular examples; when leverage outliers are present, the model fit results in non-physical solutions yielding negative solar image widths (left panel) or does not represent the bulk of the observations (right panel). The procedure described in Section 5.3 removes these leverage observations, improving the quality of the fit and the reliability of the model parameter estimates.

Figure 5.9 displays the day-to-day results of the solar interference model inversion, before outlier removal was applied, for the data collected by the PDA radar

during the period from April to August of 2013. The impact of the outliers on the stability of the parameters and on the convergence of the fit is remarkable. The presence of extreme outliers affects the estimates of all calibration parameters. The 3P model reacts with wild fluctuations both in power and in pointing. Part of these fluctuations are reflected in the width estimates of the 5P model. Power and pointing bias estimates in the 5P approach appear more resilient to the effect of outliers because the widths are additionally tuned for the model to fit the data and reduce the cost function or RMSD. This is to be expected given the shape of the model function and the characteristics of the outliers - far located and with high power values. Indeed, in extreme cases the 5P model fit leads to non-physical solutions with negative width and the resulting fit surface is a hyperbolic paraboloid or saddle surface, as seen for the 04 April 2013 example in Figure 5.8. These failed fits appear as gaps in the 5P model time-series plots in Figure 5.9; the inversion yielded non-physical solutions for approximately 24.6 % of the days considered.

Figure 5.10 shows how application of the outlier removal method allows the retrieval of daily stable calibration parameters through both the 5P and the 3P inversions. The median antenna pointing biases estimated for the studied period are small, around $-0.05°$ in azimuth and $0.06°$ in elevation, with standard deviations between $0.01°$ and $0.03°$. P_{TOA} estimates and the DRAO reference data display a good match between their respective trends. The Sun-monitoring method allowed to detect a difference of about $-1.4\,\mathrm{dB}$ between their values, which was corrected in a technical *in-situ* recalibration of the radar receiver on 20 June 2013. The intervention is reflected in the abrupt change of the estimated P_{TOA}, indicating great sensitivity in the monitoring method.

5.4.3 Information content: the LMI and PDA radars

Figure 5.11 summarises the statistics of the LMI and the PDA radar monitoring results for selected periods of 2013 during which the calibration status of both radars is assumed to have stayed invariant. These statistics have served to compare the performance of the 5P and 3P model fits under two situations for which the information contained in the set of daily observations is different.

On a daily basis, PDA detected 40 to 70 solar interferences (see Table 5.2), homogeneously distributed within distances up to $\pm 1°$ and $\pm 0.8°$ from the solar disk centre in azimuth and elevation respectively. The observations found at farther relative distances from the Sun are expected to contain more information for the retrieval of the solar image widths. In fact, as seen in Figure 5.11 the widths

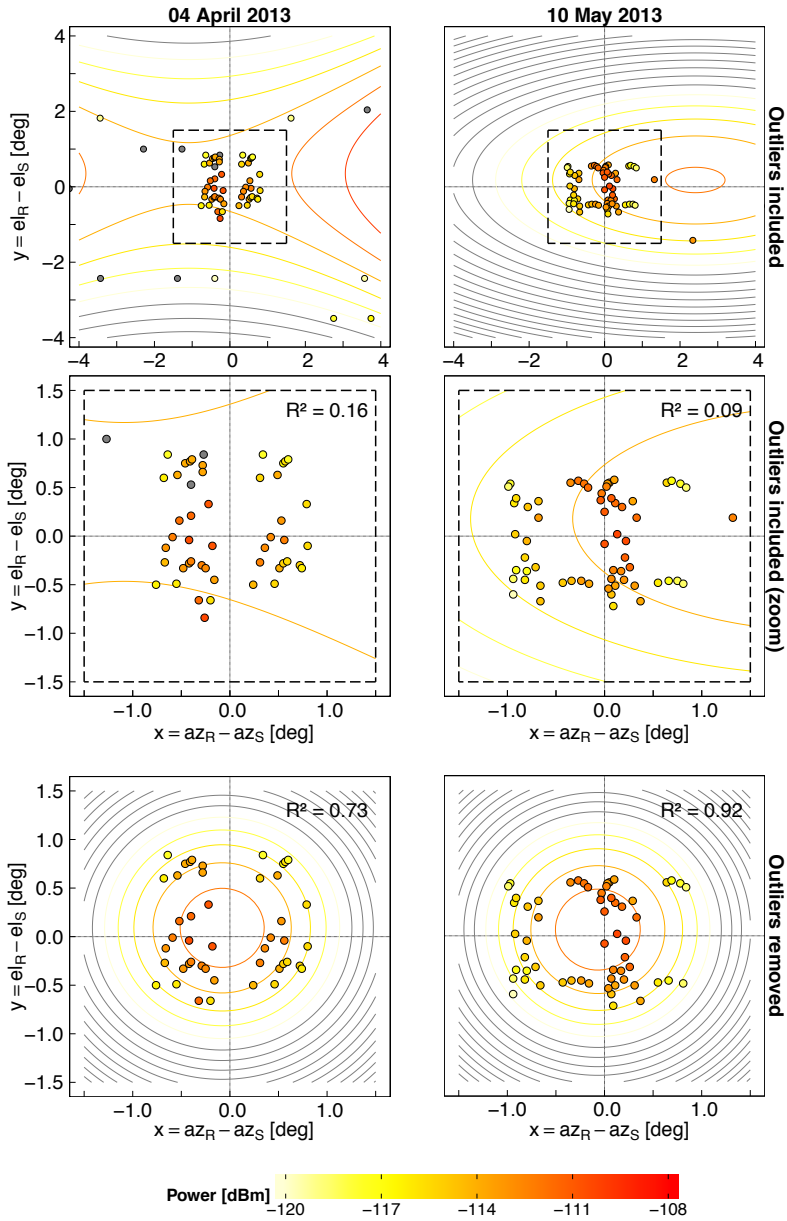

Figure 5.8: Solar interference 5P model fit to observations collected by the PDA radar on 04 April 2013 and 10 May 2013: (top) regular model fit using all identified interferences, (middle) zoom into the framed region in the top panels and (bottom) model fit after outlier removal procedure application. Observations are scattered by the relative position between the interference radial and the Sun in azimuth and elevation, i.e. x and y variables of the model Equation 5.3. The observations and the isolines of the fit model appear colour-coded as a function of the detected power, corrected for gaseous atmospheric attenuation. Adjusted R-squared values of the fit are given in each case. The resolution of the contour levels is 2 dB.

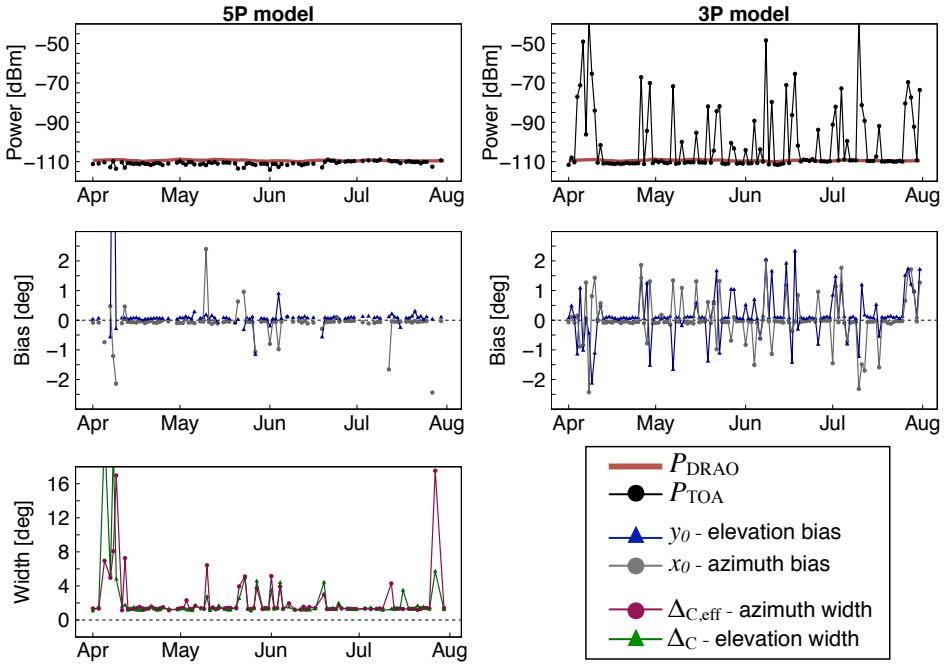

Figure 5.9: Estimated values of the calibration parameters for the PDA radar, retrieved in both the 5P and the 3P model fits when the set of observations includes outliers. The time series corresponds to the period from April to August 2013.

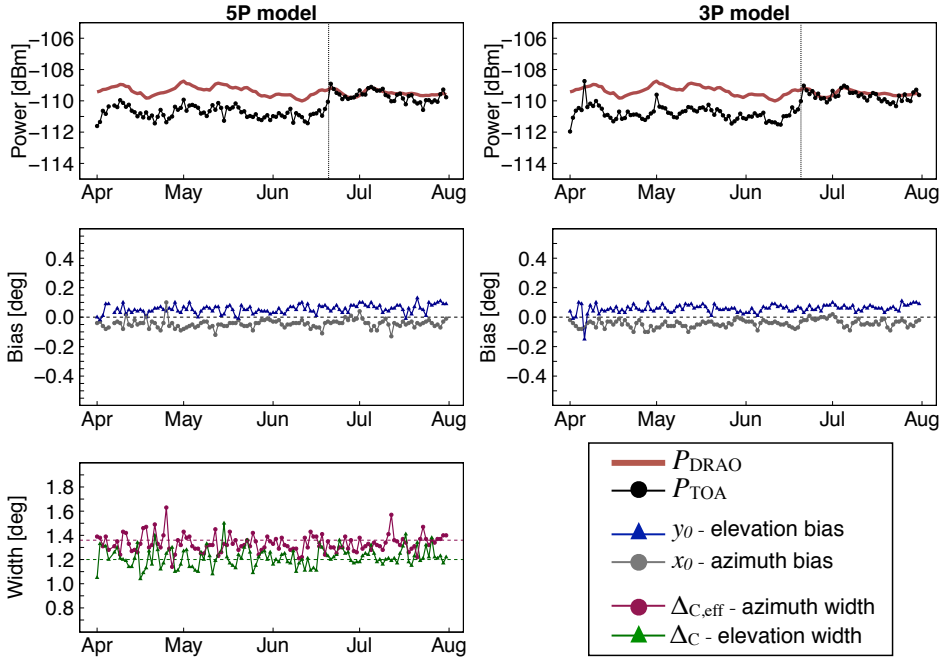

Figure 5.10: As Figure 5.9 but when outlier removal procedure is applied. Dotted vertical lines in the top panels indicate the routine maintenance calibration carried on the 20 June. In the bottom left panel, dashed horizontal lines indicate the fixed width values in azimuth (magenta) and elevation (green) in the 3P model fit.

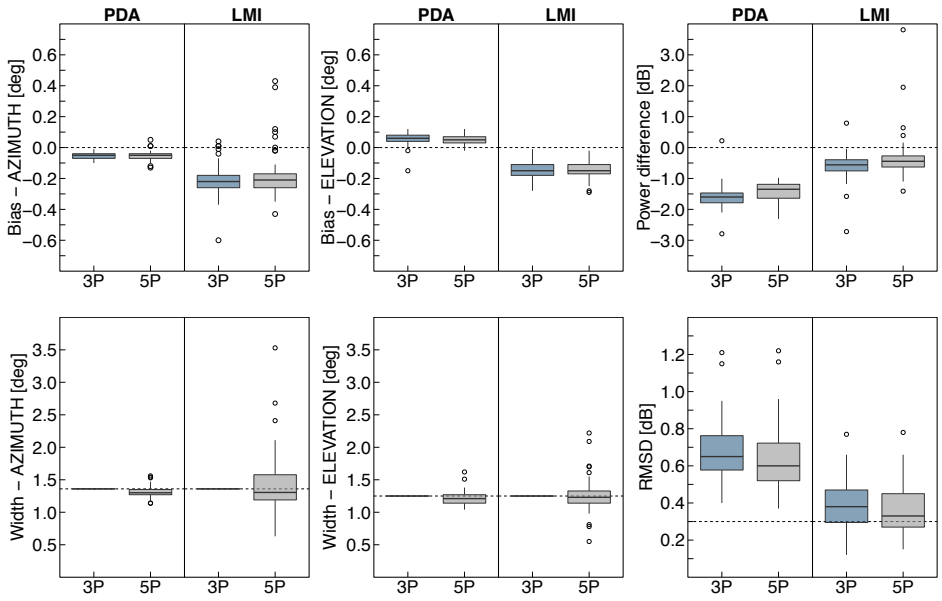

Figure 5.11: Boxplot diagrams of retrieved calibration parameters comparing the 5P and the 3P model fits for the PDA (from 01 April 2013 to 19 June 2013) and the LMI radars (from 20 September 2013 to 09 December 2013). The boxes enclose the Q25-Q75 interquartile range and the black solid line within the boxes highlights the median value. Outliers are displayed as circles outside the 1.5IQ range limited by the whiskers. The fixed solar image width values in the 3P model fit are indicated by horizontal dashed lines.

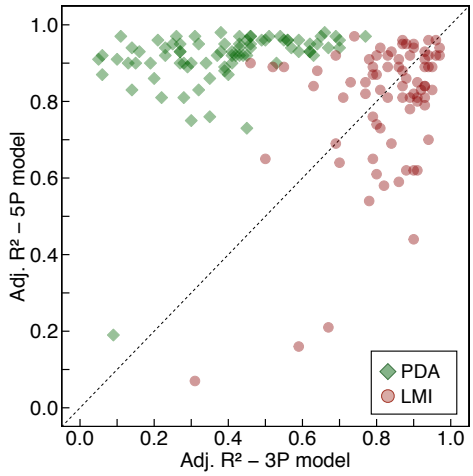

Figure 5.12: Scatter plot of the adjusted R-squared value of fit comparing the 5P and the 3P model fits for the PDA (green diamonds) and the LMI (red circles) radars.

estimated by the 5P model fit display a variability confined within ±0.1°, indicative of a good and stable quality in the data collection by the radar. Moreover, the estimated median widths match appropriately the expected widths derived from antenna pattern measurements in Table 5.3. Note, however, that the fixed azimuthal width in the 3P model inversion is approximately 0.04° larger than the median width estimated in the 5P fit. As a result, the median P_{TOA} estimate by the 3P fit are about 0.1 dB lower than the corresponding median 5P fit estimate. The comparison of the adjusted R-squared values for the two fitting strategies shown in Figure 5.12 indicates that 5P model inversion performs better in explaining the data-sets, yielding stable and close to 1 R-squared values. The 3P model inversion results in unstable and considerably lower R-squared values, which indicate the difficulty of the fixed-width model to reproduce the data variability, likely that of the observations found farther from the Sun.

In the case of the LMI radar, often not enough daily solar interferences are collected for the model inversion, due to a lower sensitivity of the receiving system. The minimum detectable power (P_{mds}) is determined by the response curve of the radar receiver and the magnitude LOG threshold filter, which for the LMI is set at 3 dB above the average noise power (see Chapter 3, Subsection 3.3.2). The combination of these factors result in values of P_{mds} that are only slightly lower than the registered solar powers at the TOA, as expressed by low peak power SNR values for the LMI in Table 5.2.

During the second half of 2013, the LMI collected between 10 and 20 interferences per day, reaching 20 to 30 from October and on, when the solar activity showed a continuous increase. Even under the latter circumstances, the receiving system detected only solar interferences with a high power for which the antenna was closely pointing to the centre of the Sun-disk (not further than ±0.5° distance in azimuth and elevation). The information content in such a distribution of observations is not appropriate for accurate retrievals of the image width by the 5P model, especially in the azimuthal direction. The inverse problem is ill conditioned for the estimation of the widths and the accuracy of the estimates depends on the daily variable setting and precision of the observations available for the fit.

Retrieved azimuthal widths for the LMI radar are unstable with a day-to-day variability of ±0.3°, as confirmed by the deviations shown in Table 5.2. The lack of information also affects the variability of pointing bias estimates in the azimuthal direction both for the 5P and the 3P inversions. The lack of information for the 5P model retrieval is confirmed in the analysis of the adjusted R-squared value of the fit for the LMI shown in Figure 5.12; despite the lower RMSD values from

Figure 5.11, the predictive power of the 5P model is not improved with respect to the 3P model fit, as indicated by the similar R-squared values.

Keeping in mind that LMI detects the solar signal only when the antenna is pointing close to the Sun-disk centre, the fact that the RMSD values for the LMI are significantly lower than for the PDA and close to the lower limit of 0.3 dB suggests that the uncertainty of the solar observations increases with increasing antenna-Sun distance. This is, in fact, sustained by the results shown in Figure 5.13, which illustrates how the detected power of the weaker signals displays a higher uncertainty than that of the stronger solar signals.

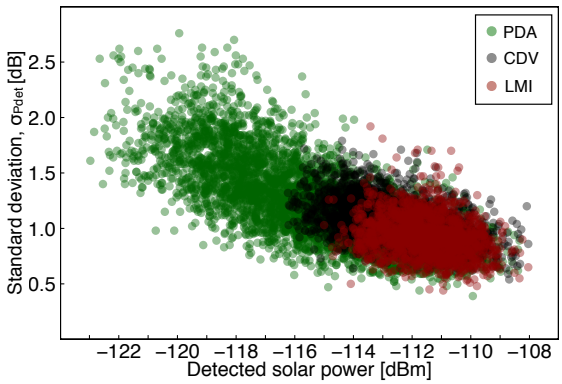

Figure 5.13: Standard deviation of the detected solar power as a function of the detected power for actual solar observations collected, during year 2013, by the CDV, the LMI and the PDA radars. The detected power is given as the median for the range bins along the interference radial and the standard deviation is calculated from the corresponding MAD. Only interferences collected in clear air days, under standard atmospheric propagation conditions and for antenna elevations above 3° are displayed.

The antenna pointing bias estimates for the LMI correspond median errors around −0.22° in azimuth and around −0.15° in elevation for the period studied. These exact pointing biases were verified in a later *in-situ* laser tracker antenna alignment test and attributed to a malfunction of the azimuth resolver, which is the analog component measuring the antenna position (see Subsection 6.3.1 in the upcoming Chapter 6).

5.4.4 Radar system performance: the CDV radar

Figure 5.14 shows the elevation antenna pointing bias and width results for the CDV radar from May to October 2013. During the studied period, the radar system went through four different configuration stages which could be identified from the results

of application of the monitoring method. Relevant dates delimiting the stages are indicated by dashed vertical lines.

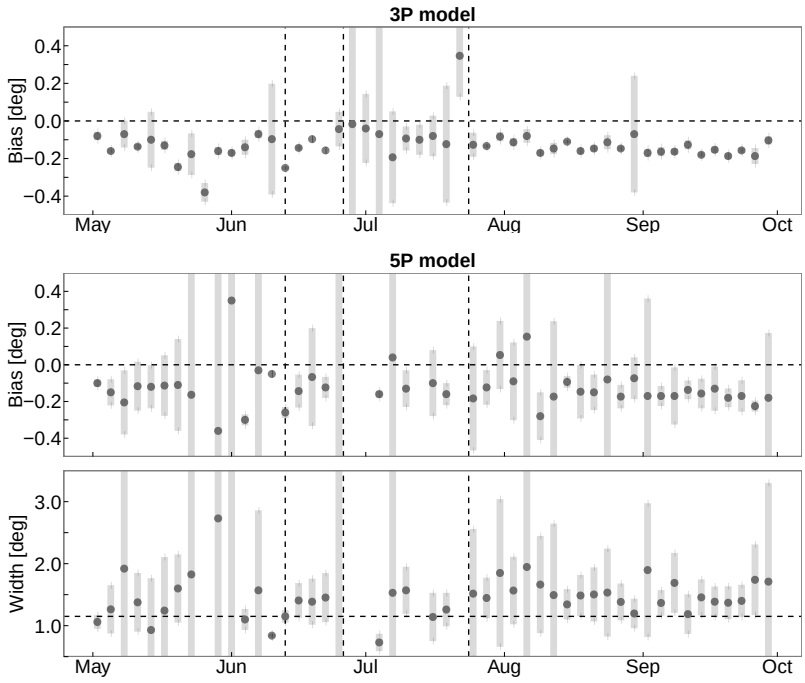

Figure 5.14: 3-day mean values of the pointing bias and width estimates in elevation for the CDV radar. Grey bars indicate the standard error of the mean, calculated from the uncertainties of the estimates. Dashed vertical lines delimit four different radar system configuration stages during the period.

The first stage covers the period prior to a software upgrade on the 13 of June. During this stage the CDV detected few interferences, generally less than 20 per day, often falling below 10, and with a large day-to-day variability. Moreover, the distribution of the relative positions of the interferences was not uniform as expected. In particular, no interferences were detected for a stripe spanning 0.2° in azimuth, causing a remarkable data void region. This fact is well illustrated in Figure 5.15, showing the data distribution before and after the software upgrade. The severe lack of information for the retrieval lead to very variable elevation bias and width estimates with large uncertainties. The anomaly in the data distribution was solved in the software upgrade, suggesting a problem in the processing module.

On the 26 of June, oscillations in the transmitter amplification operation were detected and this situation persisted until the 24 of July, when TWT amplifier was

replaced. Throughout this period, the unstable operation of the TWT may have affected the noise figure and hence the sensitivity of the system. The daily number of detected interferences was continuously below 10 and the quality of the solar power observations, these being close to the noise level, was deteriorated. When the number of observations allowed the solar interference model inversion, all parameter estimates were variable with large uncertainties and the 5P fit often returned non-physical solutions. After the TWT change, the number of solar interferences increased above 20 and the improvement in the day-to-day stability of the model parameter results was significative. The variability of the estimates evidenced after the 24 of July has been attributed to the system sensitivity since no interferences were detected at relative distances beyond ca. ±0.7° in azimuth and ±0.5° in elevation.

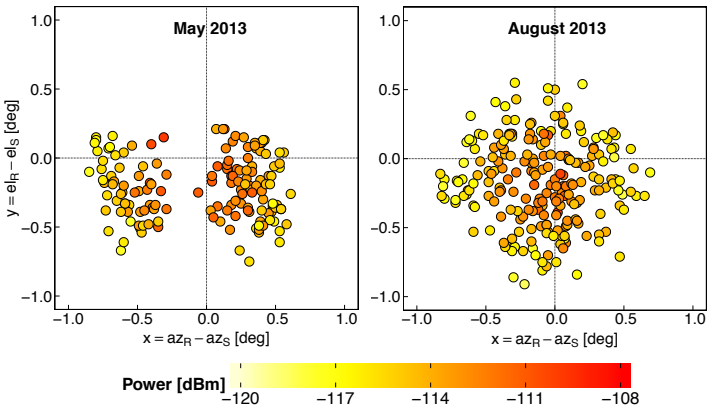

Figure 5.15: Relative positions of solar interferences collected by the CDV radar during: (left) May 2013, before a software upgrade and (right) August 2013, after completing the upgrade.

5.5 Method performance study

The results of the Sun-monitoring technique presented in the previous section indicate that the performance of the method is conditioned by the number of observations collected and by their spatial distribution and spread. These factors are, in turn, linked to the sensitivity of the radar system. For instance, a sudden decrease in the number of solar interferences collected could warn of a sensitivity loss or of a system malfunction.

It has been pointed out that solar observations collected by the PDA and the LMI radars conform two distinct distributions as a function of the relative position between the interference radial and the Sun. These distributions are plotted in Figure 5.16 and their assigned names make reference to the shape displayed. The *elliptical* distribution collects observations by the PDA radar from January to April 2013 and is expected to be optimal for the retrieval of the target calibration parameters, since the dataset spans ranges in azimuth and elevation of the order of the widths to be retrieved. The *circular* distribution corresponds to observations collected by the LMI radar from July to November 2013 and its shape and point density relates to a low sensitivity of the receiving system that only allows the detection of solar signatures for antenna positions close to the Sun.

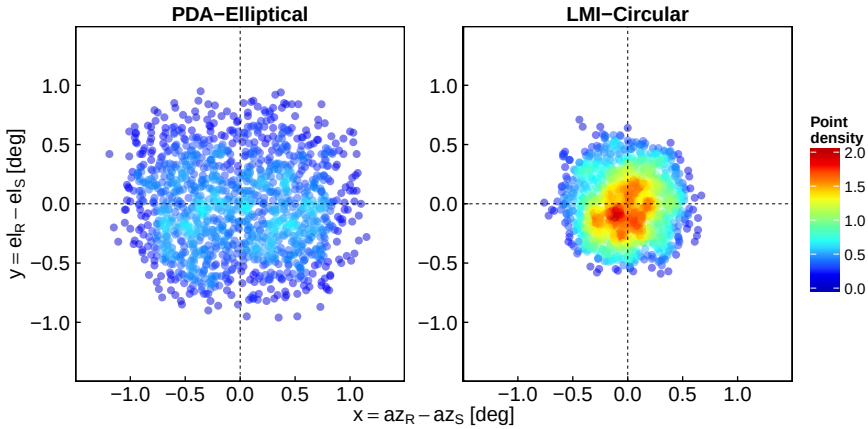

Figure 5.16: Relative antenna-Sun positions of actual solar observations collected by the PDA and the LMI radars in PPI scans. The observations are colour-coded as a function of the spatial point-density.

In the present section, the Sun-monitoring methodology is reproduced under controlled conditions based on the distributions of solar observations collected by the PDA and the LMI radars. The accuracy of the estimated calibration parameters is evaluated for both the 5P and 3P model inversions and for the two different data distributions, as a function of the number of observations available for the inversion and of the error of the observations.

5.5.1 Number and distribution of the solar observations

Figure 5.17 sketches the basic procedure followed in the Sun-monitoring method performance analysis, which serves to study how the number of observations available for the model inversion influences the accuracy of the estimated calibration parameters.

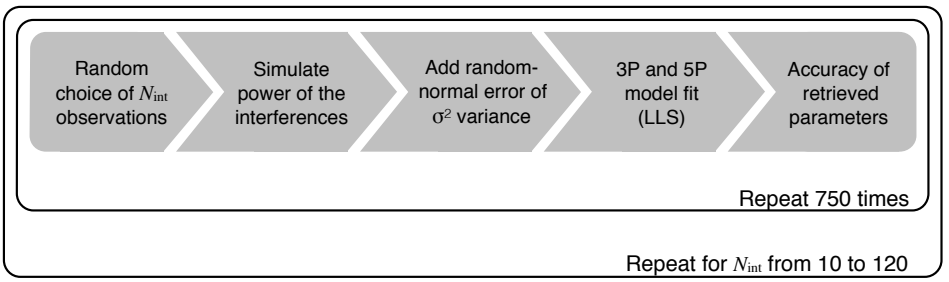

Figure 5.17: Design of the performance study for the Sun-monitoring method.

The performance analysis starts by randomly selecting a certain number of observations (N_{int}) from the target distribution, either one of the distributions displayed in Figure 5.16. For each of these N_{int} observations, the detected solar power is modelled through Equation 5.1. In the simulation of the power of the interferences, inaccuracies associated to the estimation of gaseous attenuation are not considered so $l_{\text{gas}} = 1$. Model parameters are set as (x_0, y_0) =0° and p_{TOA} =1.58×10^{-11} W, the latter corresponding to a P_{TOA} =−108 dBm. It is assumed that the radar is well calibrated in reception so that ΔP_{TOA} =0 dB. These choices are arbitrary, since it is expected that the method performance is independent of the antenna pointing and receiver calibration accuracy. The effective solar image widths are set as Δx =1.36° and Δy =1.15°, simulating a symmetric antenna pattern of Δ_B =1.1° beamwidth and a radial ray width Δ_R =1°. In accordance with these values, the scanning loss factor results in $l_{\text{scan}} = 0.791$.

The power of the simulated interferences is converted to dBm units and random noise of 0.5 dB standard deviation is added. The value for the noise standard deviation is approximately chosen based on the RMSD fit values found for the XRAD radars in the application of the Sun-monitoring method to actual observations (Table 5.2). Finally, both the 3P and 5P models are fitted to the set of observations and the retrieved calibration parameters are compared with the *true* values used in the simulation. The 3P fit is performed with the fixed solar image widths matching the *true* widths assumed in the simulation, i.e. Δx =1.36° and Δy =1.15°.

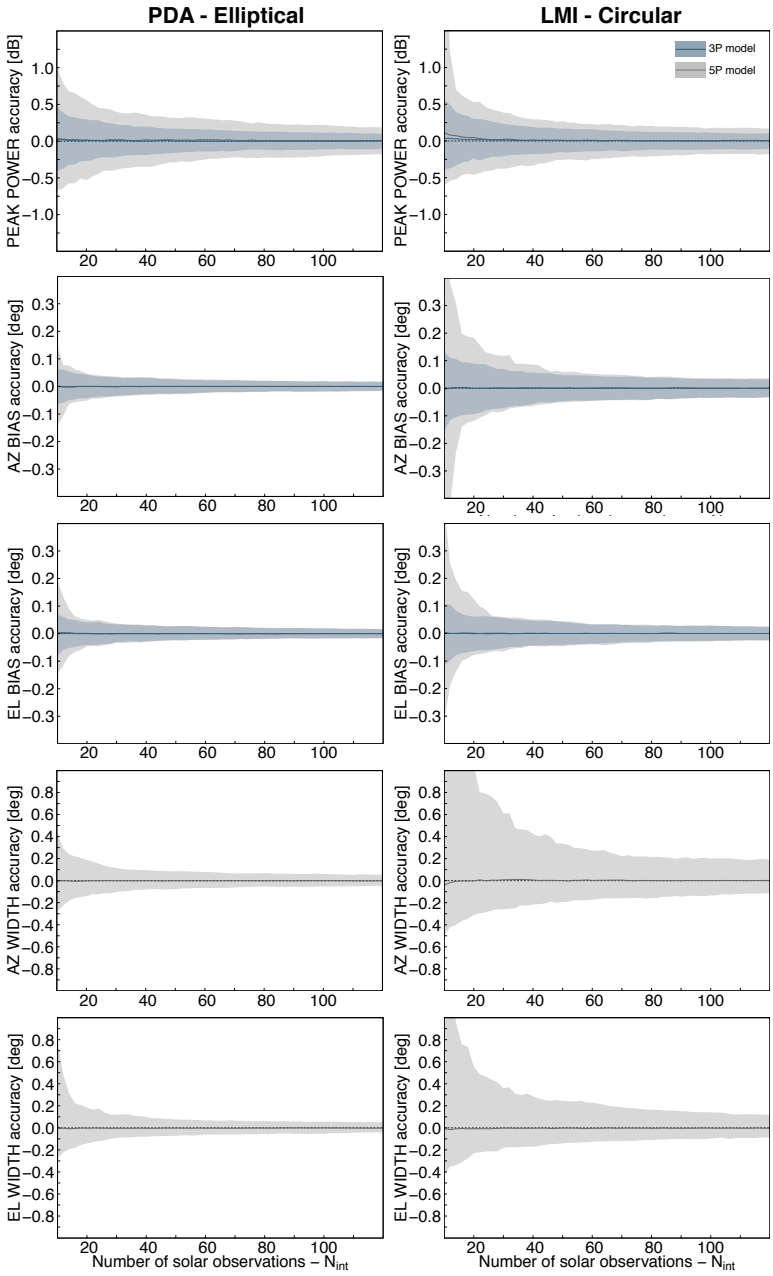

Figure 5.18: Accuracy of retrieved model parameters as a function of the number of observations available for the fit and for two different data distributions: (left) *elliptical* and (right) *circular*. The results correspond to simulations of solar observations with an added noise level of 0.5 dB. The solid lines depict the median accuracy of 750 iterations for the two inversion approaches: (blue) 3P model inversion and (grey) 5P model inversion. Corresponding shadowed areas enclose the Q1-Q99 inter-quantile range.

With the aim of deriving significant statistics, this whole procedure is repeated 750 times, each with a different seed for the random noise generator. The number of observations is varied from 10 to 120 and the whole procedure is carried on for both the *elliptical* and *circular* distributions.

Figure 5.18 shows the resulting statistics of method accuracy, derived from the comparison between the retrieved calibration parameters and their *true* values, as a function of the number observations and for the two distributions. Results indicate that, in all cases, when the number of observations is large enough the minimum accuracy of the estimates is approximately constant. As a guideline, for the *elliptical* distribution when the number of observations is above approximately 20, the precision of the pointing bias estimates is around $\pm 0.05^\circ$ and the precision of the peak power estimate is better than $\pm 0.5\,\mathrm{dB}$. In the case of the *circular* distribution, more than approximately 40 observations are required to achieve the same precision in the pointing biases.

Both pointing bias and width estimates are more accurate for the *elliptical* distribution, especially in azimuthal direction, because farther observations carry more information for the retrieval of these parameters. The information content based on the relative antenna-Sun distance of the solar observations can be assessed through inspection of the weighting function matrix components for the solar interference model in Equation 5.3. The weighting functions of interest in this case are the ones that account for the sensitivity of the model to changes in pointing bias and width parameters. For instance, from Equation 5.3 and using Equation 5.6 and Equation 5.7, the azimuthal pointing bias and width weighting functions are given by:

$$\frac{\partial P}{\partial x_0} = \frac{\partial P}{\partial b_x}\,\frac{\partial b_x}{\partial x_0} = \frac{80\log_{10}2}{\Delta x^2}\,x\,, \tag{5.46}$$

and:

$$\frac{\partial P}{\partial \Delta x} = \frac{\partial P}{\partial a_x}\,\frac{\partial a_x}{\partial \Delta x} = \frac{80\log_{10}2}{\Delta x^3}\,x^2\,. \tag{5.47}$$

These weighting functions are plotted in Figure 5.19 for different values of the azimuthal solar width. If it is desired that the Sun-monitoring technique be sensitive enough to detect a change of 0.1° in the azimuthal pointing bias, solar observations with a sensitivity higher than $5\,\mathrm{dB\ deg^{-1}}$ are required. This sensitivity ensures that, when the pointing bias changes 0.1°, the change in the power of the interference is larger than the $0.5\,\mathrm{dB}$ error. In the case of a radar system for which Δx is between 1.3° and 1.4° (corresponding to azimuthal beamwidths between 1.0° and 1.2°, for a typical $\Delta_R = 1.0^\circ$), a change of 0.1° in the azimuthal pointing bias is only

significantly registered by observations located farther than approximately ±0.4°. Analogously, a 0.1° change in the azimuthal width is significant for observations located farther than approximately ±0.7°.

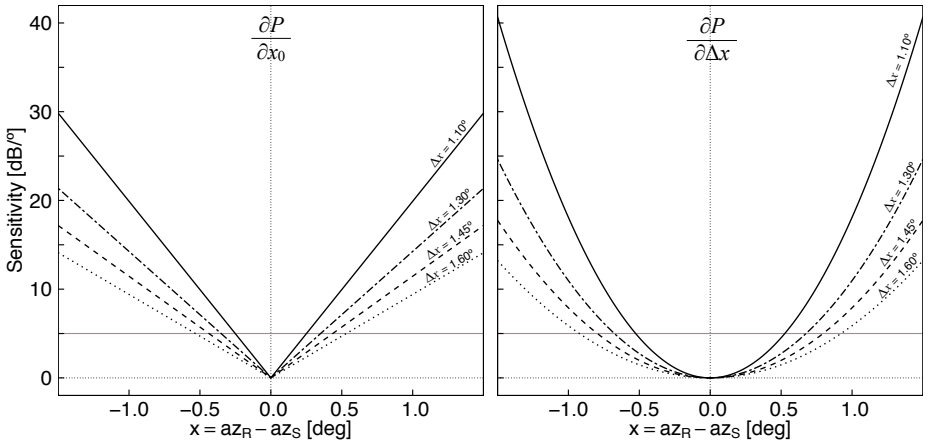

Figure 5.19: Weighting function matrix components of the solar interference model, i.e. sensitivity of the detected solar power to variations in azimuthal pointing bias (left) and azimuthal solar image width (right) as a function of the relative antenna-Sun position of the interference. The horizontal red line indicates the minimum sensitivity required to significantly register a change of 0.1° in the corresponding calibration parameter, assuming a standard deviation of 0.5 dB for the power of the solar interferences.

Going back to the results in Figure 5.18, the estimation of the widths in the 5P fit adds uncertainty to the peak power estimates even when the number of observations is large. This is a result of the systematic fit covariance between the curvature parameters a_x, a_y and the independent term c in the inversion of Equation 5.1. This covariance, exemplified in Figure 5.20, indicates a negative correlation in the error of the estimates and hence, results in a negative correlation between the accuracy of the widths and the peak power.

When the number of observations is small, approximately below 20, pointing bias estimates become unstable and differences between the distributions and between inversion approaches become significant. When the number of observations decreases, the uncertainty of the retrieved model parameters in Equation 5.1 increases and, specially in the case of the 5P fit, the non-linear relationship of the model parameters with respect to the effective solar widths in Equation 5.6 becomes significant. Under these circumstances it is not possible to assume a normal error distribution for the estimated widths. The effect of the non-linearity is stronger the larger the width of the a_x and a_y error distribution, i.e. for increasing uncertainty

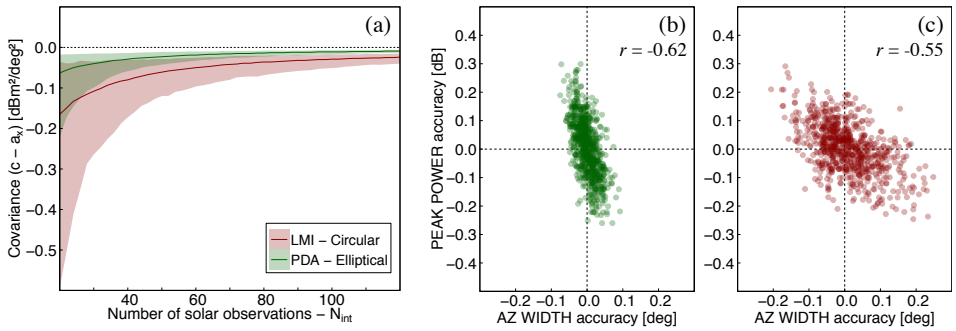

Figure 5.20: Negative fit covariance between the model parameters (panel (a)) results in a negative correlation in the error of the corresponding calibration parameter estimates both for the *elliptical* (panel (b), green) and the *circular* (panel (c), red) distribution of the observations. Panels (b) and (c) display the accuracy results for the 750 iterations corresponding to a number of observations $N_{\text{int}} = 60$.

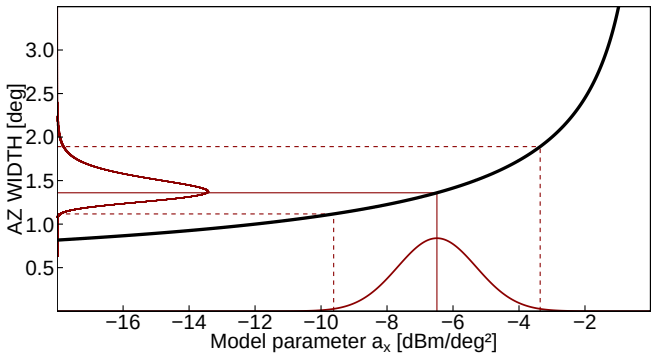

Figure 5.21: Relation between the azimuthal width Δx and the fit model parameter a_x as given by Equation 5.6 (black solid line). Based on this relation the error distribution of the Δx calibration parameter is reproduced in the abscise axis from the normal error distribution of the a_x model parameter drawn in the ordinate axis (red solid lines). Horizontal and vertical lines depict the median (solid lines) and the Q1 and Q99 quantiles (dashed lines) of the distributions in each case.

in the estimated a_x and a_y model parameters. Indeed, the skewness of the error distribution of the solar widths for decreasing number of observations is more noticeable for the *circular* distribution, as observed in Figure 5.18. The effect has been reproduced analytically in Figure 5.21 for the azimuth width estimate, using for the a_x model parameter a normal error distribution of 1.2 dB deg^{-2} standard deviation. This standard deviation value has been chosen equal to the standard deviation of the a_x parameter calculated for the *circular* distribution from the 750 iterations for

$N_{\text{int}} = 30$. The reproduced shape of the azimuthal width error distribution in Figure 5.21 matches the result for $N_{\text{int}} = 30$ from the simulations shown in Figure 5.18 for the *circular* distribution. Note that the error distribution of the pointing biases and the peak power are also affected to a lesser degree because they are derived from the estimated widths through Equation 5.7 and Equation 5.8. Consequently, a minimum number of observations is required for a consistent application of a LLS inversion in the 5P model fit, preferably more than 20 or even 40 solar observations in the case of a low sensitivity radar.

5.5.2 Error of the solar observations

The analysis carried on in the previous section indicates that having a large enough number of solar observations available for the fit is critical in bounding the accuracy of the retrieved calibration parameters within the desired levels. However, for a fixed number of observations, the precision of the retrieved calibration parameters also depends on the error in the power of the solar observations.

As shown in Figure 5.22, the median RMSD of the fit is a good indicator of the error of the observations. When the variance of the power is different for each observation, i.e. when the data set is heteroscedastic, as is the case for actual solar observations in Figure 5.13, the median RMSD can be used instead as an estimator of the average error of the set. This is the reason why the median RMSD for actual fit results is higher for the PDA radar than for the LMI radar, see Table 5.2. In any case, the RMSD results can be used to know the number of observations needed for an accurate monitoring of the calibration parameters and/or to assess whether the number of observations available ensures the required precision.

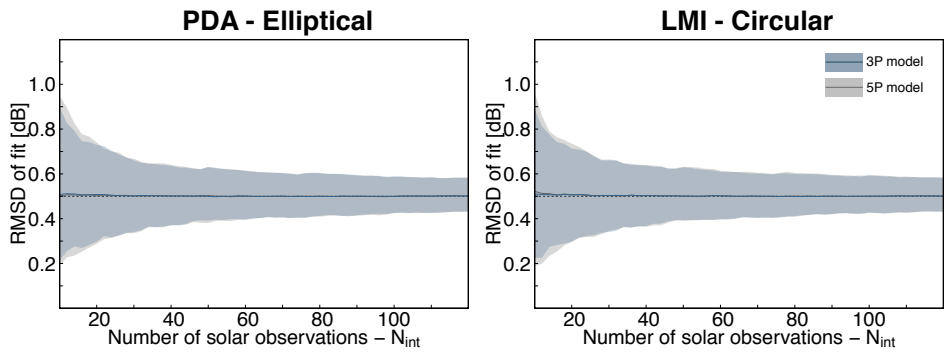

Figure 5.22: As Figure 5.18 but for the RMSD of fit residuals. The results correspond to simulations of solar observations with an added noise level of 0.5 dB.

The analysis sketched in Figure 5.17 has been repeated for added noise levels ranging from 0.1 dB to 1.0 dB. Figure 5.23 displays the number of observations required to achieve the desired precision for each parameter as a function the noise level. The minimum number of solar interferences has been calculated as that for which the Q1- Q99 inter-quantile range for the accuracy of the estimates is below the desirable minimum precision specified in Table 5.4. These precisions have been chosen as those typically desirable for an adequate radar calibration quality control in an operational environment.

Table 5.4: Values of the desirable minimum precision for the calibration parameters of the Sun-monitoring method.

Parameter	Min. Precision
P_{TOA} [dB]	± 0.5
x_0, y_0 [°]	± 0.1
$\Delta_{C,\mathrm{eff}}$, Δ_C [°]	± 0.1

The results in Figure 5.23 indicate that a number of 20 to 40 solar observations ensures the desired precision for all the parameters estimated in the 3P model fit for noise levels up to 0.8 dB. Accurate retrieval of the widths in a 5P model requires significantly larger sets of observations. For the *elliptical* distribution, a set of 60 observations ensures the $\pm 0.1°$ precision in the estimated widths for noise levels up to 0.7 dB. In the case of a *circular* distribution, for noise levels higher than 0.2 dB more than 120 solar observations are required for a precise retrieval of the azimuthal width, which is a requirement of difficult compliance because for low sensitivity radars the number of interferences detected per day is generally below 20.

From the results for the XRAD summarised in Table 5.2, it can be derived that for the PDA radar, with a median RMSD around 0.6 dB, a daily number of observations between 50 and 60 guarantees an accurate retrieval of all calibration parameters in a 5P model fit. Since PDA detects between 35 and 60 observations on a daily basis, it is concluded that the 5P model inversion can be reliably applied. Conversely, the LMI radar detects between 10 and 20 solar interferences, a number that for a median RMSD of about 0.4 dB ensures the required accuracy only for the pointing biases and the peak solar power.

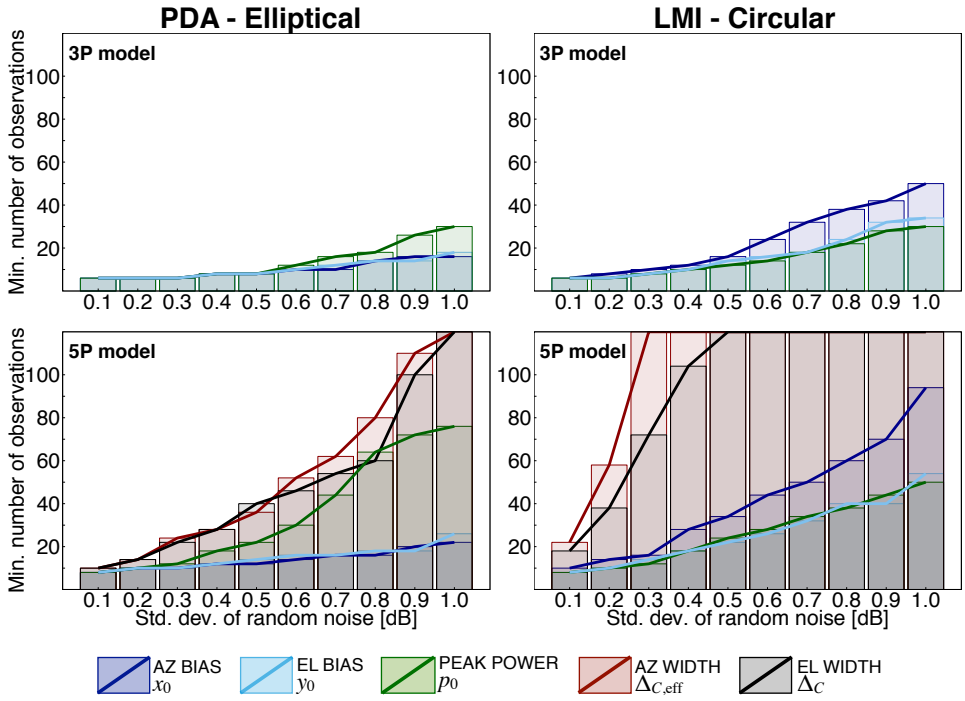

Figure 5.23: Minimum number of solar observations needed to achieve the precision specified in Table 5.4 for each calibration parameter, as a function of the noise level.

5.6 Conclusions

The online solar method for combined monitoring of weather radar antenna pointing biases and receiver calibration has been adapted and applied for the weather radar network of the SMC. A theoretical derivation of the physical model for weather radar solar observations has defined the model validity ranges based on system settings and has provided a means for estimating the effective solar image width in reception of a scanning antenna. In particular, it has been found that the proposed Gaussian model adequately describes the solar interferences detected by the radar for elevations under 10°, when the ratio between the radial resolution and the convolution width is below 1.5.

Prior to model inversion, application of a non-iterative method based on robust statistical estimators has proven very efficient for the removal of leverage model outliers, in the present case attributed to non-solar, commonly RLAN, interferences. When the antenna pointing errors are not significant, the criterion might be

adjusted for rejection of subtle outliers such as solar signals attenuated by rain or biased by ground or precipitation echoes, aiming for an improved accuracy in the model parameter retrieval.

The ability of the adapted algorithm to detect miscalibrations and antenna pointing and system anomalies has been tested in the application to a year of daily solar observations for three different XRAD weather radars. It has been noticed that the sensitivity of the radar system conditions the number and distribution of the observations, which determines the information available for the retrieval of the calibration parameters in the model fit. Consequently, the performance of a full five-parameter retrieval (5P) in comparison to a three-parameter (3P) model fit with fixed solar image widths has been evaluated based on the dissimilar information content in the collection of daily solar observations detected by two of the radars. For the more sensitive radar, the 5P model inversion approach explains better the observations, yielding stable and precise parameter estimates with an optimal goodness of fit. Conversely, in the case of a less sensitive radar system, which detects the solar signal only when the antenna is pointing close to the Sun-disk centre, the 5P model inversion does not improve the quality of the fit with respect to the 3P approach.

These results have been further examined in a performance analysis, in which the solar observations have been simulated and the inversion procedure has been reproduced and systematically repeated under controlled conditions to extract statistical information. It has been found that, in a 5P model fit, the estimated widths and the peak power are correlated in such a way that inaccuracies in the width estimates imply an inaccurate peak power estimate. Nevertheless, a large enough number of observations ensures that the accuracy of all retrieved parameters in a 5P model fit is within the desirable limits, as long as the system's sensitivity allows to detect solar observations when the antenna is pointing farther than approximately $\pm 0.7^\circ$ from the Sun-disk centre; i.e. observations which contain significative information for the retrieval of the widths. Under these circumstances, it has been determined that a number above 60 observations may be appropriate for accurate monitoring of the parameters. This number of solar interferences may be collected on a daily basis by a sensitive radar (Holleman et al., 2010b) or can otherwise be achieved by gathering the observations detected during three consecutive days (Frech, 2009), a time scale short enough to assume that the solar flux does not change significantly.

On the other hand, when the dataset systematically lacks information for the retrieval of the widths -as seen in the cases of a limited sensitivity and of an anoma-

lous data distribution- the accuracy of the parameters estimated in the 5P model is dominated by the ill-conditioning of the inverse problem. In particular, the number of observations required to accurately estimate the solar image widths is larger than 120, which is a difficult number to achieve by a low sensitivity radar. From the point of view of antenna alignment and receiver calibration status assessment, in these cases, application of the 3P model may be more appropriate for an improved accuracy and stability of the estimates.

6

Antenna pointing accuracy

* The present chapter has been adapted from: Altube, P., J. Bech, O. Argemí, T. Rigo, and N. Pineda, 2016: Intercomparison and potential synergies of three methods for weather radar antenna pointing assessment. *J. Atmos. Oceanic Technol.*, 33, 331-343, doi: 10.1175/JTECH-D-15-0075.1

Antenna boresight alignment and pedestal levelling status assessment have been traditionally included in the radar calibration procedures as they are critical for georeferencing radar measured variables (Gekat et al., 2004; Vega et al., 2012). Indeed, the accuracy of the antenna alignment constitutes a basic quality factor for

primary data and downstream products. For instance, an antenna pointing error of 0.2° either in the horizontal or vertical plane, produces an approximate geolocation error of 700 m at 200 km ranges, which may be relevant for many applications such as echo height computing for hail probability assessment (Delobbe and Holleman, 2006), topographical beam blockage correction (Bech et al., 2003) or precipitation estimates in small mountain basins for landslide or debris-flow forecasting (Berenguer et al., 2015). Based on the experience of the XRAD weather radar operators, geolocation errors due to an inaccurate antenna alignment affect the generation of QPE maps and the issuance of heavy precipitation warnings, particularly when these evens take place close to boundary areas between different regions or close to the coastline.

These examples point out the importance of routine checks of the weather radar antenna pointing accuracy. Calibration of the absolute (mechanical and boresight) bearing requires an external target of precisely known location. As studied in the previous chapter, the Sun constitutes a readily available target that can be reliably used for monitoring the absolute antenna pointing accuracy. Other common practice calibration methods (see, for instance, Manz et al., 2000) rely either on active targets, e.g. directive antennas and transponders; or on fixed-ground and elevated passive targets, e.g. radio tower, reflector mast, orographic features or obstacles and balloon/aircraft borne reflectors. Calibration using balloon or aircraft mounted targets as reference requires interruption of the radar operation and hence the temporary suspension of the radar product generation chain. In addition, if frequent checks are required, these methods may result logistically and economically costly. On the other hand, ground targets are usually not suitable for elevation calibrations (Divjak, 2009). In this regard, Delrieu et al. (1995) developed an algorithm for characterisation of the mountain echoes detected by a ground-based weather radar and successfully used the clutter field as reference for estimation of the azimuthal antenna pointing accuracy. A fully automatic extension of the procedure is described in Rico-Ramírez et al. (2009).

Within this framework, testing available antenna alignment monitoring procedures is potentially useful for weather radar communities requiring high quality data observations. In this chapter, three methods for estimation of the weather radar antenna azimuth and elevation pointing offsets are compared. All three methods have been implemented and are operative for the XRAD weather radar network. Two of the methods reviewed use the known location of the Sun as a reference. The first of these methods is based on an offline scan of the solar disk. The second method is the online Sun-monitoring method analysed in Chapter 5. The third method con-

sists on correlating measured ground clutter echoes with echoes simulated using a high-resolution digital elevation model.

The main objectives of the present chapter are to review the operation and characteristics of each of the three antenna pointing methods, to study their performance in actual operative conditions and to examine the reasons for the discrepancies between the reported pointing bias estimates, with the aim of laying the groundwork for an optimised individual or combined application and interpretation of the methods. The inter-comparison is tackled by first analysing the performance of the methods and identifying the discrepancies in the pointing biases reported in a one-month, short term campaign during which the offline Sun-scan method was run on a daily basis. The results collected in a one-year long period are then studied, based on the measurement conditions and on the procedure followed by each of the methods, to understand and discuss the reasons for the discrepancies found in the short term analysis.

6.1 Antenna pointing monitoring procedures for the XRAD

In this section, the three methods for monitoring weather radar antenna pointing accuracy are described in detail. Table 6.1 compiles main characteristics of the methods as implemented for the XRAD radar network.

Table 6.1: Inter-comparison of relevant characteristics of ground clutter returns (GC), Sun interferences (SI) and Sun scan (SC) methods as implemented for the XRAD radar network.

	Online	Precip. immune	AP immune	Elevs. [deg]	Accuracy (az/el) [deg]	Quality indicator
GC	yes	no	no	0.6	0.5 / 0.1	Max. correlation
SI	yes	≈yes	≈yes	0.6 - 8	0.1 / 0.1	RMSD/N_{int} Error of estimates
SC	no	yes	yes	20 - 60	0.1 / 0.1	Peak power SNR Fit error

6.1.1 Ground clutter returns (GC method)

In the first method (hereafter GC), fixed structures of ground clutter echoes observed in radar image scans at low elevations are compared to ground clutter returns modelled using a high resolution Digital Terrain Elevation Model (DTEM). The module running the GC method at the SMC is part of the MAFRAD set of radar monitoring tools implemented by the CRAHI, introduced in Chapter 3, Subsection 3.3.3.

The DTEM used for the ground clutter field simulations has a grid resolution of 30 m and a resolution of 1 m in elevation. Considering clear air and standard atmospheric propagation conditions, ground clutter reflectivity fields are simulated for a collection of antenna elevations using the algorithm by Delrieu et al. (1995). The algorithm models the interaction with topography of three-dimensional electromagnetic pulses. The resolution volume of the radar beam is modelled by a Gaussian angular power pattern and a range weighting function as the one proposed in Doviak and Zrnič (1984).

Simulated fields are available for an elevation range of ±3° at 0.02° steps. These simulations are correlated with the observed field, built as the average of the daily set of clutter reflectivities collected at 0.6° scans. In addition, predicted fields are azimuthally rotated at 0.1° steps to compute correlations for azimuth lags in a ±3° range. The combination of elevation and azimuth lags yielding the maximum correlation coefficient represents an estimate of the antenna pointing biases in both directions. To achieve co-location of the simulated and observed clutter bins for computation of the correlation coefficient, the simulated field is averaged to the nominal resolution of the PPI field (1° in azimuth and 1 km in range) and the observed field is spline interpolated to the locations of the simulation.

The antenna pointing offset estimates for XRAD radars are available online on a daily basis. Since no classification of the observed ground clutter echoes is applied to the observed clutter field, the accuracy of the pointing bias estimates may be compromised by the presence of precipitation or by the modification of the ground clutter echoes due to anomalous atmospheric propagation conditions. Consequently, these factors must be monitored to warrant valid results.

Approximate accuracy limits of the method reported by the GC module developers are 0.5° in azimuth and 0.1° in elevation. In accordance with the accuracy limits, the operative module provides the values of the estimates rounded to 0.1° precision both in azimuth and elevation. Hence, the GC method as implemented at the SMC is aimed at quantifying elevation antenna pointing errors while only

suitable for the detection of large significative pointing errors in azimuth. Due to the 1° nominal azimuthal resolution of the fields, small inaccuracies in the simulation parameters may result in inaccuracies of up to 0.5° in the estimated azimuth pointing biases, which may give rise to geolocation errors larger than 1000 m at the farthest ranges. As an example of the sensitivity of the method to an inaccurate azimuthal resolution parameter, Figure 6.1 shows a simultaneous change in the GC reported biases for all XRAD radars when, in December 2014, the parameters of the long range scanning task were modified to change the actual Δ_R resolution of 0.8° to the desired nominal value of 1°.

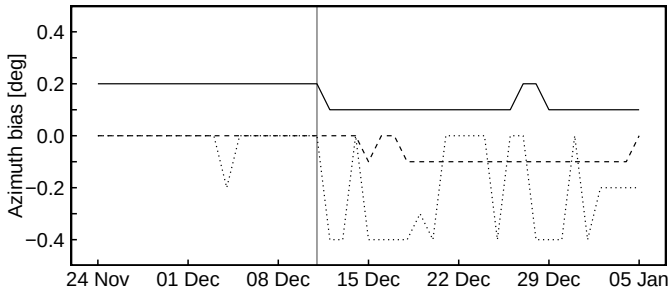

Figure 6.1: Azimuthal pointing biases reported by GC method before and after a change in the nominal resolution of the scanned radial on 11 December 2014: CDV radar (solid line), LMI radar (dotted line) and PDA radar (dashed line).

6.1.2 Solar interferences (SI method)

The second procedure is the online Sun-monitoring method (hereafter SI) by Holleman and Beekhuis (2004). As detailed in Chapter 4, online application of the SI method requires automatic detection of solar artefacts in polar reflectivity data. Then, as explained in Chapter 5, a theoretical model for the power of the solar signal is fitted to the collection of solar observations to estimate the antenna pointing biases in azimuth and elevation (Huuskonen and Holleman, 2007).

The SI method implemented at the SMC is adapted to the mid range data (80 km to 130 km) available from the XRAD weather radar network. The original algorithm has been modified to minimise the effect of precipitation in the characterisation of the detected solar signal (Chapter 4, Subsection 4.1.2) and a methodology for removal of strong outlying observations is applied (Chapter 5, Section 5.3). Atmospheric anomalous propagation conditions may lead to an inaccurate positioning of the Sun with respect to the antenna, mainly for observations collected at low

elevations. However, its effect upon the retrieved pointing biases lies within the accuracy limits of the method, likely because the majority of the observations considered for the model fit remain unaffected, see Section 6.2. The accuracy of the method is better than 0.1° if the number of observations to be fitted is above approximately 20 (see Chapter 5, Section 5.5). Also, the uncertainties of the estimated pointing biases, obtained from the covariance matrix of the linear least-squares fit, may be considered indicative of the quality of the dataset since they take into account the spread and distribution of the observations (Bevington and Robinson, 1969).

6.1.3 Sun scan (SC method)

The last of the methods considered (hereafter SC) is based on an offline scan of the solar disk and is implemented commercially by several weather radar manufacturers and of common application in routine technical maintenance tasks. In this case the use of a Sun calibration utility is described, supplied within the Vaisala IRIS radar software package, which outputs the solar SNR data resulting from a sector scan around the expected position of the Sun (Vaisala, 2014a). The utility itself uses the local computer time to calculate the current solar position and controls the antenna scan attending to the user specifications. In the data processing stage, SNR data are thresholded above a user specified level and a 2-dimensional second order polynomial fit is applied to obtain estimates of the peak solar SNR as well as the solar image widths. Data with a SNR value of 3 dB or more under this estimated peak power are then discarded and a second 2-dimensional polynomial fit gives the solar position estimates in azimuth and elevation. Comparison of these position estimates with the solar position as derived from local system time identifies antenna pointing offsets.

In the case of the XRAD, the SC routine is configured to perform the solar scan in a sector spanning 4° by 4° in azimuth and elevation with a resolution of 0.2°. The sector is scanned azimuthally, starting below the expected solar elevation and stepwise moving upwards. The SC utility corrects for the apparent continuous motion of the Sun during the sector scan, recalculating the solar position at the beginning of each sweep and subtracting the difference from all angles in that sweep. Within the specified angular resolution bins, 64 samples are taken at a PRF of 1000 Hz and all range bins further than 20 km away from the radar are averaged to compute the corresponding SNR value.

The accuracy of the SC estimated biases depends on the accuracy of the solar

centre position and on the accuracy of the peak solar power position estimated from the sector scan data processing. The accuracy error of the solar centre position is below 0.01° for an error of the order of a few seconds in the local time reading (Vaisala, 2014a, Section 3.5). In turn, the accuracy of the peak solar power position depends on a number of factors such as the antenna elevation angle at which the measurement is performed, the quality and number of valid data or the solar emission pattern. Most of these factors are quality controlled by the utility itself while running, through evaluation of indicators like the image area covered by valid data, SNR of the peak power and RMSD of the fit. Given the similarities in the data collection and fitting process, it is estimated that the peak position accuracy is around 0.05° as in the case of the SI method. Under these considerations, the accuracy of the SC method is assumed to be better than the 0.1° value given by the resolution of the solar scan dataset.

Routine checks of the XRAD radars' antenna alignment by means of the SC method are bimonthly carried out by technicians. Following the recommended procedures established for the XRAD, SC measurements are taken only in clear-air days and the utility is run twice, in the morning and in the afternoon, always when the Sun is at an elevation between 20° and 60°. These procedures are set to ensure the pointing bias estimates are not affected by precipitation or anomalous refraction conditions. From February to March 2014, a dedicated SC campaign was carried out to assess the stability of the method and the resulting antenna positioning errors. The SC utility was run in the morning and in the afternoon on a daily basis (excluding weekend and rainy days), summing up a total of 22 days. Measurement times were fixed, generally around 1000UTC and 1400UTC, to ensure that morning/afternoon solar zenithal positions were similar and above 20° and that the solar azimuthal positions would not vary strongly throughout the campaign. The results of the campaign are presented in the upcoming Section 6.3.

6.2 Quality control

In the upcoming sections, the analysis and comparison of the antenna pointing monitoring methods is presented, based on the results of their application to the XRAD radars for the period from April 2013 to March 2014, with particular insight into the dedicated short term campaign carried out from February to March 2014. Prior to the analysis, the datasets for the GC and SI method have been quality-subset, attending to the factors affecting the method performance and/or to characteristic

quality indicators in each case. The data-series of the SC method is accepted as-is, since the quality control is applied by the SC commercial utility itself during the measurement procedure.

Pointing bias estimates by the GC method have been selected based on the atmospheric conditions, keeping results corresponding only to days with clear skies and standard propagation conditions. Days with standard atmospheric propagation conditions have been identified using VRG_{1000} and I_D data calculated from radiosonde observations, by application of the thresholds tabulated in Bech et al. (2007a). Precipitation accumulation maps for the selected days, as those described by Trapero et al. (2009), have been further inspected to discard those for which any precipitation above 0.1 mm was present. Figure 6.2 shows the results of the classification: 13.5 % of the total of days of the long term period are identified as clear air days with standard propagation conditions.

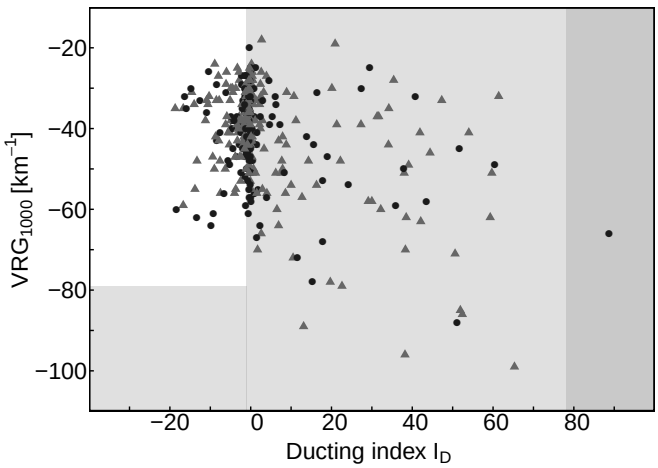

Figure 6.2: Atmospheric propagation conditions at 1200UTC from April 2013 to March 2014. Ducting Index (I_D) and Vertical Refractivity Gradient (VRG_{1000}) values derived from radiosonde measurements are used to classify the daily propagation conditions: standard (white), super-refraction (light grey) and ducting (dark grey). Triangles represent clear air days while black dots represent days for which any precipitation above 0.1 mm was present.

Based on this classification, the influence of precipitation and anomalous propagation (AP) on the pointing biases estimated by SI method has been investigated for the PDA radar. The PDA radar has been chosen for the analysis for being the XRAD radar for which the most reliable SI method results are obtained, as seen in Chapter 5, and because it presents no significant pedestal levelling error (see

Subsection 6.4.1). SI results have been split into four groups corresponding to different atmospheric conditions: clear air and standard propagation, precipitation only, AP only and both precipitation and AP. As shown in Figure 6.3, the differences between the antenna pointing offsets reported under the different atmospheric conditions differ in less than 0.01°. In addition, an statistical test comparing the mean pointing biases reported under clear air and standard propagation conditions with the mean reported under each of the other conditions shows that these differences are not significant. Only the combination of precipitation and anomalous propagation seems to have an slight effect on the elevation pointing offsets but the bias is minimal and below the accuracy limits of the SI method.

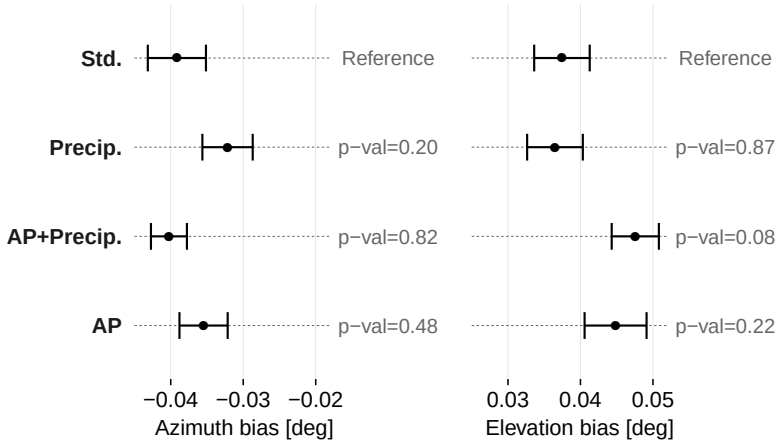

Figure 6.3: Mean antenna pointing biases estimated by the SI method for PDA radar, classified according to the atmospheric conditions: clear air and standard propagation (Std.), precipitation only (Precip.), anomalous propagation only (AP) and both precipitation and anomalous propagation (AP+Precip.). Error bars illustrate the standard error of the mean. Only SI estimates derived from fits to solar observation data sets larger than 20 are considered. Given are the p-values corresponding to t-value tests for difference between the mean under standard conditions and the means under non-standard conditions. P-values larger than 0.05 (95 % level) indicate a non-significant difference with respect to the standard conditions.

The quality selection of SI results is therefore based on the number of solar observations available for the fit and on the uncertainty of the parameters derived from the fit. In particular, a minimum number of 20 solar observations is required for acceptance of the fit results, and only errors below 0.05° in the pointing offsets and below 0.1° in the width estimates are allowed.

6.3 Direct comparison in a short-term campaign

Figure 6.4 displays an example of the comparison of the antenna pointing biases obtained from the three methods for the short campaign period from 10 February 2014 to 14 March 2014 for the CDV radar. Results from morning and afternoon measurements using the SC utility have been averaged into a single daily estimate by application of a mean weighted by the fit error. First inspection of the figure indicates that the precision of the estimates by the Sun-based methods, SI and SC, is below 0.05°. However, a systematic difference of about −0.1° between the biases from SI and SC methods is noticeable, both in azimuth an elevation.

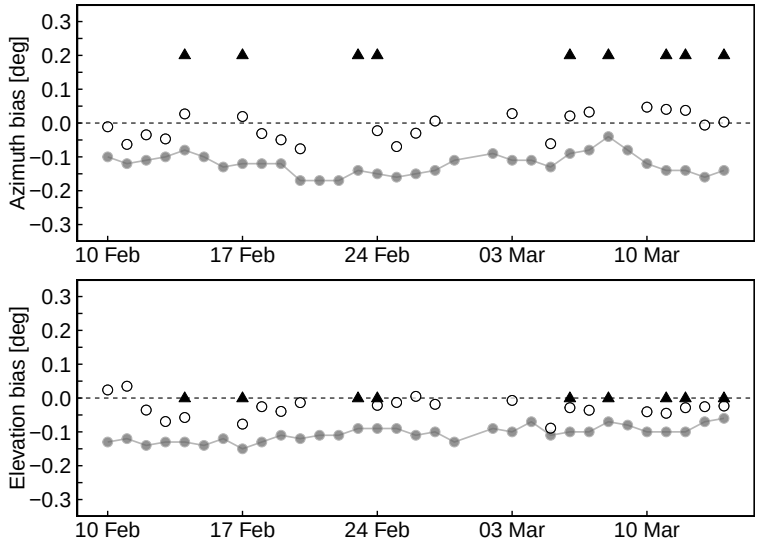

Figure 6.4: Antenna pointing bias estimates in azimuth (top) and elevation (bottom) for the CDV radar during the period from 10 February 2014 to 14 March 2014. Results for the three different antenna alignment methods are displayed: GC method (black triangles), SI method (grey circles) and SC method (white circles). For the sake of clarity, SI method results are shown connected by a line.

As reasoned in the upcoming Subsection 6.4.2, the precision of the biases estimated through the GC method is below the 0.1° output precision given by the operative module and, therefore, the day-to-day variability of the estimates is not perceivable in the results presented. This is not critical in the case of the azimuth biases because the correlation coefficients between the observed and simulated clutter fields are calculated in 0.1° steps. However, for the elevation biases, an output precision of 0.01°, finer than the one currently provided by the operative module,

would be desirable for an adequate quality control of the antenna alignment.

6.3.1 East/West splitting

The SC estimates obtained in the morning and in the afternoon have been separately analysed for a more detailed insight. SC results have been classified into East (SC-E) and West (SC-W) according to the azimuthal position of the antenna with respect to the North (0°) at the time of the measurement. During the campaign, SC-E measurements were taken at azimuthal positions between 140° and 160° while SC-W measurements were taken between 210° and 240°.

In the case of SI method, computation of separated bias estimates for East and West positions has also been possible. SI estimates have been computed again, differentiating between East (SI-E) and West (SI-W) by application of the method to solar interferences detected either at sunrise or sunset respectively during three consecutive days. Conditioned by the local solar sunrise and sunset positions for the considered dates, SI-E solar observations were collected at azimuthal positions between 95° and 115° and SI-W observations at positions between 225° and 265°.

As seen in Figure 6.5, this separation reveals a systematic difference between the elevation biases measured at East and West positions of the CDV radar antenna. The East-West offset is ca. 0.09° for SC method and reaches 0.16° for SI method. In turn, no significative difference in the azimuth bias estimates is noticeable. These results altogether indicate a possible inclination of the antenna rotation plane with respect to the horizontal plane, often associated with pedestal levelling errors (Frech, 2009). The possibility of the East-West differences being related to a misalignment between solar disk centre and the "microwave centre" (Chandrasekar et al., 2014) has been discarded given the length of the time period studied (of the order of the solar rotation period) and the stability of the differences found.

Table 6.2 presents the statistics of the biases estimated during the short term campaign period and for all three XRAD radars. Examination of the results shows how the application of the SI method to all solar interferences, collected both at sunrise and sunset, yields bias estimates which are approximately the average of those biases computed separately from East and West interferences. In addition, a significative East-West offset in the elevation biases from SI and SC methods has also been detected for the PDA radar.

In the azimuthal direction solar features are smoothed and attenuated due to the scanning motion and the precision of the estimates may be affected by a low sensitivity of the radar system. Average SNR values of the peak solar signal derived

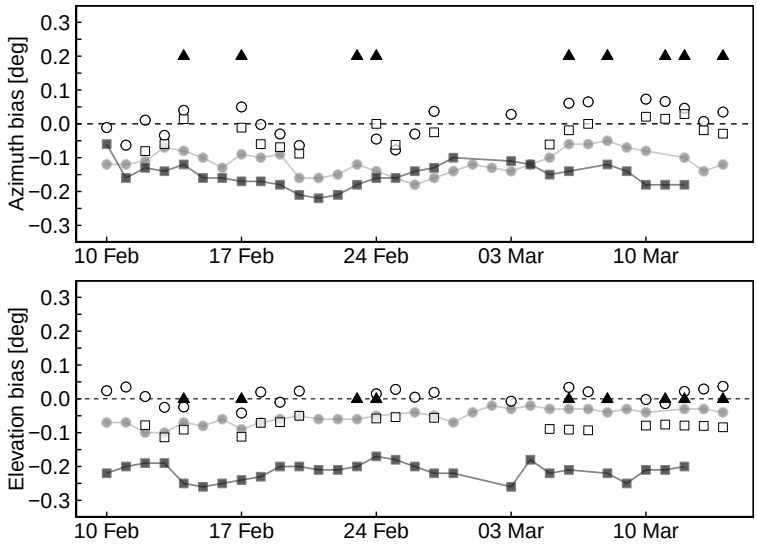

Figure 6.5: As Figure 6.4 but with the estimates from Sun-referenced methods separated according to the East-West azimuthal position of the antenna at the time of the measurement: GC (black triangles), SI-E (light grey circles), SI-W (dark grey squares), SC-E (white circles) and SC-W (white squares).

from the SC method are, in linear units, 3 for the LMI, 4 for the CDV and 6 for the PDA. Hence, a slightly larger day-to-day variability of azimuth bias estimates is expected in the cases of the LMI and the CDV radars. Note, however, the remarkably larger variability in the SC azimuth biases for the LMI (Table 6.2). This has been attributed to the presence of a significative backlash in azimuth, associated with a severe wearing of the gear cogs of the azimuth resolver. This problem was detected in due course and solved by replacement of the resolver on the 14 April 2014.

As reasoned in Chapter 5, the radar sensitivity may also affect the precision of the SI method estimates. However, this is not as clearly reflected in the short term statistics of the estimates given in Table 6.2 due to the quality selection of the results described in Section 6.2. Indeed, accounting for all results collected in the one-year long time period, the valid daily SI results remaining for the LMI after the quality selection has been reduced to a 55 % of the total, while the CDV and the PDA have kept 75 % and 84 % respectively.

Finally, the clear discrepancies of the GC azimuth biases with respect to the Sun-based methods are within the accuracy limit of 0.5° established for the GC method.

Table 6.2: Mean and standard deviation of antenna pointing bias estimates for the XRAD radars from 10 February 2014 to 14 March 2014. Results from Sun-referenced methods are separated according to the East-West azimuthal position of the antenna at the time of the measurement. Results of application of the SI method to all interferences are also shown for comparison.

		GC	SI	SI-E	SI-W	SC-E	SC-W
CDV	az [°]	0.2 ± 0.0	-0.12 ± 0.03	-0.11 ± 0.03	-0.15 ± 0.04	0.01 ± 0.05	-0.03 ± 0.04
	el [°]	0.0 ± 0.0	-0.11 ± 0.02	-0.05 ± 0.02	-0.21 ± 0.02	0.01 ± 0.02	-0.08 ± 0.02
LMI	az [°]	0.2 ± 0.1	-0.27 ± 0.02	-0.25 ± 0.03	-0.31 ± 0.02	0.02 ± 0.12	0.05 ± 0.15
	el [°]	-0.4 ± 0.0	-0.14 ± 0.02	-0.16 ± 0.02	-0.12 ± 0.02	-0.04 ± 0.01	-0.01 ± 0.02
PDA	az [°]	0.0 ± 0.0	-0.01 ± 0.01	0.02 ± 0.01	-0.05 ± 0.02	-0.06 ± 0.02	-0.07 ± 0.02
	el [°]	0.2 ± 0.0	0.02 ± 0.01	-0.01 ± 0.01	0.07 ± 0.02	0.04 ± 0.02	0.12 ± 0.02

6.4 Analysis of discrepancies

6.4.1 SI and SC methods: antenna system levelling

The East/West splitting for both the SI and SC methods described in the previous section has allowed, on a long term analysis, to examine the dependence of the elevation pointing biases (δ_θ) upon the azimuthal position of the antenna (ϕ). In the presence of a levelling error this dependence is expected to be of the type:

$$\delta_\theta = \delta_{\theta,0} + \beta_0 \cos(\phi - \phi_0) \,, \tag{6.1}$$

where β_0 is the angle of inclination between the rotation axis and the vertical, ϕ_0 is the azimuthal direction of the inclination with respect to the North and $\delta_{\theta,0}$ is a systematic elevation error, as sketched in Figure 6.6. The latter includes the antenna axis elevation offset and any (boresight) misalignment between this axis and the electrical axis. Equation 6.1 is an adaptation of the model presented in the exhaustive work by Muth et al. (2012).

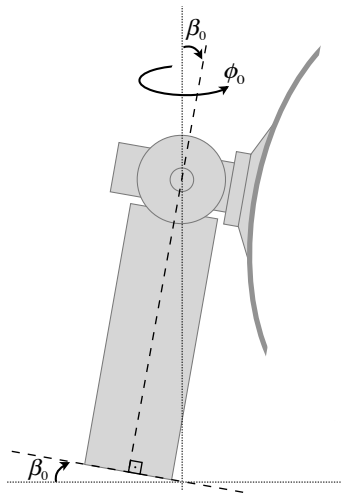

Figure 6.6: Sketch of the angles characterising an antenna pedestal levelling error.

The East-West implementation of SI method has been applied from the 1 April 2013 to the 31 March 2014. The collection of three-day sunrise or sunset solar interferences lies within azimuth stripes of 5° to 10° width and the median position has been used as reference for the retrieved bias estimates. The time period considered

covers the whole solar cycle of local sunrise and sunset azimuthal positions, spanning from 55° to 125° and from 230° to 300°, respectively. The SC method results have also been included in the analysis, encompassing both the bimonthly technical tests throughout this period and the short term campaign results presented in the previous section.

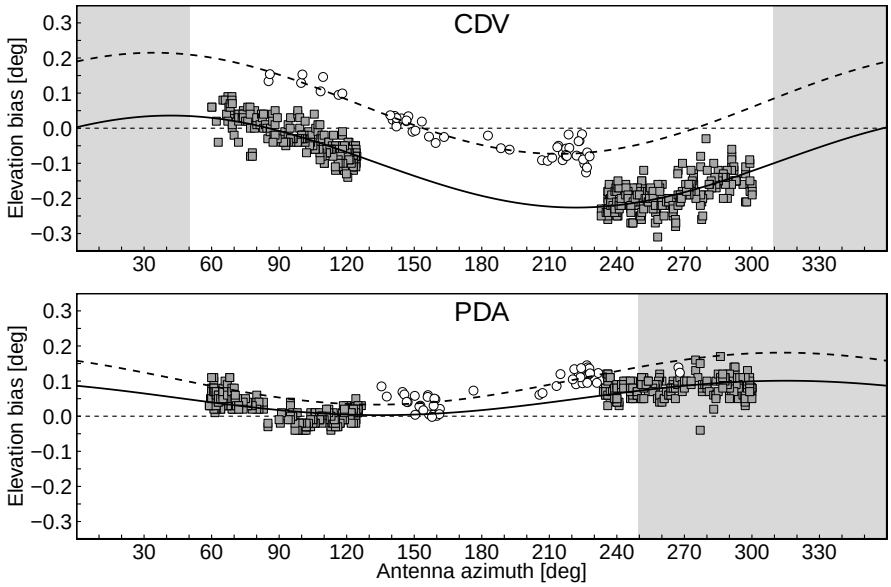

Figure 6.7: Elevation pointing biases estimated for the CDV (top) and the PDA (bottom) radars from 1 April 2013 to 31 March 2014 as a function of the azimuthal position of the antenna: SC (white circles) and SI (grey squares) method estimates. Lines represent the resulting levelling error model (Equation 6.1) fits to SC (dashed line) and SI (solid line) estimates. Grey shaded sectors indicate the influential azimuth regions determining the estimates given by the GC method (see Subsection 6.4.2).

Figure 6.7 shows the azimuthal dependence of the elevation biases retrieved through SI and SC methods for the CDV and the PDA radars. The LMI case is not presented because no consistent difference between the East and West pointing biases has been found, not in the short term campaign nor in the long term period. For the CDV and the PDA radars, a difference between East and West results is appreciable in both cases and a sinusoidal dependence is perceived when all results are considered together in Figure 6.7. Nonlinear least-squares fits of the levelling error model in Equation 6.1 have been applied independently to SI and SC estimates. The model parameters retrieved in each case are detailed in Table 6.3. Outcomes of the fits indicate that for the CDV radar a significative inclination of ca.

0.14° was present at an azimuth within 30°-40° from North. Although a noteworthy difference of 0.15° between SI and SC systematic offset estimates is quantified, the levelling errors derived from both methods are in accordance. In the case of the PDA radar, the inclination of about 0.05° found at an azimuth around 315° is not significative given the precision of the SI and SC methods and lies within the margins accepted for the antenna pointing accuracy. The difference between SI and SC systematic offset estimates for PDA is minor, around 0.05°. The reason for the differences between SI and SC offsets is discussed in Subsection 6.4.3.

Table 6.3: Levelling error model (Equation 6.1) parameters and their errors as retrieved for the CDV and the PDA radars in a nonlinear least-squares fit of the elevation bias estimates from SI and SC methods.

	Data	Offset ($\delta_{\theta,0}$) [°]	Inclin. (β_0) [°]	Dir. (ϕ_0) [°]
CDV	SI	-0.097 ± 0.002	0.132 ± 0.004	42 ± 2
	SC	0.07 ± 0.01	0.15 ± 0.01	32 ± 4
PDA	SI	0.052 ± 0.001	0.049 ± 0.002	315 ± 3
	SC	0.11 ± 0.02	0.07 ± 0.02	313 ± 17

6.4.2 GC method: precision and influential clutter bins

The GC method calculates the Pearson correlation coefficient (ρ) between the observed (Z^{o}) and simulated (Z^{s}) reflectivities of ground clutter echoes for different combinations of δ_ϕ and δ_θ azimuth and elevation pointing biases:

$$\rho(\delta_\phi, \delta_\theta) = \frac{1}{N-1} \sum_{\phi} \sum_{r} \left[\frac{Z^{\mathrm{o}}_{r,\phi} - \overline{Z^{\mathrm{o}}}}{\sigma^{\mathrm{o}}} \right] \left[\frac{Z^{\mathrm{s}}_{r,\phi}(\delta_\phi, \delta_\theta) - \overline{Z^{\mathrm{s}}}}{\sigma^{\mathrm{s}}} \right], \tag{6.2}$$

where N is the number of clutter bins considered; $\overline{Z^{\mathrm{o}}}$, $\overline{Z^{\mathrm{s}}}$ are the average reflectivities and σ^{o}, σ^{s} the standard deviations of the observed and simulated ground clutter reflectivity fields, respectively. (r, ϕ) are range and azimuth positions indexing each particular clutter bin within the fields.

The function $\rho(\delta_\phi, \delta_\theta)$ has a maximum at $(\delta_{\phi,0}, \delta_{\theta,0})$; the latter values constitute the antenna elevation and pointing biases reported by the GC method. Table 6.4

gives the average and standard deviation of the maximum correlation coefficient $\rho(\delta_{\phi,0}, \delta_{\theta,0})$ for the XRAD radars during the long time period from 1 April 2013 to 31 March 2014.

Table 6.4: Values of variables relevant for the correlation coefficient calculation and for the performance of GC method when applied to the XRAD radars.

	CDV	LMI	PDA
Max. Correlation	0.67 ± 0.01	0.66 ± 0.03	0.789 ± 0.008
Std. Dev. of Z [dB]	≈ 16	≈ 10	≈ 15
Num. of bins	≈ 9600	≈ 7200	≈ 8300
Influential bins	17.1 %	14.8 %	17.5 %
Influential az. [°]	$10 - 40$	$10 - 40$	$250 - 270$
	$330 - 360$	$220 - 240$	$290 - 340$

In the case of the XRAD, it has been estimated that the sensitivity of ρ in the neighbourhood of the maximum rounds $\mathrm{d}\rho/\mathrm{d}(\delta_\phi) \approx 0.1\mathrm{deg}^{-1}$ for azimuth biases and $\mathrm{d}\rho/\mathrm{d}(\delta_\theta) \approx 0.3\mathrm{deg}^{-1}$ for elevation biases. These sensitivities combined with the standard deviation of the maximum correlation coefficient (see Table 6.4) indicate that the minimum precision (understood here as the maximum day-to-day variability) of the GC results is around ±0.1° in azimuth and ±0.03° in elevation for the CDV and the PDA radars and around ±0.3° in azimuth and ±0.1° in elevation for the LMI radar.

Based on Equation 6.2, relevant quantities for the calculation of significant correlation coefficients are: the number of points/bins considered and the variance of their reflectivities. These quantities, given for the XRAD radars in Table 6.4, indicate that the minimum ρ required for a significant correlation is higher for the LMI radar than for the PDA and the CDV. In addition, the two bracketed factors in Equation 6.2 are the standard scores of the observed and simulated clutter bins, indicating that bins with a reflectivity with a large deviation with respect to the mean value constitute influential points and have the potential to resolve the value of ρ. Polar maps of the standard score of the observed clutter fields at an elevation of 0.6° are displayed in Figure 6.8 for the three XRAD radars. Among these standard score fields, influential bins have been identified as those with a reflectivity value beyond the $\pm 1.5\sigma$ interval around the expected value.

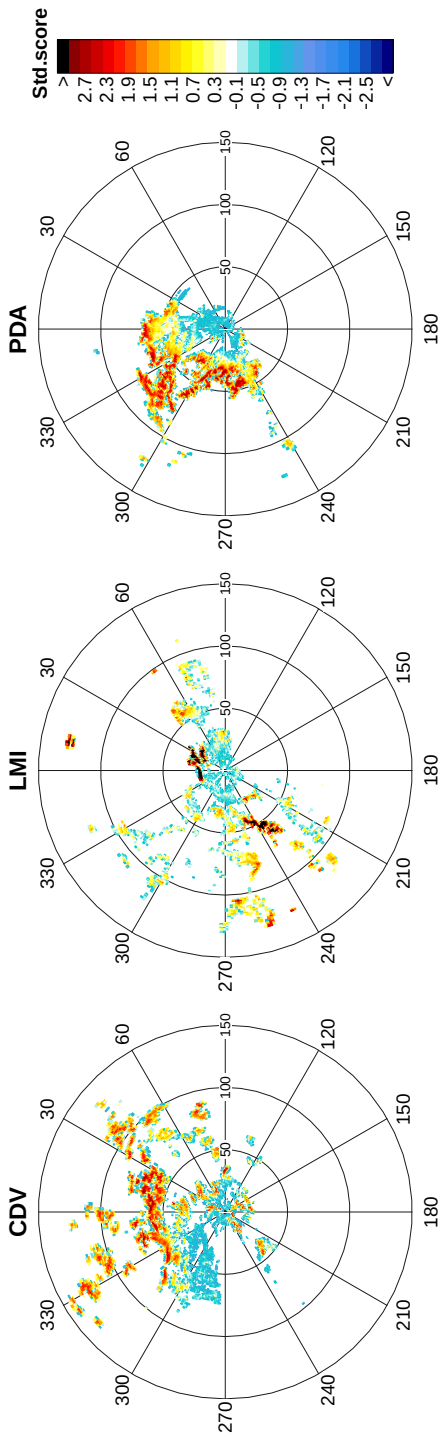

Figure 6.8: Polar maps of standard scores computed from the average ground clutter reflectivity field measured during 7 days with clear air and standard atmospheric propagation conditions in March 2014 at 0.6° elevation for CDV (left), LMI (centre) and PDA (right) radars. Radial grid units are degrees from North and circular grid units are kilometres from radar site.

As shown in Figure 6.9, in the case of the LMI radar, few influential bins with large standard scores determine the value of the correlation coefficient. Variability in the observed reflectivity of these bins has a large effect upon the precision and small inaccuracies in the simulation of their reflectivities may bias the method results. These considerations may explain the difference found in Table 6.2 for the GC elevation bias estimates compared to the SI and SC method estimates.

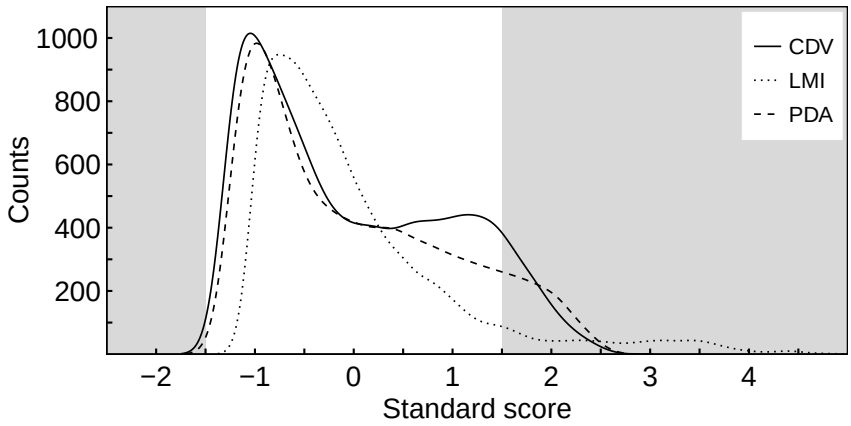

Figure 6.9: Histograms of standard scores computed from the bin fields in Figure 6.8 for the CDV (solid line), the LMI (dotted line) and the PDA (dashed line) radars. Grey areas indicate the regions where influential bins are selected.

In the case of the CDV and the PDA radars, influential clutter bins are confined to particular azimuth regions. The biases estimated by the GC method are those corresponding to the azimuth regions in which the influential bins are clustered. Influential azimuth ranges for the XRAD radars have been recognised as those with the largest number of influential bins and are specified in Table 6.4. Identification of these azimuth regions is relevant for the interpretation of the GC results, in particular if a pedestal levelling error is present. In this regard, the elevation bias of 0° reported by the GC method for CDV radar (Table 6.2) coincides with the bias expected from Figure 6.7 when measuring, at low antenna elevations, in the azimuth sector from 330° to 40° if the levelling error detected is taken into account. Similarly, for the PDA radar, the GC method elevation bias of 0.2° is close to the biases predicted by the levelling error models in Figure 6.7 at azimuthal positions between 250° and 340°.

6.4.3 Analysis by antenna elevation

The analysis as a function of the antenna azimuthal position presented in Subsection 6.4.1 has pointed to the existence of a systematic difference between the elevation offsets measured by SI and SC methods for the CDV radar. As an example, Figure 6.10 shows, for all three radars considered, a comparison of the elevation biases measured through the SI method versus those measured through the SC method. The data-points correspond to measurements for which the azimuthal position of the antenna coincided for both methods (within ±5°). This comparison confirms that a significative difference between the SI and SC elevation biases is present both for the CDV and the LMI radars.

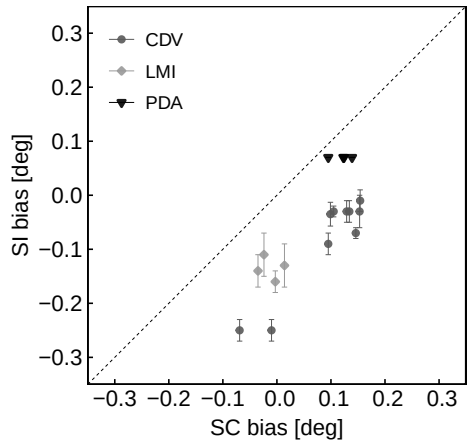

Figure 6.10: Comparison of elevation pointing biases estimated for the XRAD radars by SI and SC methods at coincident azimuthal positions of the antenna: the CDV (dots), the LMI (diamonds) and the PDA (triangles). Bars indicate the uncertainties of the estimates derived from the fit in the SI method.

Considering that SI and SC measurements were collected at very different antenna elevation positions (Table 6.1), the dependence of the estimates as a function of antenna elevation (θ) has been examined as the possible reason for the observed differences. A variation of the measured elevation pointing bias dependent on the antenna elevation may be indicative of nonlinearities in the angle conversion by the elevation resolver device (Chandrasekar et al., 2014). In the case of SC method biases, each of which correspond to a fixed elevation measurement, derivation of the dependence is straightforward. However, SI biases result from the information provided by solar interferences detected at elevations between 0.6° and 8.0°. There-

fore, the solar data has been reanalysed, splitting the interferences first into East and West and then into the different antenna elevations programmed in the scanning task (see Chapter 3, Section 3.2). To keep the number of interferences above 20 for each of the sets, the SI method has been applied to observations collected within 10-day moving windows. Also, to avoid any inaccuracies in the estimates resulting from solar flux variations throughout these 10-day periods, the power of the solar observations has been normalised prior to the fit, scaling it by the detected peak solar power derived from the corresponding daily SI fit (without East-West splitting).

To extract the azimuth dependence of the biases in the cases of the CDV and the PDA radars, the sinusoidal term in Equation 6.1 has been subtracted from the SI and SC estimates (δ_θ) using the inclination (β_0) and direction (ϕ_0) angle values derived in the levelling error model fit (Table 6.3). This assumes that only the constant offset term ($\delta_{\theta,0}(\theta)$) presents a dependence on elevation.

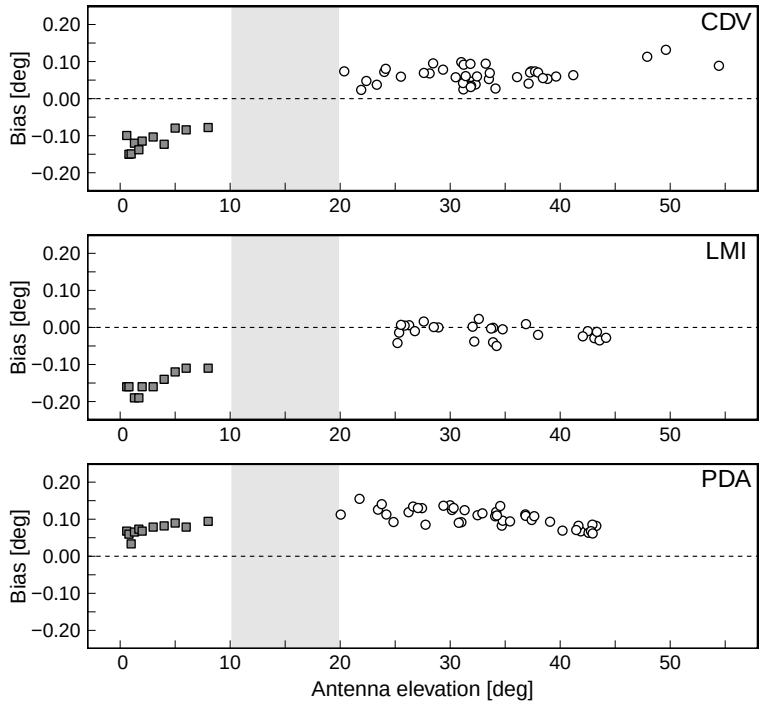

Figure 6.11: Elevation pointing biases estimated for the CDV (top), the LMI (middle) and the PDA (bottom) radars as a function of the elevation position of the antenna. Both SC (white circles) and SI (grey squares) method estimates are shown. The shadowed area indicates the antenna elevation range for which measurements are not available in the case of SI method nor were routinely carried out in the case of SC method.

Figure 6.11 displays the resulting elevation pointing biases as a function of antenna elevation: SI method estimates at low elevations and SC method estimates at high elevations. Given the large amount of data available from SI method, the median value of the estimated biases is displayed at each elevation. Despite the elevation region for which no SC measurements were carried out, in all cases the values of the biases at low elevations show a continuity at high elevations. The biases at low elevations trace an increasing trend with elevation (around 0.01° per degree elevation) for the three radars. In the case of the CDV radar, the increasing trend is also perceptible at high elevations at a lower rate (around 0.005° per degree elevation). For all cases, the results appear in agreement with the discrepancy between the offsets found between SI and SC methods. Even in the case of PDA, the increasing trend at low elevations is compensated by a decreasing trend at high elevations, which explains the absence of a significant difference between SI and SC estimates.

As observed in Figure 6.11 the elevation pointing biases estimated for the CDV and the LMI radars at high antenna elevations were 0.2° to 0.3° different from those measured at low elevations. These results indicate that adjusting the antenna pointing bias based on SC measurements carried out at high elevations may not be appropriate for meteorological applications, in which the lowest elevations are often the relevant ones.

6.5 Conclusions

In the present chapter, three existing methods for antenna pointing monitoring have been reviewed and comparatively studied. The first method (GC) uses daily observed ground clutter returns as reference. The other methods use the known location of the Sun as reference: the first (SC) is based on an offline Sun scan while the second (SI) uses solar interferences detected in operational radar scans.

GC and SI methods are online-run and do not require the interruption of the radar operation. However, the accuracy of the GC method may be compromised by precipitation or anomalous atmospheric propagation conditions. Conversely, the precision of the SI estimates depends on the quality and number of the collected solar observations. Indeed, in the case of the SI method, the number of observations can be increased by considering interferences collected in several consecutive days. Both methods estimate the antenna pointing biases at low elevations, which are the most relevant in the georeferenciation and quantification of precipitation. In

turn, SC method is offline-run, providing only isolated bias estimates. However, if measurements are taken on clear-air days and at high elevations, as in the presented cases, the results are assumed unaffected by atmospheric conditions.

Daily SC measurements carried out for three XRAD radars during a one-month campaign have made possible a direct comparison of the pointing biases estimated by the methods. The results of this short term analysis have shown that the day-to-day variability of the bias estimates by the Sun-based methods, SI and SC, is below 0.02°. Nonetheless and particularly for the azimuth biases, this precision decreases if the radar sensitivity is close to the peak solar signal level. A remarkably large day-to-day variability in the SC azimuth offset estimates has proven to be indicative of azimuthal backlash, consequence of the degradation of a mechanical component. In the case of the GC method, the angular resolution of the PPI clutter fields due to sample averaging may compromise the accuracy of the azimuth pointing offsets.

A one-year long-term analysis of the performance of the methods has pointed out the importance of accounting for the antenna position at the time of the measurement when interpreting the reported pointing biases. For SI method, East/West splitting of the solar observations and reanalysis of the data has allowed to examine the elevation biases as a function of the azimuthal position of the antenna and a characteristic dependence has been found, associated with an inclination of the antenna rotation plane with respect to the horizontal plane and attributed to a structural levelling error. Elevation biases reported by SC method throughout the long-term period have shown an azimuthal dependence in agreement, confirming the levelling error. After subtracting the azimuthal dependence, it has been shown that pointing offset estimates may also present a dependence upon the antenna elevation position. The presence of such a dependence, likely related to a nonlinearity in the resolver angle conversion, even if not very pronounced, may introduce a significant difference between the biases estimated by SI and SC methods if the measurements of SC method are performed at high antenna elevations.

For GC method, the effect of the ground clutter azimuthal distribution has been investigated and for each radar the clutter bins influencing the bias estimates have been defined. For radars with few clutter bins the correlations computed tend to be less significant and isolated strong clutter structures may bias the pointing offset estimates and decrease their precision. Two cases of radars for which the influential bins are confined to vast but limited azimuth regions have also been presented. It has been found that at these influential azimuth regions the GC elevation biases are in accordance with those found for SC and SI method when the pedestal levelling error is taken into account.

Overall, the results demonstrate the ability of all three methods to detect severe antenna misalignments on short-term. However, for remote and accurate quantification of both the pointing offsets and monitoring of system levelling status, a long-term, synergistic application of the Sun-based procedures is suggested. Although the proposed methodology requires of further validation, the present study has shown that such a combined application may provide pointing bias estimates in an expanded range of azimuth and elevation antenna positions. The range of azimuthal positions of the antenna accessible by SI measurements during a one-year period depends on the latitudinal location of the radar and on the maximum scan elevation (Frech, 2009), attending to the local annual solar motion. For most cases, the pointing biases are not measurable through SI method for both a northerly and a southerly region of azimuthal positions. However, the gap at southerly azimuths can be partially covered by long-term SC measurements programmed in advance. The analysis of SI and SC elevation pointing biases as a function of antenna azimuthal position would serve to separate the levelling error from the systematic alignment offset, if present. In addition, comparison and/or analysis of SI and SC systematic elevation offsets would allow to detect and estimate differences between the methods related to a dependence upon the antenna elevation position, providing a means for appropriate calibration of the antenna alignment at the chosen elevation.

7

Quality of Doppler velocity: dual-PRF outlier correction

* The present chapter has been adapted from: Altube, P., J. Bech, O. Argemí, T. Rigo, N. Pineda, S. Collis and J. Helmus, 2016: Correction of dual-PRF Doppler velocity outliers in the presence of aliasing. *J. Atmos. Oceanic Technol.*, under review.

High-quality Doppler weather radar velocity data are essential for automated, real-time, severe weather detection algorithms (Stumpf et al., 1998; Mitchell et al.,

1998; Smith et al., 2004), for assimilation in numerical weather prediction models and nowcasting systems (Sun and Crook, 2001; Stensrud et al., 2009; Pierce et al., 2012) or for building climatologies from archived radar data as described in Bellon and Zawadzki (2003), Miller et al. (2013) or Wapler et al. (2016), where multi-year datasets are used to derive specific statistics of the characteristics of thunderstorm mesocyclones. In this regard, quality improvement of the Doppler data provided by the XRAD is essential for building climatologies of this kind for the Catalonia region, where a high tornadic activity is attributed in several studies available in the literature, as well as *ad hoc* from climatologies built from direct observations or from the damage in the surface (Homar et al., 2003; Mateo et al., 2009; Aran et al., 2009; Bech et al., 2009, 2011; Gayà et al., 2011; Soriano Romero et al., 2015).

Pulsed Doppler radars estimate the radial velocity of the scattering targets (v) based on the phase shift between consecutive backscattered pulses. The maximum measurable phase shift between pulses is $\pm\pi$ radians, which poses a limit to the maximum radial velocity that the radar can unambiguously measure. This is known as the Nyquist velocity or aliasing velocity, V_a:

$$V_a = \frac{\lambda\,\mathrm{PRF}}{4}\,, \tag{7.1}$$

where λ is the wavelength of the radar and PRF is the Pulse Repetition Frequency (PRF).

If scatterers move faster than V_a, aliasing occurs, that is, the signal frequency is misidentified and the estimated velocity is given folded back within the $\pm V_a$ interval, differing from the actual velocity in an integer number of $2V_a$ (Doviak and Zrnič, 1984). The correction of aliased Doppler velocities has been historically in the focus of a large number of post-processing algorithms. For instance, widely known dealiasing techniques apply local statistics (Ray and Ziegler, 1977; Miller et al., 1986), rely on the local and/or temporal continuity of the velocity field (Eilts and Smith, 1990; James and Houze, 2001), incorporate global variational methods (Jing and Wiener, 1992) or constitute region-segmentation algorithms (Bergen and Albers, 1988, and references therein). Other common techniques use variational methods locally to estimate the underlying wind field to be used as reference for dealiasing (Gong and Wang, 2003; Haase and Landelius, 2004; Xu et al., 2010). The drawback in the application of dealiasing algorithms is that, often, the assumptions about the underlying wind field are not met or complementary data are required (e.g. a quality map, a valid starting point or wind field observations or simulations).

An alternative to dealiasing post-processing techniques is to minimise the alia-

sing by extending the unambiguous velocity V_a at the processing level. For a fixed radar wavelength, the Nyquist velocity could be straightforwardly extended by increasing the PRF. However, the choice of the PRF involves a trade-off between the maximum unambiguous range measurable by the radar, $R_{\max}$, and the Nyquist velocity:

$$V_a \, R_{\max} = \frac{c\lambda}{8} \, . \tag{7.2}$$

Scanning/processing schemes have been proposed that allow to independently choose the unambiguous range and velocity (Lehtinen, 2001; Pirtillä et al., 2005). However, in these techniques, the estimation of spectral moments requires the application of statistical inversion procedures. Therefore, commonly applied strategies tackle the range and velocity ambiguity limitations separately. For instance, range ambiguities can be mitigated using phase-coding schemes to assign overlaid echoes to the correct range (Sachidananda and Zrnić, 1999; Frush et al., 2002). Conversely, extension of the Nyquist velocity for a fixed $R_{\max}$ can be achieved by processing pulses at multiple PRFs, conventionally through the implementation of either staggered multiple-PRT (Pulse Repetition Time) techniques (Sirmans et al., 1976; Torres et al., 2004; Cho, 2005; Tabary et al., 2006) or the batch-mode dual-PRF technique (Dazhang et al., 1984).

In the staggered dual-PRT technique, the time between two consecutive pulses is varied yielding two velocity estimates for each atmospheric resolution volume. These velocity estimates are further processed to dealias the velocity within an extended Nyquist interval. This procedure is extended in the triple-PRT technique, in which three PRTs are interlaced with an increased potential to extend the unambiguous velocity with improved dealiasing success (Tabary et al., 2006). However, the nonuniform sampling applied in the staggered-PRT techniques hampers the spectral processing involved in traditional clutter-filtering algorithms (Banjanin and Zrnić, 1991; Sachidananda and Zrnić, 2000). Consequently, the batch-mode dual-PRF technique has often been chosen for operational use over the staggered schemes and is commonly available in commercial weather radar processors.

In the dual-PRF technique, contiguous atmospheric volumes are probed at two different PRFs and the two resulting velocity measurements are further processed to dealias the velocity within an extended Nyquist interval. The unfolding procedure assumes that the two measurements correspond to the same velocity but, in practice, this assumption may be violated by factors such as the presence of high azimuthal shear or due to the uncertainty of the measurements, which lead to an increased dealiasing failure and result in the unfolding errors or outliers characteristic

of the dual-PRF radial velocity images (Jorgensen et al., 2000; May, 2001).

In the present chapter, a novel post-processing algorithm for identification and correction of dual-PRF outliers is presented. The methodology uses circular (or directional) statistics (Fisher, 1993) applied in a spatial image filtering procedure and can be employed without prior application of post-processing dealiasing algorithms, in contrast to existing dual-PRF correction techniques (Joe and May, 2003; Holleman and Beekhuis, 2003). This is of particular importance because some of the dealiasing techniques may erroneously correct dual-PRF outliers (see Bergen and Albers, 1988; Haase and Landelius, 2004, for instance). Therefore, this characteristic offers increased flexibility for the design of Doppler velocity quality control procedures. In this study, the performance of the proposed algorithm under simulated and actual measurement conditions is evaluated in comparison with two existing weather radar dual-PRF correction techniques, in order to prove its increased correction potential and discover its limitations. The ability of the methodology to improve the quality of real dual-PRF data is exemplified through the application to velocity images corresponding to three severe weather events.

7.1 Dual-PRF technique

The batch-mode dual-PRF scanning technique consists on sending a pulse train at a fixed PRF followed by another pulse train with a different PRF (Dazhang et al., 1984). In the considerations henceforth it is assumed that the ratio of the two PRFs is chosen as a function of an integer dual-PRF factor, N:

$$\frac{\mathrm{PRF}_h}{\mathrm{PRF}_l} = \frac{V_{ah}}{V_{al}} = \frac{N+1}{N}\,, \tag{7.3}$$

where V_{ah} and V_{al} are the Nyquist velocities corresponding to the high and low PRF respectively. Commonly used N factors are 2, 3 or 4 (May, 2001; Jorgensen et al., 2000; Vaisala, 2014b).

With the batch-mode scanning procedure, any two gates (resolution volume units) contiguous in the scanning direction are probed at different PRFs. Therefore, the radial velocities estimated in the two contiguous gates, v_h and v_l, are given within the two different $\pm V_{ah}$ and $\pm V_{al}$ Nyquist intervals. The main assumption of the dual-PRF technique is that the "actual" velocity of the scatterers is the same in both gates. Thereby, the two estimated velocities or phase shifts can be considered together in order to estimate the dual-PRF velocity (v_e) as (*cf.* Doviak and Zrnič,

1984):

$$v_e = \frac{V_{ae}}{\pi}(\theta_l - \theta_h)_{\min} , \tag{7.4}$$

where θ_l and θ_h are the phase shifts estimated at low and high PRF respectively and the *min* subindex indicates that the smallest angular difference is considered.

This dual-PRF velocity estimate v_e is given within an extended Nyquist interval, $\pm V_{ae}$, such that (*cf.* Dazhang et al., 1984; Torres et al., 2004):

$$V_{ae} = N\,V_{ah} = (N+1)V_{al} . \tag{7.5}$$

The error of v_e computed in Equation 7.4 is amplified by the propagation of the errors of the two estimated phases (Jorgensen et al., 2000; Holleman and Beekhuis, 2003; Torres et al., 2004). In practice, Equation 7.4 is only used to determine the number of folds, n_h or n_l, that the originally estimated velocity, v_h or v_l, has undergone within its corresponding Nyquist interval, V_{ah} or V_{al}. Then, v_e is improved applying the obtained number of folds, so that the error of the final v_e is only that of the originally estimated velocity:

$$v_e^{(h/l)} = v_{h/l} + 2n_{h/l}V_{ah/l} . \tag{7.6}$$

The dual-PRF velocity will, in most of the cases, be correctly unfolded, $v_e = v_{e,\mathrm{cor}}$, but for certain gates it may also be incorrectly unfolded (Jorgensen et al., 2000), constituting a dual-PRF unfolding error or outlier, $v_e = v_{e,\mathrm{out}}$.

Dual-PRF unfolding errors

Following Joe and May (2003), dual-PRF unfolding errors occur if the main assumption of the dual-PRF technique is violated, in particular when the difference between the *true* velocities of adjacent gates exceeds a certain $\Delta v_{\max}$ threshold:

$$|v_i - v_{i-1}| > \frac{V_{ae}}{N(N+1)} \equiv \Delta v_{\max} . \tag{7.7}$$

If this inequality is fulfilled, the v_e estimate in Equation 7.4 will be biased, yielding an incorrect unfolding factor $n_{h/l}$ for application of Equation 7.6. Consequently, the velocity estimate for the corresponding outlier gate, $v_{e,\mathrm{out}}$, will be biased from the correctly unfolded velocity $v_{e,\mathrm{cor}}$ by an integer number $m_{h/l}$ of high

or low Nyquist intervals:

$$v_{e,\mathrm{out}}^{(h)} = v_{e,\mathrm{cor}} + 2m_h V_{ah}$$
$$v_{e,\mathrm{out}}^{(l)} = v_{e,\mathrm{cor}} + 2m_l V_{al}\ . \tag{7.8}$$

Gate-to-gate velocity differences leading to dual-PRF unfolding errors as required by Equation 7.7 arise in regions where the estimated spectral width is large, due to wind shear, turbulence and/or a low quality of the velocity estimates (see Holleman and Beekhuis, 2003, for instance). Consequently, velocity outliers may appear speckle-wise in isolated gates, generally as a result of random errors in the velocity estimates or systematically clustered together in areas of strong shear or turbulence or where the quality of the received signal is low. An example of these characteristic dual-PRF unfolding errors in a real case radial velocity PPI field is shown in Figure 7.1 for the LMI radar.

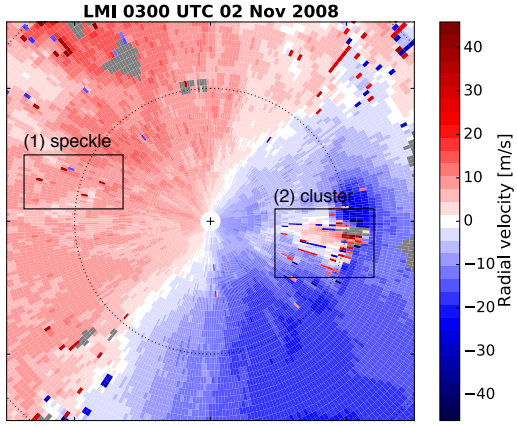

Figure 7.1: Example of a base level (0.6°) PPI scan from LMI radar showing dual-PRF radial velocity at 0300UTC on 2 November 2008. Black rectangles indicate: (1) an area of speckle-like dual-PRF outliers and (2) an area of clustered dual-PRF outliers associated with a highly sheared structure, likely a microburst (Bech et al., 2011). Gates with a non-valid velocity value are filled in grey colour and the dotted range ring indicates a 20 km distance from the radar.

The incidence of the outliers is also conditioned by the value of the threshold in the right hand side of Equation 7.7, i.e. $\Delta v_{\max}$. For a fixed value of the high PRF, which determines the maximum unambiguous range, the choice of the dual-PRF factor N involves a tradeoff between the maximum extension of the Nyquist velocity

in Equation 7.5 and $\Delta v_{\max}$. For instance, the choice of a high N allows for a large extension of the Nyquist velocity V_{ae} but increases the probability of getting dual-PRF unfolding errors due to a lower $\Delta v_{\max}$. It is therefore a relevant requirement that a dual-PRF outlier correction procedure performs efficiently in the presence of a high number of outliers while allowing the application of a complementary procedure that corrects aliasing within $\pm V_{ae}$ interval (hereinafter extended Nyquist aliasing, after the terminology employed in WMO, 2008).

7.2 Correction of dual-PRF unfolding errors

In this section a new post processing technique for correcting dual-PRF unfolding errors is presented. This new technique arises from the analysis of two popular correction techniques proposed in the literature.

7.2.1 Existing post-processing techniques

The two existing dual-PRF correction techniques studied rely on the continuity of the velocity field and use statistical image processing methods to identify dual-PRF unfolding errors, attending to their outlier characteristics. More precisely, a gate-by-gate analysis of the radial velocity image identifies outlying gates by comparison of their velocity with a reference statistic calculated for the gates in their neighbourhood: either the mean velocity (Joe and May, 2003) or the median velocity (Holleman and Beekhuis, 2003; Cho, 2005). Henceforth, these two techniques will be referred to as *mean* and *median* techniques. It must be noted that because in these two techniques the statistics are calculated for the velocity, if extended Nyquist aliasing is present, gates in or close to the edges of the aliased area may present a significative velocity deviation with respect to the mean or median velocity of the surrounding gates. These gates will then be incorrectly identified as dual-PRF outliers. Therefore, an extended dealiasing algorithm needs to be applied prior to these dual-PRF correction techniques, as pointed out in Holleman and Beekhuis (2003).

The correction of the identified outliers consists on trying all possible unfolding factors (m integer in Eq. 7.8) to determine the one that yields the minimum deviation from the mean or median velocity in the neighbourhood. When the PRF at which the outlying gate has been scanned is unknown, all possible unfolding factors for the low and high PRFs need to be tried (Joe and May, 2003). In turn, when the PRF of the target gate is known, this procedure is faster and more robust. How-

ever, as described in Holleman and Beekhuis (2003), as long as dual-PRF outliers are present it is possible to perform a statistical analysis of the velocity estimates to determine in advance which PRF corresponds to each radial.

7.2.2 New post-processing technique

The new correction procedure proposed is a post-processing technique that, as the techniques described above, uses local statistics to identify dual-PRF unfolding errors. However, the statistics applied in this case are circular and work on the phase space instead of the velocity space. In particular, the reference velocity for identification of the outliers is derived from the mean phase in the neighbourhood. This mean phase is calculated circularly, that is, considering only the minimum angular differences between the phases of the surrounding gates, without giving preference to any rotation direction. Thereby, the methodology is less sensitive to the presence of neighbouring outliers and can be applied in the presence of extended aliasing. As detailed in the following, the proposed technique (*cmean* method henceforth) treats outlier identification and correction separately in two differentiated stages.

New technique: identification

The dual-PRF velocities v_e can be expressed as phases in a circle of radius V_{ae}/π. The phase α_{cor} calculated for a gate with a velocity that has been correctly unfolded in the dual-PRF procedure, $v_e = v_{e,\text{cor}}$, is given by:

$$\alpha_{\text{cor}} = \pi \frac{v_{e,\text{cor}}}{V_{ae}} \,. \tag{7.9}$$

On the other hand, according to Equation 7.5 and Equation 7.8 and from Equation 7.9, the phases α_{out} calculated for gates that correspond to dual-PRF outliers, $v_e = v_{e,\text{out}}$, will differ from the correct phase α_{cor} by:

$$\alpha_{\text{out}}^{(h)} = \alpha_{\text{cor}} + 2\pi \frac{m_h}{N} \,, \tag{7.10}$$

if the gate has been scanned at the high PRF, and by:

$$\alpha_{\text{out}}^{(l)} = \alpha_{\text{cor}} + 2\pi \frac{m_l}{(N+1)} \,, \tag{7.11}$$

if the gate has been scanned at the low PRF.

Now, if all phases are scaled multiplying them by either N or $(N+1)$ depending on the scanning PRF, the second term in the right hand side of Equation 7.10 and Equation 7.11 will result in an integer factor of 2π. In this way, the circular mean calculated for the scaled phases will not be biased by the presence of dual-PRF outliers in the immediate neighbourhood. Also, since the phases are expressed in a circle of $2V_{ae}$ circumference, the circular mean calculated around gates in or close to the edges of an area of extended Nyquist aliasing will not be biased either and hence will not be erroneously identified as dual-PRF outliers.

Based on these ideas, the proposed dual-PRF identification stage is summarised in the following steps, which are sketched in Figure 7.2:

1. Convert dual-PRF velocities v_e to phases α through multiplication by (π/V_{ae}).

2. Multiply the α phases by N or $(N+1)$, depending on the scanning PRF, to obtain the scaled phases α' .

3. Compute the circular average of the scaled phases in a 5x5 window around each of the gates, separately for low PRF and high PRF neighbouring gates within the 5x5 window:

$$\beta_{h/l} = \text{atan2}\left(\frac{1}{M_{h/l}} \sum_{j=0}^{M_{h/l}} \sin \alpha_j'^{(h/l)} \, , \, \frac{1}{M_{h/l}} \sum_{j=0}^{M_{h/l}} \cos \alpha_j'^{(h/l)} \right) , \tag{7.12}$$

   where the atan2 function is the two argument arc-tangent function that considers the sign of the two arguments in order to compute the arc angle in the appropriate quadrant. The index j runs for all high or low PRF gates within the 5x5 window, M_h or M_l. The maximum number of high and low PRF gates within the 5x5 window will either be 10 or 14, depending on the PRF of the target gate. This step yields two average phases for each gate, β_l and β_h, which constitute estimators of $(N+1)\alpha_{\text{cor}}$ and $N\alpha_{\text{cor}}$ respectively, given in the base phase interval $[-\pi, \pi]$.

4. Estimate the reference phase α_{ref} from:

$$\alpha_{\text{ref}} = \begin{cases} (\beta_l - \beta_h), & \text{if } (\beta_l - \beta_h) \geq 0 \\ (\beta_l - \beta_h) + 2\pi, & \text{otherwise} \end{cases} \tag{7.13}$$

5. Calculate the minimum angular difference between the dual-PRF phase and

the reference phase for each gate: $(\alpha - \alpha_{\text{ref}})_{\min}$ and convert this phase difference to a velocity difference through multiplication by (V_{ae}/π).

6. Identify outlying gates as those with a velocity difference greater than their corresponding Nyquist velocity (V_{al} or V_{ah}).

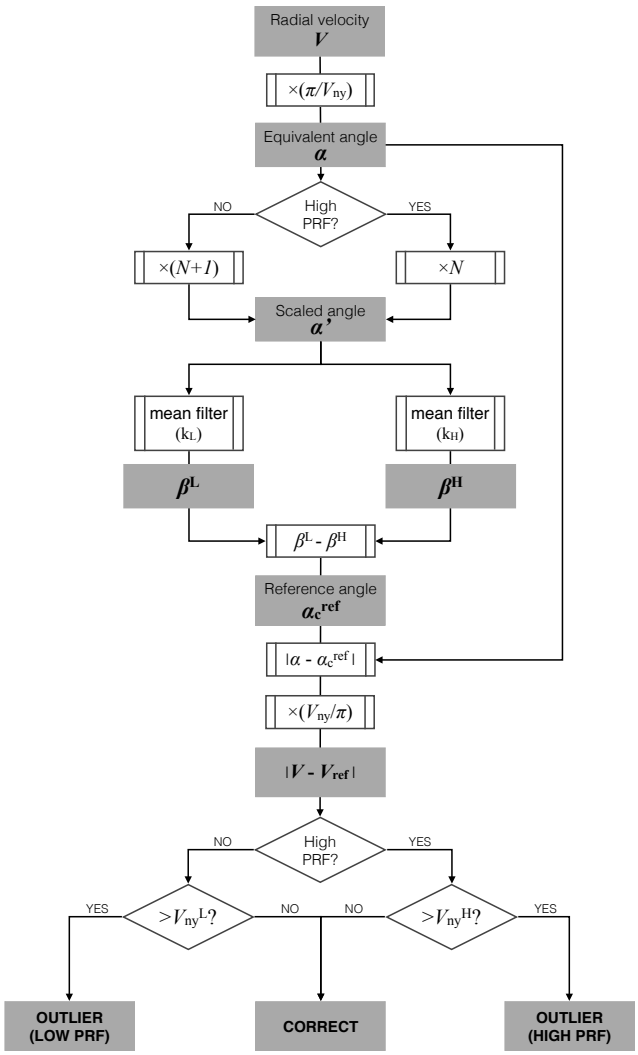

Figure 7.2: Flowchart description of the proposed dual-PRF velocity outlier identification procedure using circular statistics.

The 5x5 size of the filter window is chosen so that a sensible number of both high-PRF and low-PRF estimates are available for calculation of the corresponding circular averages. In addition, it is required that at least 2 of both high-PRF and low-PRF gates within the window contain a non missing velocity value. It is important to note that steps 2 and 4 above require that the PRF ratio fulfils Equation 7.3. However, the procedure can be straightforwardly generalised for PRF ratios such that $\mathrm{PRF}_h/\mathrm{PRF}_l = (N+d)/N$, where d is an odd integer. If d were an even integer, the condition in step 4 would not be sufficient to unambiguously determine the reference phase and would require additional constraints.

New technique: correction

Once potential dual-PRF outliers have been identified, this next stage corrects them using a procedure similar to that of the *median* method. The local median velocity in a 5x5 window around the outlier gate is calculated and the deviation of the target gate velocity from this reference is computed for all possible correction factors. The values of the possible correction factors are determined by the dual-PRF factor N and are conditioned by whether the outlier gate has been scanned at high or low PRF (see Joe and May, 2003, for an example with $N = 3$). The correction factor $m_{h/l}$ finally applied in Equation 7.8 is the one which yields the minimum velocity difference. In addition, the following points must be verified:

- Gates that have been labelled as outliers in the identification process are excluded from the calculation of the median.
- Only gates that have been labelled as outliers in the identification process are corrected.
- Only identified outliers that have at least 2 valid neighbours are corrected.

The first and last requirements have an effect on the number of valid gates available for the calculation, especially when the outliers appear clustered or close to missing value regions, but minimise the probability of an erroneous correction.

7.3 Simulation of dual-PRF velocity fields

Following Brown and Wood (2007), radial velocity fields have been simulated based on analytical functions representing vertical profiles of a horizontally homogeneous wind field. From these radial velocity fields post-processed artificial dual-PRF fields

have been computed, which have served as reference for analysing the outlier correction ability of the three techniques under study (the existing *mean* and *median* and the proposed *cmean*). Figure 7.3 displays the speed and direction profiles of the first horizontal wind field used in the study. Simulations for a C-band radar of 5 cm wavelength have been generated, performing PPI scans at five different elevations: 0°, 1°, 2°, 3° and 4°. The simulations for the profile shown in Figure 7.3 are free of extended aliasing and make up the dual-PRF reference volume for the statistical quantification of the outlier correction performance.

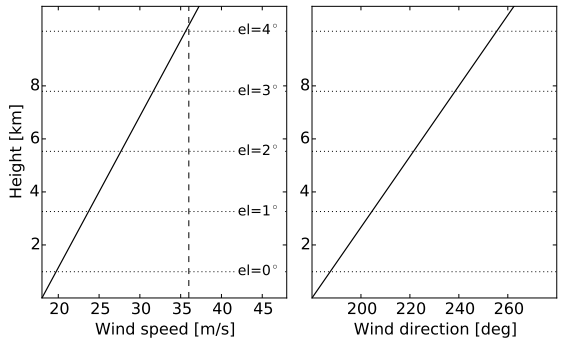

Figure 7.3: Wind speed (left panel) and direction (right panel) vertical profiles of the wind field used for the simulation of dual-PRF Doppler velocity volumes. Dotted horizontal lines indicate the maximum height of the radar beam axis for the simulated PPI elevations. The dashed vertical line indicates the extended Nyquist velocity V_{ae} =36 m s^{-1}.

In the simulation process, the beamwidth of the radar is assumed negligible and the three wind vector components (u, v and $w = 0$) for each point of the simulation grid are computed from the corresponding height in the wind profile. The PPI simulation grid has a resolution of 1 km in range and 1° in azimuth and the minimum and maximum ranges are 2 km and 130 km, respectively. After extracting the radial velocity component from the wind vectors, Gaussian random noise with fixed standard deviation has been added to each radial velocity value. In this way, a series of volumes corresponding to radial velocities with standard deviations that range from 0.1 m s^{-1} to 3.0 m s^{-1} in 0.1 m s^{-1} steps has been generated. For each radial velocity PPI field in each of the volumes, two fields of interest are computed:

1) The *reference* single-PRF velocity field computed by folding the velocities into a Nyquist interval of ±36 m s^{-1}.

2) The dual-PRF radial velocity field computed by folding the velocities in alter-

nate radials into Nyquist intervals of $\pm 12\,\mathrm{m\,s^{-1}}$ (V_{ah}) and $\pm 9\,\mathrm{m\,s^{-1}}$ (V_{al}), corresponding to a dual-PRF factor $N = 3$. The resulting velocities are unfolded within the extended Nyquist interval of $36\,\mathrm{m\,s^{-1}}$ (V_{ae}) using the dual-PRF technique (Section 7.1).

Analogously, a 4° elevation *reference* single-PRF velocity field and the corresponding dual-PRF field have been generated from the second wind profile shown in Figure 7.4. In this second case, the resulting simulated fields present extended aliasing and have been used to qualitatively analyse the performance of the correction techniques in the edges of the aliased regions. In this case, the field is only simulated once, adding a Gaussian random noise of $1\,\mathrm{m\,s^{-1}}$ standard deviation.

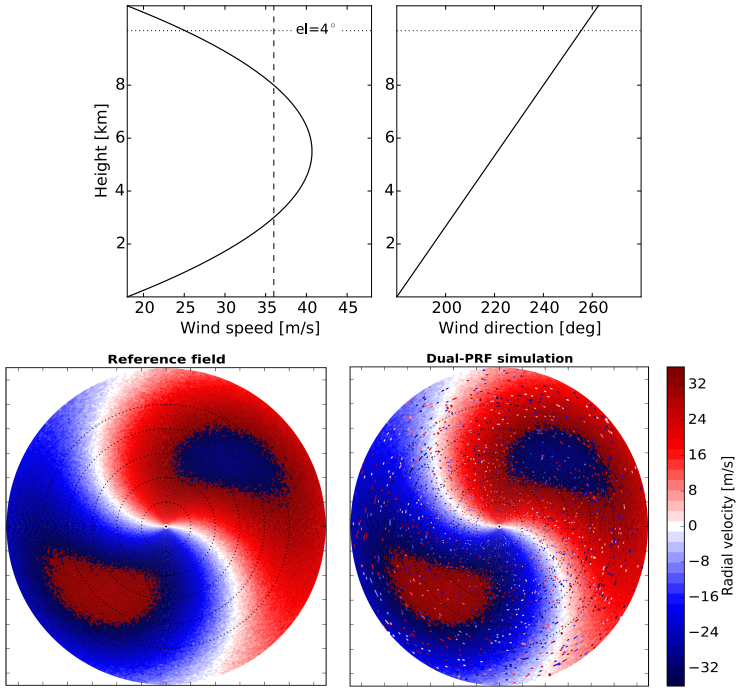

Figure 7.4: (Top panels) As Figure 7.3 but for a simulated Doppler velocity field which presents extended Nyquist aliasing. (Bottom panels) Reference radial velocity field and dual-PRF velocity field simulated at an elevation of 4° for the wind field profiles drawn in the top panels. The dual-PRF field has been generated using a dual-PRF factor of $N = 3$ and an extended Nyquist velocity of $36\,\mathrm{m\,s^{-1}}$. Dotted range rings drawn in the radial velocity fields indicate 20 km intervals.

7.4 Analysis of correction techniques

The characteristics of the statistics used by each of the three dual-PRF outlier correction techniques can be qualitatively investigated from the distributions of the local velocity deviation in each case. The distributions of the local velocity deviations have been constructed calculating the velocity deviation for each of the gates in the simulated dual-PRF velocity volumes described in Section 7.3 above. The velocity deviation is the difference between the velocity of the target gate and a reference velocity that is computed differently depending on the correction technique. For the *median* and *mean* methods, the local reference velocity has been calculated as either the median or the mean velocity of the gates with a non-missing velocity value in a 3x3 window around the target gate. In the case of the *median* method, the central target gate has also been included in the calculation, as in Holleman and Beekhuis (2003). For the *cmean* method, the velocity deviations have been calculated following the steps described in Subsection 7.2.2.

Figure 7.5 displays the distributions of the local velocity deviations for the three correction techniques. In all cases the velocity difference has been scaled by the Nyquist interval corresponding to the target gate; $2V_{ah}$ if the gate has been scanned at the high PRF or $2V_{al}$ if the gate has been scanned at the low PRF. In this way, the scaled velocity difference is an indicator of by how many Nyquist intervals the dual-PRF velocity is in error.

As observed in the top panel of Figure 7.5, when the median velocity is used as reference for calculation of the deviation, dual-PRF outliers are clearly identified as those with a deviation greater than the corresponding V_{ah} or V_{al} (dashed vertical lines). The median is a reliable estimator of the reference velocity when the percentage of outliers in the sample drawn from the neighbourhood is below the accepted breakpoint of 50 % (Hampel et al., 1986). Consequently, in the identification process a few outliers may be missed and correctly unfolded gates may be erroneously identified as outliers if the number of outlier neighbours is higher than 50 %. However, the deviation histogram presents well defined peaks of limited width at integer multiples of the corresponding Nyquist interval and, therefore, correctly identified outliers can be accurately corrected based on the median reference velocity.

On the other hand, and as indicated by the results presented in the central panel of Figure 7.5, the presence of outliers in the neighbourhood has a significative biasing effect in the reference mean velocity. When the standard deviation of the

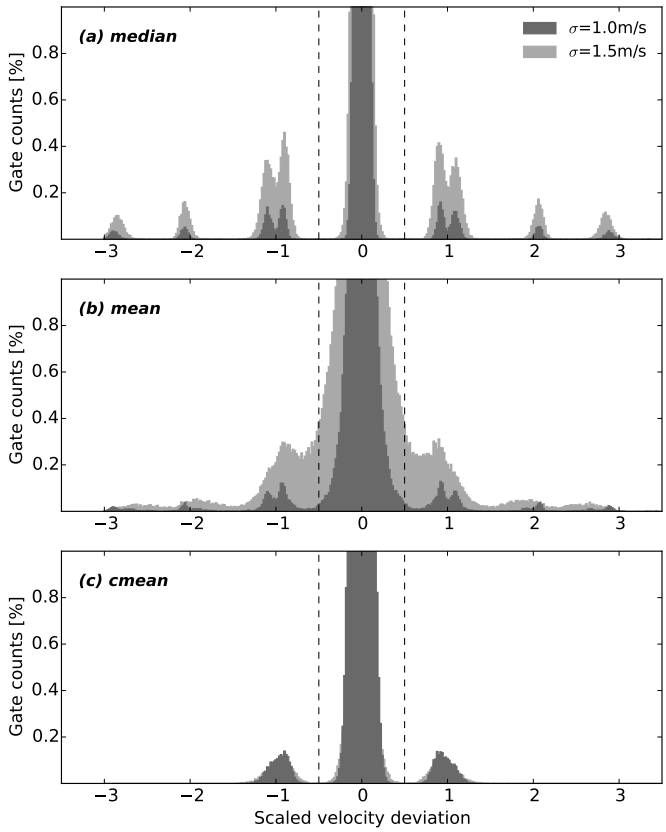

Figure 7.5: Histograms of the velocity deviation of each gate from the: (top panel) local median velocity (middle panel) local mean velocity and (bottom panel) local circular mean. The velocity deviation is scaled by the Nyquist interval corresponding to the scanning PRF of the gates. The total number of gates considered is 230400, encompassing all gates in the simulated dual-PRF velocity fields at five different elevations (0°, 1°, 2°, 3° and 4°). The dual-PRF factor is $N = 3$ and the extended Nyquist velocity is V_{ae} =36 m s^{-1}. Two cases of radial velocity standard deviation are presented: 1.0 m s^{-1} (dark grey) and 1.5 m s^{-1} (light grey). Vertical dashed bars indicate the minimum deviation thresholds to identify the dual-PRF outliers.

radial velocities increases, the number and concentration of dual-PRF outliers also increases. As a result, the calculated velocity deviations are highly variable and the large spread of the distribution peaks indicates that: (1) misses and false alarms are likely to occur in the identification of outlying gates, specially in the overlapping area for gates with scaled velocity deviations between 0 and ±1 (close to dashed vertical bars) and (2) outlier values may be erroneously corrected for gates whose

scaled deviation does not clearly correspond to a particular integer.

Finally, the distributions for the *cmean* technique in the bottom panel of Figure 7.5 indicate that dual-PRF outliers can be clearly identified as those with a scaled velocity difference beyond the dashed vertical lines. However, the phase difference calculated in the *cmean* procedure (step 5 in Subsection 7.2.2) always lies between $\pm\pi$ and the resulting velocity difference is never greater than $\pm V_{ae}$. Consequently, the scaled velocity difference is never greater than ± 2 (for a factor $N = 3$) and its distribution peaks at ± 1. This implies that the procedure serves to identify the outliers but that the circular mean reference does not give enough information for correction, therefore requiring a correction stage based on velocity statistics instead of phase statistics, as proposed in Figure 7.2.2.

7.5 Quantitative performance analysis

In this section the performance of the new *cmean* dual-PRF outlier correction technique is quantitatively assessed in comparison with the existing *mean* and *median* techniques. The three correction techniques are applied, in two separate analyses, to the simulated dual-PRF velocity volumes and to a collection of real fields scanned at single PRF that have been further aliased to dual-PRF. In the implementation of the *mean* technique, the correction procedure has been modified in analogy to the *cmean* technique; i.e. identified outliers are excluded from the local mean calculations in the correction stage. This 2-stage procedure is similar to the extension of the Joe and May (2003) *mean* method reported in Hengstebeck et al. (2014) and is thought to minimise the erroneous correction of identified outliers pointed out in Section 7.4.

In the present quantitative analysis of the three correction techniques, the location of the outliers in the dual-PRF fields and the corresponding correction factor are known by comparison with the *reference* single-PRF field in each case. This allows to label the gates separately in the identification and correction stages of the dual-PRF outlier correction techniques in order to quantify the quality improvement brought out by the technique. Figure 7.6 schematically depicts the gate labelling, classifying them as: correct negatives (correctly unfolded gates that have been correctly identified as non-outliers), false alarms (correct gates erroneously identified/corrected as outliers), misses (outlier gates not identified/corrected) and hits (outlier gates appropriately identified and corrected). To statistically quantify the performance of the dual-PRF correction methods, the Probability Of Detection

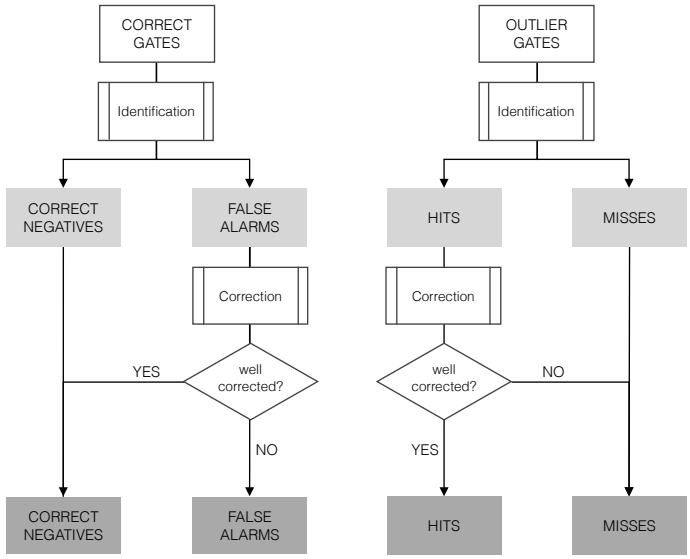

Figure 7.6: Labelling process of the velocity field gates, based on the quality of the dual-PRF outlier identification (light grey labels) and correction (dark grey labels).

(POD) verification index has been used, analogous to effectiveness in the present context, and an Efficiency Index (EI) has been defined:

$$\mathrm{POD} = \frac{\text{hits}}{(\text{hits} + \text{misses})} = \frac{\text{hits}}{\text{outlier gates}}\,, \tag{7.14}$$

$$\mathrm{EI} = \frac{\text{hits} - \text{false alarms}}{(\text{hits} + \text{misses})} = \frac{\text{hits} - \text{false alarms}}{\text{outlier gates}}\,. \tag{7.15}$$

The EI statistic indicates the fraction of outliers efficiently corrected, accounting for the generation of new outliers by the false alarms. The EI may be used in combination with the POD as an alternative indicator of the false alarm rate or Probability of False Detection (POFD) index, which is not an appropriate statistic for the present analysis because the number of false alarms (and also the number of outliers) is in most cases small relative to the number of correct gates.

7.5.1 Dual-PRF fields from simulations

Figure 7.7 displays the results of application of the three correction techniques, *mean*, *median* and *cmean*, to the dual-PRF field with extended aliasing presented in Section 7.3. The panels in Figure 7.7 correspond to the Northeast region of the

field in Figure 7.4 and show both the corrected field for each of the correction techniques and the corresponding gate labelling described above. This example illustrates how the *median* and *mean* methods generate false alarms and miss some of the outliers in the boundaries of the aliased region while the *cmean* method respects the non-outlier gates and appropriately corrects the outliers.

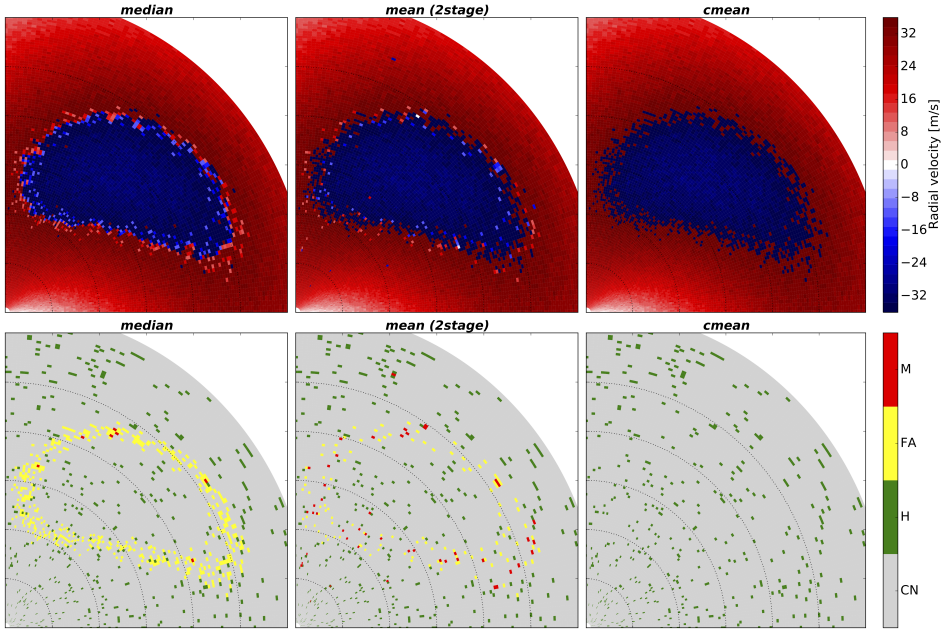

Figure 7.7: Comparative results of dual-PRF outlier correction in the presence of extended Nyquist aliasing, by means of the *mean*, *median* and *cmean* techniques: (top panels) corrected fields for each of the techniques and (bottom panels) labelling of each of the gates in the corrected fields as correct negatives (CN), hits (H), false alarms (FA) and misses (M). The original, uncorrected dual-PRF field has been simulated at an elevation of 4° from the wind profiles in Figure 7.4. Dotted range rings indicate 20 km intervals.

The three outlier correction techniques have also been applied to the series of simulated non-aliased dual-PRF velocity volumes. Taking into account that the outliers in the simulated fields arise uniquely as a result of random processes and that the noise distribution is Gaussian with fixed standard deviation, the fraction of outliers out of the total number of gates, F_{out}, depends only of the ratio between the threshold in Equation 7.7, $\Delta v_{\max}$, and the standard deviation of radial velocities: *sigma*:

$$F_{\text{out}} = 1 - P\left(\epsilon_{v_e} \in [-\Delta v_{\max}, \Delta v_{\max}]\right) = 1 - \text{erf}\left(\frac{\Delta v_{\max}}{2\sigma}\right), \tag{7.16}$$

where ϵ_{v_e} is the error of the velocity estimate of the gate with respect to the *true* velocity.

The fraction of outliers is given as in terms of the *Error Function*, which accounts for the probability of ϵ_{v_e} lying between $-\Delta v_{\max}$ and $\Delta v_{\max}$ thresholds for a Gaussian cumulative distribution function, as described in Holleman and Beekhuis (2003). Note that, for a fixed $\Delta v_{\max}$, the fraction of outliers and hence the probability of these getting clustered increases for increasing standard deviation of the radial velocities σ. Since the standard deviation of the radial velocities is different for each simulated volume, the performance of the techniques for different levels of clustering of the outliers can been assessed based on the analysis of the POD and EI verification indexes calculated for the corrected volumes.

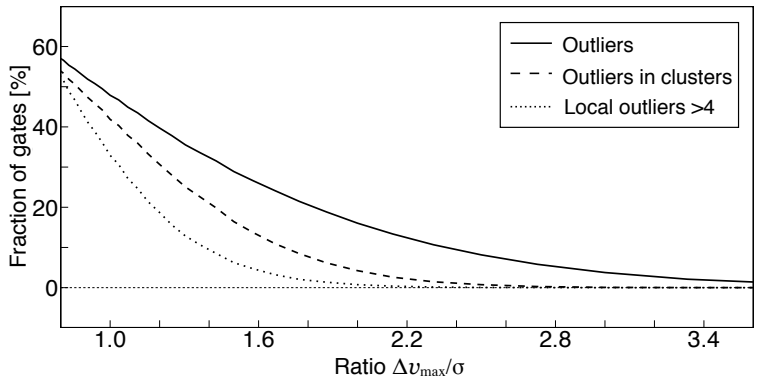

Figure 7.8: Fraction of outliers (solid line), fraction of clustered outliers (dashed line) and fraction of gates with more than 4 outliers in their immediate neighbourhood (dotted line) as a function of the $\Delta v_{\max}/\sigma$ ratio in simulations of dual-PRF radial velocity fields. The percentages are given based on the total number of gates 230400, encompassing all gates in the simulated fields at five different elevations (0°, 1°, 2°, 3° and 4°). The dual-PRF factor is $N = 3$ and the extended Nyquist velocity is V_{ae} =36 m s^{-1}.

The five simulated PPI fields within a volume contain a total of 230400 gates. The fraction of outliers out of this gate total is displayed in Figure 7.8 as a function of the $\Delta v_{\max}/\sigma$ ratio. Figure 7.8 also shows the fraction of gates with more than 4 outliers in the immediate neighbourhood (within a 3x3 sized window) and the fraction of clustered outliers. The latter accounts for all the outlier gates within a cluster, having defined a cluster as a collection of more than 3 contiguous out-

liers. The number of outliers grouped in clusters increases with decreasing $\Delta v_{\max}/\sigma$ ratios. This increase is particularly significant for ratios below 1.8 and when the $\Delta v_{\max}$ threshold equals the standard deviation of the velocity estimates, at which point almost all outliers pertain to a cluster and more than half of the total gates have more than 3 outliers in their neighbourhood.

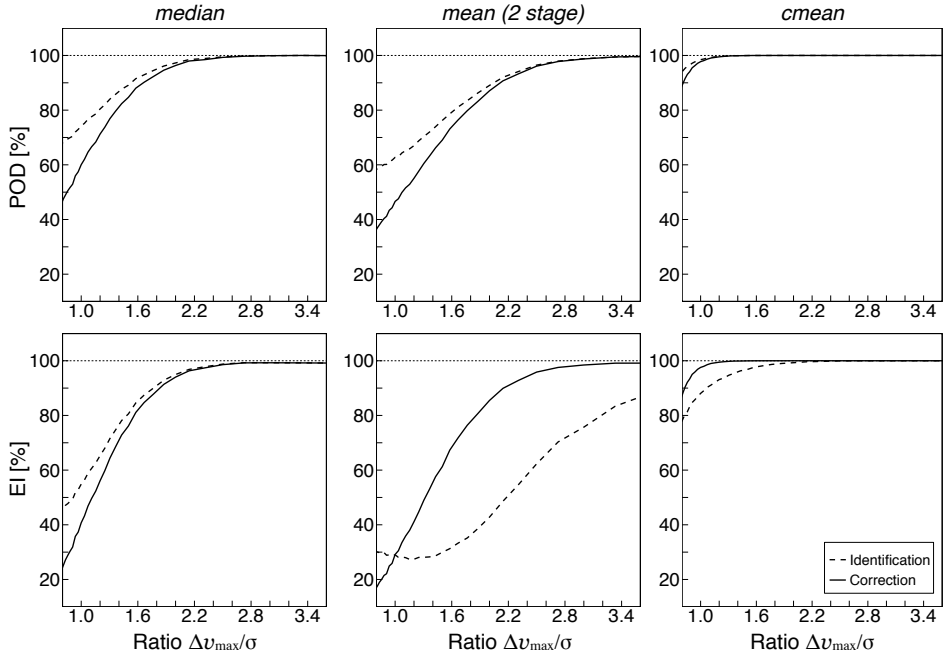

Figure 7.9: Probability Of Detection, POD (left panels) and Efficiency Index, EI (right panels) of the *median* (top panels), *mean* (central panels) and *cmean* (bottom panels) dual-PRF correction methods. The indexes are displayed as a function of the $\Delta v_{\max}/\sigma$ ratio in the simulations of dual-PRF velocity fields and are calculated separately for the outlier identification (dashed line) and correction (solid line) stages.

Figure 7.9 displays the POD and EI indexes as a function of $\Delta v_{\max}/\sigma$ for the three correction methods. The indexes separately score the identification and correction performance of the methods. From the POD values for the *median* technique it is derived that the number of misses in identification increases rapidly for ratios below ≈ 1.6, coinciding with the increase in the fraction of gates surrounded by more than 4 outliers, and that the higher the noise level the more hits are badly corrected. The comparison of POD and EI values leads to a similar conclusion for the false alarm rate. These results are attributed to the increasing concentration of

outliers and their biasing effect in the calculation of the local median. In the implementation of this method, identified outliers (hits and false alarms) are not removed in the correction stage and therefore all false alarms in identification remain false alarms after correction so the EI scores alone do not give additional information. As anticipated in Section 7.4, the number of misses and false alarms in identification is higher for *mean* method. However, the high false alarm rate in identification is somewhat reduced in the correction stage by removal of the identified outliers. The POD results suggest that the outlier removal requirement in this second stage is able to mitigate the erroneous correction of actual outliers (hits) only for ratios higher than ≈ 2.5.

Regarding the *cmean* method, the POD values show that this new technique identifies close to 100 % of errors down to a $\Delta v_{\max}/\sigma$ ratio of 1, when around half of the gates are outliers and around 80 % of these outliers are grouped in clusters. The EI values indicate that for ratios below ≈ 1.6 the fraction false alarms generated by the *cmean* method in identification is significative. However, the high hit rate in identification results in an improved performance of the correction procedure. The removal of identified outliers minimises the bias of the local median computed in the second correction stage; indeed, practically all the false alarms in identification are left uncorrected and more than 90 % of the outliers are properly corrected.

7.5.2 Dual-PRF fields from single-PRF observations

In the previous section a validation of the new correction procedure has been presented, based on synthetic dual-PRF velocity fields for which the uncertainty of all radial velocities follows the same Gaussian distribution. In the simulations, the underlying wind field is horizontally homogeneous and the azimuthal resolution is 1°, so significant azimuthal shear arises only randomly from the radial velocity uncertainties. However, in real situations, wind fields are often inhomogeneous, velocity uncertainties are heteroscedastic and radial velocity fields contain regions of missing data (filtered out or without significant echoes). In this section a more realistic validation of the dual-PRF outlier correction techniques is presented, based on dual-PRF velocity fields constructed from real single-PRF velocity fields.

In this analysis, raw data from the C-band Scanning ARM Precipitation Radar (CSAPR), located in the Southern Great Plains ARM facility (SGP I7 site) in Oklahoma (ARM, 2011), is used. The CSAPR radar provides PPI Doppler velocity data estimated at a single-PRF of 1240 Hz, corresponding to a Nyquist velocity of 16.5 $\mathrm{m\,s^{-1}}$. The grid has a resolution 120 m in range and 1° in azimuth and

the minimum and maximum ranges are 118 m and 118 km, respectively. Further information about the CSAPR radar can be found in Giangrande et al. (2013, 2014). On 20 June 2011 at 1800UTC a low pressure system in Kansas and associated frontal passage was directing a south-south-westerly flow across the plains. Mid-level instability and moisture led to a light to moderate line of precipitation. Large regions of winds greater than 50 knots led to large regions of aliasing, especially in sweeps at higher radar elevations.

A post-processing dealiasing algorithm has been run over radial velocity fields collected by the CSAPR on 20 June 2011 between 1817UTC and 1859UTC (ARM, 2011), and four well-dealiased PPI images at 4.4° elevation have been selected. Non-valid gates have been filtered out below a normalised coherent power threshold of 0.25. The four selected velocity fields, used as *reference* in the validation process, have been artificially folded in alternate radials into Nyquist intervals of $12\,\mathrm{m\,s^{-1}}$ and $9\,\mathrm{m\,s^{-1}}$ and further unfolded within the extended Nyquist interval of $36\,\mathrm{m\,s^{-1}}$ using the dual-PRF technique. The resulting dual-PRF images contain a total of 232989 valid gates of which 4.74 % constitute dual-PRF outliers. The *mean*, *median* and *cmean* correction techniques have been applied and their ability to reconstruct the *reference* fields by means of the POD and EI indexes has been evaluated.

Table 7.1: Probability Of Detection (POD) and Efficiency Index (EI) of the *median*, *median* and *mean* methods, calculated separately for the dual-PRF outlier identification and correction stages. The indexes are calculated for a selection of dual-PRF velocity fields derived from single-PRF radial velocity data collected by the ARM CSAPR radar on 20 June 2011.

Index	Stage	*median*	*mean (2stage)*	*cmean*
POD	Identification	88.3%	87.0%	95.7%
POD	Correction	83.2%	82.0%	90.7%
EI	Identification	83.6%	73.8%	85.4%
EI	Correction	78.5%	80.0%	88.9%

The validation indexes, summarised in Table 7.1, confirm the behaviour of each of the methods in identification and correction derived from the simulations in Subsection 7.5.1. Attending to the POD results, the *cmean* method is superior in the identification of dual-PRF outliers but all three methods perform similarly in the correction of the identified outliers. The comparison of the EI values for the three methods indicates that the removal of the outliers in the correction stage

reduces the false alarm rate.

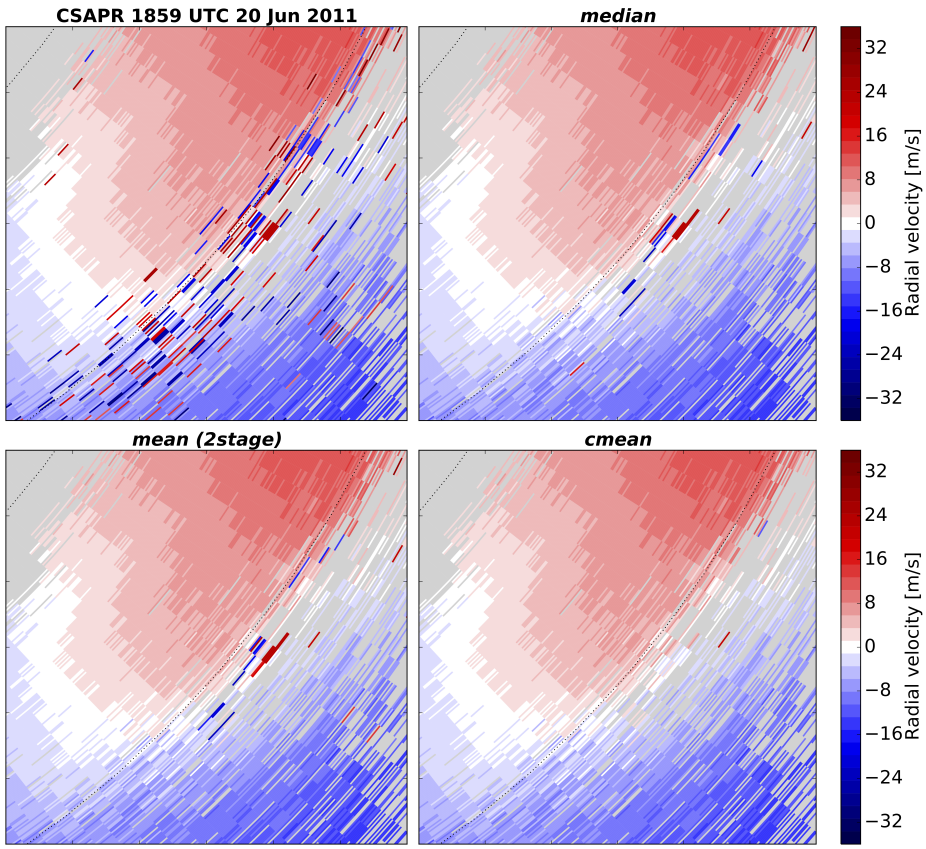

Figure 7.10: Example of outlier correction in a dual-PRF velocity field built from single-PRF velocity data collected by ARM CSAPR radar on 20 June 2011 at an elevation of 4.4°. Gates with a non-valid velocity value are filled in light grey colour and the two dotted rings indicate 60 km and 80 km ranges from the radar respectively.

Figure 7.10 illustrates the performance of the correction techniques when applied to a region of the dual-PRF velocity field derived from single-PRF observations at 1859UTC. This example illustrates the improved performance of the *cmean* technique in the correction of clustered outliers around regions filtered out due to a low signal quality index. However, POD and EI scores in Table 7.1 in comparison with the results obtained in Subsection 7.5.1 suggest that the miss and false alarm rate of the *cmean* method in identification may increase under real measurement conditions. These results may be attributed to biases in the reference circular mean estimate with respect to the actual velocity of the target gate when the local field is

highly variable, which are enhanced by the calculations in steps 2 to 4 of the identification process (Figure 7.2.2). This effect has a greater impact in the number of false alarms in identification, as expected from the shape of the *cmean* distribution in Figure 7.5 and as indicated by the EI scores in Table 7.1. The comparison of POD and EI scores in correction indicates that the outliers remaining at the end of the process correspond almost completely to the misses. That is, the correction stage works more effectively for the false alarms than for the misses. As observed in Figure 7.10, after removal of the identified outliers, the number of misses may increase close to regions of missing data likely due to the lack of valid neighbours for calculation of the statistics. Conversely, this effect benefits the correction of false alarms.

7.6 Application to real cases

The performance of the proposed *cmean* technique under actual dual-PRF measurement conditions is illustrated in this section for velocity images from three different events, recorded by the PBE, the LMI and the CDV radars of the XRAD. The PBE and the CDV radars estimate the radial velocity of the scatterers in dual-PRF mode with a PRF ratio of 1000/750 while the LMI radar scans with a PRF ratio of 1150/862, corresponding to extended Nyquist velocities of $40\,\mathrm{m\,s^{-1}}$ and $45.9\,\mathrm{m\,s^{-1}}$ respectively. The raw velocity data provided by these radars is filtered in the processor by application of the SQI and CSR thresholds (see Subsection 3.3.2 in Chapter 3).

7.6.1 The PBE radar, 7 September 2005

The first case studied corresponds to a tornado reported in Bech et al. (2007b) and rated F2 in the Fujita scale, that took place on the 07 September 2005 affecting the Barcelona International Airport. The radar image in Figure 7.11 is a reproduction of Figure 10 in Bech et al. (2007b), and shows the radial velocity field observed by the PBE radar minutes after the tornado crossed the runways of the airport, moving inland on a SE-NW track. The correction of the dual-PRF field by means of the *cmean* method, displayed in the right panel, allows a better identification of the couplet associated with the mesocyclone to the East of the radar site.

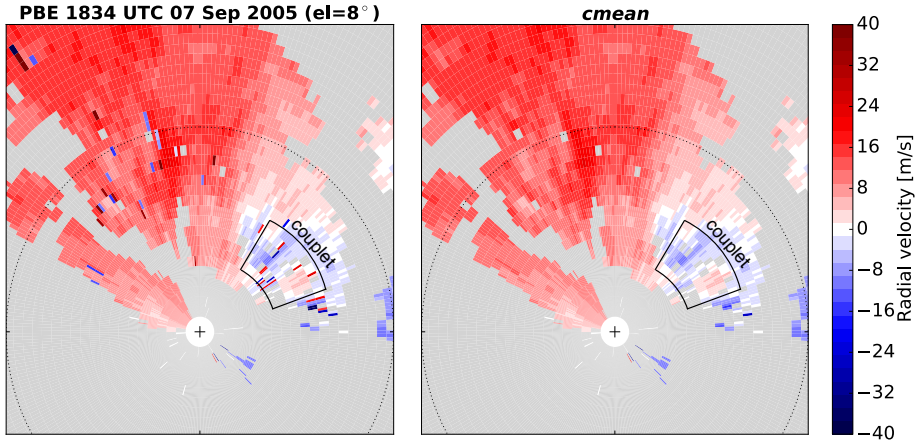

Figure 7.11: (Left) Dual-PRF radial velocity PPI image from the PBE radar at 1834UTC on 07 September 2005 at an elevation of 8.0°. (Right) Correction of the dual-PRF radial velocity image using the *cmean* technique. Gates with a non-valid velocity value are filled in light grey colour and dotted range rings indicate 20 km intervals.

7.6.2 The LMI radar, 2 November 2011

The second image presented is a snapshot by the LMI radar extracted from the tornadic event that took place on 02 November 2008 between 0000UTC and 1200UTC, described in Bech et al. (2011), Pineda et al. (2011) and Roca-Sancho et al. (2014). The velocity image, shown in Figure 7.12, is a zoom-out of Figure 7.1 and corresponds to the time of maximum ground damage (rated as F1 in the Fujita scale) by a thunderstorm microburst in the southern coast of Catalonia. The processing of the raw dual-PRF image by the *cmean* technique adequately corrects most of the dual-PRF dealiasing errors in a single pass, clarifying the divergent structure of the microburst. Only few outliers are missed in particular cases found within zones of high variability in the estimated velocities.

7.6.3 The CDV radar, 18 June 2013

The third case image, in Figure 7.13, is part of a severe thunderstorm event that produced hailstones with a maximum diameter of 3.5 cm in western Catalonia. The figure displays the velocity field observed by the CDV radar immediately after the time of maximum hail-fall. Hours later, the same thunderstorm produced an important flood event in the Val d'Aran valley (NW of Catalonia). In this case, highly sheared areas in the NW of the image have been filtered out. These areas are

recognisable by the high amount of dual-PRF outliers in their borders. This image also presents two aliased zones, one to the North and a larger one in the South. The *cmean* procedure corrects the clustered outliers in the borders of filtered out areas while preserving the edges of the zones with global aliasing. It can also be observed that the correction may have a higher failure rate in regions of clustered outliers that are semi-isolated; i.e. surrounded by gates with a non-valid velocity value.

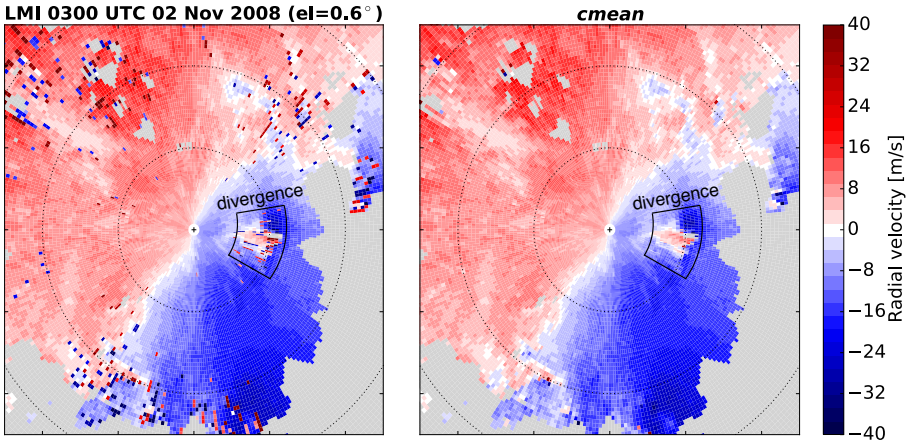

Figure 7.12: As Figure 7.11 but for the LMI radar at 0300UTC on 2 Nov 2008 at an elevation of 0.6°

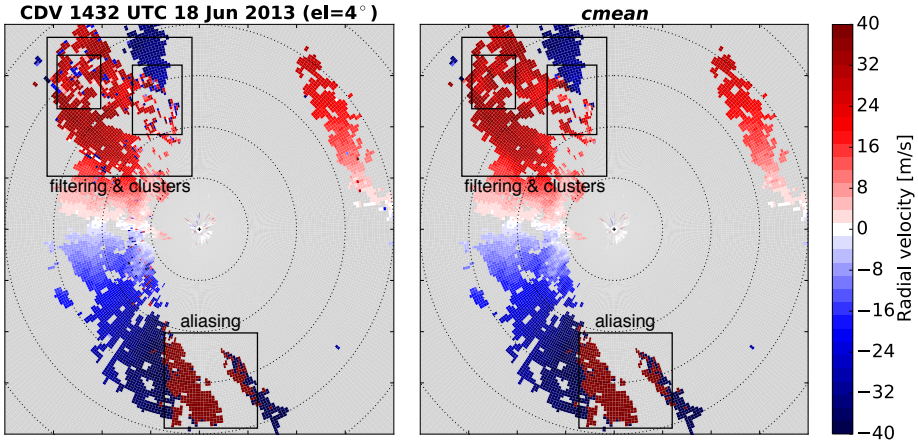

Figure 7.13: As Figure 7.11 but for the CDV radar at 1432UTC on 18 Jun 2013 at an elevation of 4.0°

7.7 Conclusions

The dual-PRF technique is widely used to extend the unambiguous velocity interval within which Doppler weather radars estimate the radial velocity of the scatterers. However, dual-PRF radial velocity images present characteristic unfolding errors or outliers that arise due to violation of the assumptions involved in the procedure. In the present chapter, two existing post-processing techniques have been analysed. These techniques identify and correct dual-PRF outliers by comparing the gate velocity with the mean or median velocity of the surrounding gates. It has been shown that these techniques require that a global dealiasing algorithm is run prior to the correction of the outliers and that their performance is limited by the presence of outliers in the surroundings.

From these premises, a new post-processing technique to correct dual-PRF outliers has been presented. Similar to the existing techniques, the proposed technique relies on the continuity of the local field but uses circular statistics and does not need prior application of a global dealiasing algorithm. The new technique is built in two stages that treat the identification and the correction of the outliers separately. In the identification stage, the gate velocities are converted into phases in a circle with a circumference that is twice the extended unambiguous velocity given by the dual-PRF procedure. The statistics to compute the local reference velocities that allow the identification of the outliers are calculated from these phases instead of directly from the velocities. Therefore, these circular statistics are not influenced by surrounding gates that present extended Nyquist aliasing. The method, as proposed in the present work, requires that the ratio of the high and low PRFs is of the type $(N+1)/N$ and that the PRF at which each radial has been scanned is known. The latter information is used to devise the identification algorithm in a way such that the biasing effect of neighbouring outliers in the calculation of the reference velocity is minimised. Working on the circular phase space only allows to identify the outliers and hence their correction needs to be carried on in velocity space, after removal of the surrounding outliers to prevent biases in the correction factors. The methodology used to correct the identified outliers in the second stage is similar to that of the existing post-processing technique based on the local median velocity, which is shown to be a more robust statistic than the mean velocity for the purpose. The removal of outliers together with the requirement that at least two surrounding gates have a valid velocity value may in few cases hamper the correction due to a lack of valid data in the neighbourhood.

The performance of the new technique has been quantitatively assessed using simulated dual-PRF fields and also dual-PRF velocity fields derived from real single-PRF observations. The analysis has shown that the proposed method is more effective and efficient in the identification of dual-PRF outliers than the two existing procedures analysed, denoting a significative improvement when the concentration of outliers is high. This is of particular importance because clusters of dual-PRF outliers are likely to be present in highly sheared areas, which are usually regions of interest when studying severe weather events. On the other hand, all three methods perform similarly in the correction of the identified outliers but if the removal of the outliers is applied prior to the correction stage the false alarm rate is reduced. Under real measurement conditions, the new algorithm has proven to have a superior overall performance than the two existing techniques, but it has been noticed that it may sporadically miss outliers and generate false alarms in areas where the underlying field is highly variable. This is attributed to inaccuracies in the reference phase estimate and, although being an effect common to the three methods, it may be enhanced in the new technique by the additional computations involved. It has also been shown that in the application to real dual-PRF velocity fields, exemplified through three dual-PRF velocity images corresponding to different severe weather events, the proposed technique satisfactorily corrects the outliers. Finally, the technique has been applied to a simulated velocity field and to a real dual-PRF velocity field with extended Nyquist aliasing and it has been verified that the methodology does not generate false alarms and appropriately corrects the outliers in the boundaries the regions presenting extended aliasing.

Part IV
CONCLUSIONS

8

Summary and conclusions

The design and implementation of standardised quality control procedures and tools is essential for homogenisation and compositing in weather radar networks and for a rigorous and efficient management of radar base data and products in downstream hydrological and meteorological applications.

The present thesis project has dealt with the improvement of the operative quality control of the XRAD, the weather radar network operated by the Meteorological Service of Catalonia (SMC); a regional network committed to comply with the quality standards established by the European and global referents. Under this framework, the main goals have focused on the continuous quality control of the weather radar system calibration status, recognised as valuable preventive proceeding and as a primary source of dynamic information on data quality, and on the correction of Doppler velocity data, which was not addressed in the quality control framework of the XRAD.

The methodologies proposed and developed have been selected and devised to complement and improve the already implemented ones for the XRAD and the results derived are generally applicable to any radar network. Furthermore, the development of the algorithms has been carried on through R (R Core Team, 2016) and Python (Python, 2001) open source programming languages so that they are freely and worldwide available for further usage, analysis, debugging and testing.

In the following, the general results and conclusions of the thesis work are summarised and several specific recommendations are provided for future consideration, organised according to the main and specific objectives laid out in Chapter 2.

8.1 Main objectives

1. *To implement, for the XRAD, methodologies for remote monitoring of the radar system performance and calibration state*:

   This task has been tackled in Chapter 4 and Chapter 5 through the adaptation and implementation of a fully automatic procedure that uses solar interferences detected in operational radar scans as reference for online monitoring of the antenna alignment and receiver chain calibration. The adapted algorithm has also proven useful for the detection and monitoring of interferences from external emitters of non-solar nature. In addition, the inter-comparison between antenna alignment assessment methodologies in Chapter 6 has shown that long-term results from the solar monitoring method can be used to detect and quantify the antenna pedestal levelling error.

2. *To improve the quality of the Doppler velocities estimated by the XRAD radars*:

   The main quality issue affecting the radial velocity fields estimated by the XRAD radars is the presence of dual-PRF outliers. To address this issue, a post-processing algorithm for identification and correction of the dual-PRF outliers has been devised. The proposed algorithm, described in Chapter 7, relies on the spatial continuity of the velocity field and can be employed independently of post-processing dealiasing algorithms.

3. *To provide guidelines for application of the proposed quality control methodologies and resources for the interpretation of their results*:

   In this regard, the proposed quality control methodologies have been analysed in detail. In particular, in Chapter 5, the application limits of the Sun-monitoring method have been formulated in a thorough derivation of the underlying physical model. In addition, the accuracy of the Sun-monitoring technique has been investigated for different observation conditions simulated in a controlled sensitivity analysis. Chapter 6 has been devoted to the comparative assessment of the advantages and limitations of three existing methods for antenna pointing calibration, including the solar monitoring technique. The performance of the dual-PRF outlier correction technique has been quantitatively tested in Chapter 7, in comparison with other existing correction techniques in order to demonstrate its improved correction ability while recognising and understanding its limitations.

8.2 Specific objectives

(a) **To adapt a solar interference detection algorithm for its application under the scanning settings of the XRAD:**

The Sun-monitoring methodology developed by Holleman and Beekhuis (2004) includes an algorithm that uses the signal continuity at long ranges and the proximity of the signal to the solar position for identification of solar interferences in operational reflectivity data. However, in the case of radar scans of mid-range coverage as those of the XRAD, these characteristics alone are not sufficient for adequate detection of the solar interferences and accurate estimation of their power.

It has been shown that the detection algorithm can be adapted to mid-range coverages by exploiting the constant power characteristic of the solar signal. The algorithm has been modified using the median and median absolute deviation robust statistics to estimate the power of the solar interference and its variability along range. A long-term analysis of solar interferences has revealed that the along-range variability of their power is delimited below 2 dB. Including this threshold in the adapted algorithm serves to differentiate solar interferences from signals whose main contribution comes from ground clutter or precipitation.

The constancy and continuity characteristics also apply to the interferences from external Radio Local Area Network (RLAN) emitters and, hence, the adapted detection algorithm, excluding the solar proximity criterion, can be used to register the location and to discern the origin of persistent RLAN interferences. In the XRAD, RLAN interference incidence monitoring by these means provides key information for appealing to the competent radiocommunication authorities that regulate the bandwidth sharing.

Recommendations: (1) To use robust statistical estimators and to include the constancy criterion when applying the Sun-monitoring algorithm for any coverage range scans, for increased accuracy in the solar interference detection and characterisation process (see also the results in Huuskonen et al., 2016). (2) To apply the detection algorithm for all daily scans (not only to those close to sunrise or sunset) in order to register persistent RLAN interferences.

(b) **To implement for the XRAD the online Sun-monitoring technique:**

The core of the Sun-monitoring technique is the inversion of a theoretical model which uses as input the power and position of the solar interferences detected in operational scans. It has been shown how strongly outlying observations, attributed to non-solar signals that have gone all through the detection process, can drift the results of the inversion yielding biased values for the retrieved calibration parameters. A non-iterative procedure for *ad-hoc* removal of these outliers has been designed. The application of the solar monitoring method, including the outlier removal procedure, to the solar interferences detected by the XRAD radars has demonstrated its usefulness to remotely detect miscalibrations, antenna misalignments and even system performance anomalies on a daily basis. Two inversion approaches have been analysed: a three parameter model inversion (3P model), which provides estimates of the antenna pointing biases in azimuth and elevation and of the solar power at the top of the atmosphere; and a full five parameter model inversion (5P model), which additionally gives estimates of the solar image widths in azimuth and elevation. The values of these solar image widths stem from the convolution between the antenna sensitivity pattern and the solar-disk emission and depend on the scanning motion of the antenna. The analytical means to estimate the expected solar image widths from system parameters (antenna beamwidth and scanned radial width) have been explicitly formulated in a complete derivation of the solar interference model. All these results may be found compiled in Altube et al. (2015a).

Recommendations: (1) To limit the Sun-interference model application to radars with antenna beamwidths larger than 0.3° and for which the ratio between the scanned radial ray and the antenna-Sun convolution widths is below 1.5. For an accurate analytical computation of the convolution width using the formula given in Baars (1973) a beamwidth larger than 0.7° is required. (2) To include the outlier removal method in the Sun-monitoring procedure for increased robustness in the inversion. (3) To monitor fit statistics, e.g. the Root Mean Squared Deviation of the fit residuals (RMSD), on a daily basis in order to detect method failures, which may often be attributed to anomalies in the radar system performance or to changes in the constant parameters such as the antenna gain and beamwidth.

(c) **To study the accuracy of the Sun-monitoring technique under varying observation conditions:**

The application of the Sun-monitoring technique to the XRAD has shown that, when the sensitivity of the radar system is close to the peak power of the solar signal, the 5P model inversion is often ill conditioned for the retrieval of the solar image widths. The Sun-monitoring methodology has been artificially reproduced under controlled conditions to investigate how the ill-conditioning of the problem is constrained by the accuracy, number and distribution of the solar observations.

The performance analysis has shown that, in a 5P model inversion, the estimation of the solar image widths introduces uncertainty in the estimation of the solar peak power because the accuracies in the estimates are negatively correlated. In addition, the non-linearity of the 5P model affects the error distribution of the estimated parameters, specially that of the solar widths, and these can no longer be considered normal. The effects of the correlation and of the non-linearity are enhanced for decreasing number of observations available for the fit and for a distribution of observations corresponding to a low sensitivity radar, which detects only solar signals when the antenna is pointing close to the solar disk centre.

It has also been noticed that, for both the 3P and the 5P inversion approaches, the estimates of the calibration parameters become increasingly unstable when the number of observations decreases, so that a minimum number of solar observations are required to achieve the desired accuracy. The minimum number of observations required depends on the accuracy of the observations and on the distribution of the latter. For instance, for a low sensitivity radar system the number of observations required to accurately estimate the solar image widths may be higher than 120 even when the solar observations have been accurately characterised in the detection process. This is a difficult number of observations to achieve by a low sensitivity radar on a daily basis even when observations from consecutive days are collected. In these cases, application of the 3P model may be more appropriate for an improved accuracy in the antenna pointing bias and receiver chain calibration. Part of these results have been presented in (Altube et al., 2014) and (Altube et al., 2015b).

Recommendations: (1) To examine the distribution of the solar observations collected and to determine, using the solar interference model weighting functions, if the radar is sensitive enough to detect solar signals that carry relevant information for the retrieval of the widths. (2) To use the RMSD of the fit as indicator of the average error of the solar dataset in order to acknowledge which is the number of observations required to achieve the desired accuracy or if the number of observations available ensures such accuracy. (3) To rely on the 3P model inversion if the requirements for the accuracy in the retrieval of the widths are not met. (4) To automatically quality control the Sun-monitoring method results using the weighting functions, the average error and/or the number of observations as indicators.

(d) To compare the solar technique with methodologies for antenna alignment calibration already implemented for the XRAD:

Prior to the implementation of the Sun-monitoring technique, two other methodologies were already available for antenna alignment assessment in the XRAD. One of these methods is based on an offline scan of the Sun-disk and is employed by XRAD technicians in routine maintenance tasks. The last technique correlates measured ground clutter echoes with echoes simulated using a high-resolution digital elevation model to determine the antenna pointing bias. The three techniques have been reviewed and compared under actual operative conditions. Antenna pointing bias estimates gathered in a dedicated one-month campaign, during which the offline Sun-scanning procedure was run on a daily basis, have allowed a direct inter-comparison of the methods, highlighting their advantages and limitations in each case. The discrepancies detected in this short term comparison have been further investigated and clarified through the analysis of the bias estimates reported by the methods in the course of a one-year period. The analysis has revealed that the estimated pointing biases may vary depending on the antenna or Sun position at the time of the observation or may be conditioned by the spatial distribution of the ground echoes, specially if a pedestal levelling error is present.

In this regard, It has been shown how the Sun-monitoring methodology can be slightly modified, accounting for the azimuthal antenna position at the time of observation, in order to simultaneously quantify, preferably with the

aim of complementary data provided by the offline Sun-scan method, the pedestal levelling error and the systematic antenna pointing bias. When a levelling error is present and taken into account in the interpretation of the reported biases, the results from the three methods adequately agree. This inter-comparison and the derived results and conclusions are compiled in Altube et al. (2016b) and Altube et al. (2015c).

Recommendations: (1) To consider the antenna/Sun position at the time of observation when interpreting the pointing biases reported by the solar methods. (2) To consider the distribution and amount of influential ground clutter bins to interpret the accuracy of the pointing biases reported by the ground clutter method. (3) To combine the solar methods in a one-year, long-term analysis devised to quantify the pedestal levelling error, programming the offline Sun scans in advance in order to cover southerly azimuthal sections not reachable by the online method. For instance, given the geolocation of the XRAD, a monthly Sun-scan at a fixed elevation of 25° gives coverage to azimuths ranging from 80° to 280°. In addition, monthly Sun-scans at one or two fixed azimuthal positions are recommended (e.g. 150° and 200° in the case of the XRAD, covering elevations from 10° to 70°), with the aim of determining the dependence of the pointing bias with the zenithal position of the antenna.

(e) **To devise an algorithm that identifies and corrects dual-PRF outliers in Doppler velocity data:**

Unfolding errors or outliers in dual-PRF velocity data appear as clear discontinuities in the velocity field. An image processing methodology has been devised to correct these dual-PRF outliers and improve the quality of the Doppler radar velocity data. Similar to other existing techniques, the proposed technique identifies and corrects the outliers by comparison with a reference velocity estimated from the field in the immediate vicinity. However, the new methodology estimates the reference velocity using circular statistics applied to the phase of the surrounding gates instead of classical statistics applied to their velocities, making it more robust to the presence of outliers in the neighbourhood or to extended Nyquist aliasing in the estimated velocity field.

The improved ability of the algorithm to correct clustered outliers and outliers

in the edges of aliased regions has been quantitatively assessed and ratified, in comparison to two other existing correction techniques, using simulated dual-PRF velocity fields and also dual-PRF fields derived from actual single-PRF fields. Despite the algorithm still sporadically misses outliers close to regions of missing data or in areas where the underlying wind field is highly variable, its improved capabilities make it advantageous for a flexible design of the Doppler velocity quality control flow. A detailed description of the algorithm and of the results of performance assessment conclusions have been included in Altube et al. (2016a).

Recommendations: (1) To run the dual-PRF correction algorithm prior to the application of extended aliasing correction algorithms, which often may erroneously identify and correct the outlying gates as aliased gates. (2) To study wether the outlier correction algorithm can help reducing the Signal-Quality-Index filter threshold, so that it allows to make the most of the velocity estimates in turbulent or highly sheared regions.

References

Altube, P., J. Bech, O. Argemí, and T. Rigo, 2014: Weather radar online Sun-monitoring in presence of leverage outliers: five or three parameter model inversion? *Extended abstracts, 8th European Conference on Radar Meteorology and Hydrology (ERAD)*, Garmisch-Partenkirchen, Germany.

Altube, P., J. Bech, O. Argemí, and T. Rigo, 2015a: Quality control of antenna alignment and receiver calibration using the sun: adaptation to mid range weather radar observations at low elevation angles. *J. Atmos. Oceanic Technol.*, **32**, 927–942.

Altube, P., J. Bech, O. Argemí, T. Rigo, and N. Pineda, 2015b: Performance study of the radar Sun-monitoring method. *Poster presentation, 37th Conference on Radar Meteorology*, Norman, Oklahoma, AMS.

Altube, P., J. Bech, O. Argemí, T. Rigo, and N. Pineda, 2015c: Weather radar antenna pointing accuracy assessment: three method inter-comparison. *Oral presentation, 37th Conference on Radar Meteorology*, Norman, Oklahoma, AMS, [Available online at https://ams.confex.com/ams/37RADAR/webprogram/Paper275599.html].

Altube, P., J. Bech, O. Argemí, T. Rigo, and N. Pineda, 2016a: Correction of dual-PRF velocity outliers in the presence of aliasing. *J. Atmos. Oceanic Technol.*, under review.

Altube, P., J. Bech, O. Argemí, T. Rigo, and N. Pineda, 2016b: Intercomparison and potential synergies of three methods for weather radar antenna pointing assessment. *J. Atmos. Oceanic Technol.*, **33**, 331–343.

Aran, M., J. Amaro, J. Arús, J. Bech, F. Figuerola, M. Gayà, and E. Vilaclara, 2009: Synoptic and mesoscale diagnosis of a tornado event in Castellcir, Catalonia, on 18th October 2006. *Atmos. Res.*, **93 (1)**, 147–160.

Argemí, O., P. Altube, T. Rigo, J. Bech, N. Pineda, and X. Ortiga, 2014: Towards the improvement of monitoring and data quality assessment in the weather radar network of the Meteorological Service of Catalonia (SMC). *Poster presentation, 8th European Conference on Radar Meteorology and Hydrology (ERAD)*, Garmisch-Partenkirchen, Germany.

Argemí, O., N. Pineda, T. Rigo, A. Belmonte, X. Fabregas, and J. Bech, 2012: Wind turbine impact evolution and beam blockage analysis on the weather radar network of the meteorological service of catalonia. *Proceedings, 2nd European Conference on Radar Meteorology and Hydrology*, Delft, Netherlands, ERAD, 312–317.

ARM, 2011: Atmospheric Radiation Measurement (ARM) Climate Research Facility. C-Band ARM Precipitation Radar (CSAPR). 2011-06-11, 36.7962 N 97.4484 W: Southern Great Plains (SGP) Nardin, OK (C-band radar site, Intermediate/Auxiliary) (I7). Compiled by N. Bharadwaj, D. Nelson, B. Isom, J. Hardin, I. Lindenmaier, S. Collis and A. Matthews. Atmospheric Radiation Measurement (ARM) Climate Research Facility Data Archive: Oak Ridge, Tennessee, USA. [Data set accessed 2015-09-20 at http://dx.doi.org/10.5439/1025169.].

Atencia, A., and Coauthors, 2010: Improving QPF by blending techniques at the Meteorological Service of Catalonia. *Nat. Hazards Earth Syst. Sci.*, **10 (7)**, 1443–1455.

Atlas, D., 1990: *Radar in meteorology: Battan memorial and 40th anniversary radar meteorology conference*. American Meteorological Society, Boston, 806 pp.

Baars, J. W. M., 1973: The measurement of large antennas with cosmic radio sources. *IEEE Trans.*, **AP-21**, 461–474.

BALTRAD, 2008: An advanced weather network for the Baltic Sea region. http://baltrad.eu.

Banjanin, Z. B., and D. S. Zrnić, 1991: Clutter rejection for Doppler weather radars which use staggered pulses. *IEEE Trans. Geosci. Remote Sens.*, **GRS-29**, 610–620.

Barnolas, M., and M. C. Llasat, 2007: A flood geodatabase and its climatological applications: the case of Catalonia for the last century. *Nat. Hazards Earth Syst. Sci.*, **7 (2)**, 271–281.

Battan, L. J., 1973: *Radar observation of the atmosphere*. The University of Chicago Press, Chicago, 324 pp.

Bean, B., and E. J. Dutton, 1966: Radio meteorology. National Bureau of Standards Monograph 92, US Government Printing Office, Washington D. C., 435 pp.

Bebbington, D., S. Rae, J. Bech, B. Codina, and M. Picanyol, 2007: Modelling of weather radar echoes from anomalous propagation using a hybrid parabolic equation method and NWP model data. *Nat. Hazards Earth Syst. Sci.*, **7**, 391–398.

Bech, J., B. Codina, and J. Lorente, 2007a: Forecasting weather radar propagation conditions. *Meteor. Atmos. Phys.*, **96**, 229–243.

Bech, J., B. Codina, J. Lorente, and D. Bebbington, 2003: The sensitivity of single polarization weather radar beam blockage correction to variability in the vertical refractivity gradients. *J. Atmos. Oceanic Technol.*, **20**, 845–855.

Bech, J., M. Gayà, M. Aran, F. Figuerola, J. Amaro, and J. Arús, 2009: Tornado damage analysis of a forest area using site survey observations, radar data and a simple analytical vortex model. *Atmos. Res.*, **93 (1)**, 118–130.

Bech, J., R. Pascual, T. Rigo, N. Pineda, J. M. López, J. Arús, and M. Gayà, 2007b: An observational study of the 7 September 2005 Barcelona tornado outbreak. *Nat. Hazards Earth Syst. Sci.*, **7**, 129–139.

Bech, J., T. Rigo, N. Pineda, S. Segalà, E. Vilaclara, R. Sánchez-Diezma, D. Sempere, and E. Velasco, 2005: Implementation of the EHIMI software package in the weather radar operational chain of the catalan meteorological service. *Proceedings of 32nd Conference on Radar Meteorology*, Albuquerque-EUA, AMS, Vol. 3.

Bech, J., and Coauthors, 2004: The weather radar network of the Catalan Meteorological Service: description and applications. *Proceedings, 3rd European Conference on Radar Meteorology and Hydrology*, Visby, Sweden, ERAD.

Bech, J., and Coauthors, 2011: A Mediterranean nocturnal heavy rainfall and tornadic event. Part I: Overview, damage survey and radar analysis. *Atmos. Res.*, **100**, 621–637.

Beekhuis, H., and H. Leijnse, 2012: An operational radar monitoring tool. *Proceedings, 7th European Conference on Radar Meteorology and Hydrology*, Toulouse, France, ERAD.

Bellon, A., and G. Austin, 1978: The evaluation of two years of real-time operation of a short-term precipitation forecasting procedure (SHARP). *J. Appl. Meteor.*, **17 (12)**, 1778–1787.

Bellon, A., and A. Kilambi, 1999: Updates to the McGill RAPID (Radar Data Analysis, Processing and Interative Display) system. *Proceedings, 29th International Conference on Radar Meteorology*, Montreal, Canada, 121–124.

Bellon, A., and I. Zawadzki, 2003: A 9-year summary of radar characteristics of mesocyclonic storms and deep convection in southern Quebec. *Atmos.–Ocean*, **41**, 99–120.

Belmonte, A., and X. Fabregas, 2010: Analysis of wind turbines blockage on doppler weather radar beams. *IEEE Antennas Wireless Propagat. Lett*, **9**, 670–673.

Berenguer, M., C. Corral, R. Sánchez-Diezma, and D. Sempere-Torres, 2005: Hydrological validation of a radar-based nowcasting technique. *J. Hydrometeor.*, **6 (4)**, 532–549.

Berenguer, M., G. Lee, D. Sempere-Torres, and I. Zawadzki, 2002: A variational method for attenuation correction of radar signal. *Proceedings, 2nd European Conference on Radar Meteorology and Hydrology*, Delft, Netherlands, ERAD.

Berenguer, M., D. Sempere-Torres, C. Corral, and R. Sánchez-Diezma, 2006: A fuzzy logic technique for identifying nonprecipitating echoes in radar scans. *J. Atmos. Oceanic Technol.*, **23 (9)**, 1157–1180.

Berenguer, M., D. Sempere-Torres, and M. Hürlimann, 2015: Debris-flow forecasting at regional scale by combining susceptibility mapping and radar rainfall. *Nat. Hazards Earth Syst. Sci.*, **15**, 587–602.

Bergen, W. R., and S. C. Albers, 1988: Two- and three-dimensional de-aliasing of Doppler radar velocities. *J. Atmos. Oceanic Technol.*, **5**, 305–319.

Berne, A., G. Delrieu, and H. Andrieu, 2005: Estimating the vertical structure of intense mediterranean precipitation using two x-band weather radar systems. *J. Atmos. Oceanic Technol.*, **22 (11)**, 1656–1675.

Berne, A., and W. F. Krajewsky, 2013: Radar for hydrology: Unfulfilled promise or unrecognized potential? *Adv. Water Resour.*, **51**, 357–366.

Bevington, P. R., and D. K. Robinson, 1969: Least-squares fit to a straight line: Error estimation, Section 6.4. *Data reduction and error analysis for the physical sciences*, 3rd ed., McGraw-Hill, 107–110, [Available online at http://www.gae.ucm.es/~pulsar/books/statistics/].

Blahak, U., 2008: An approximation to the effective beam weighting function for scanning meteorological radars with an axisymmetric antenna pattern. *J. Atmos. Oceanic Technol.*, **25**, 1182–1196.

Botzen, W. J. W., L. M. Bouwer, and J. C. J. M. Van den Bergh, 2010: Climate change and hailstorm damage: Empirical evidence and implications for agriculture and insurance. *Resour. Energy Econ.*, **32 (3)**, 341–362.

Brandão, A. L., J. Sydor, W. Brett, J. Scott, P. Joe, and D. Hung, 2005: 5 GHz RLAN interference on active meteorological radars. *IEEE 61st Vehicular Technology Conference*, Stockholm, Sweden, IEEE, Vol. 2, 1328–1332.

Bringi, V. N., and V. Chandrasekar, 2001: *Polarimetric Doppler weather radar: principles and applications*. Cambridge University Press.

Brown, R. A., and V. T. Wood, 2007: *A guide for interpreting Doppler velocity patterns: Northern Hemisphere Edition*. 2nd ed., U.S. Dept. of Commerce, National Weather Service, Norman, Oklahoma, 55 pp.

Browning, K., and C. Collier, 1989: Nowcasting of precipitation systems. *Rev. Geophys.*, **27 (3)**, 345–370.

Browning, K., and R. Wexler, 1968: The determination of kinematic properties of a wind field using doppler radar. *J. Appl. Meteor.*, **7 (1)**, 105–113.

Caruana, R. A., R. B. Searle, T. Heller, and S. I. Shupack, 1986: Fast algorithm for the resolution of spectra. *Anal. Chem.*, **58 (6)**, 1162–1167.

Chandrasekar, V., L. Baldini, N. Bharadwaj, and P. L. Smith, 2014: Recommended calibration procedures for GPM ground validation radars. GPM Tier1 documentation Draft n.9, Global Precipitation Measurement Project, 100 pp.

Chandrasekar, V., and A. P. Jayasumana, 2001: Radar design and management in a networked environment. *ITCom 2001: International Symposium on the Convergence of IT and Communications*, International Society for Optics and Photonics, 142–147.

Chandrasekar, V., R. Keränen, S. Lim, and D. Moisseev, 2013: Recent advances in classification of observations from dual polarization weather radars. *Atmos. Res.*, **119**, 97–111.

Chandrasekar, V., and S. Lim, 2008: Retrieval of reflectivity in a networked radar environment. *J. Atmos. Oceanic Technol.*, **25 (10)**, 1755–1767.

Cho, J. Y. N., 2005: Multi-pri signal processing for the terminal doppler weather radar. part ii: Range-velocity ambiguity mitigation. *J. Atmos. Oceanic Technol.*, **22 (10)**, 1507–1519.

Collier, C., 1993: The application of a continental-scale radar database to hydrological process parametrization within Atmospheric General Circulation Models. *J. Hydrol.*, **142 (1)**, 301–318.

Collier, C., 1996: *Applications of weather radar systems: a guide to uses of radar data in meteorology and hydrology*. 2nd ed., John Wiley & Sons Ltd.

Collier, C., 2007: Flash flood forecasting: What are the limits of predictability? *Quart. J. Roy. Meteor. Soc.*, **133 (622)**, 3–23.

Cunha, L. K., J. A. Smith, W. F. Krajewski, M. L. Baeck, and B.-C. Seo, 2015: NEXRAD NWS polarimetric precipitation product evaluation for IFloodS. *J. Hydrometeor.*, **16 (4)**, 1676–1699.

Darlington, T., M. Kitchen, J. Sugier, and J. de Rohan-Truba, 2003: Automated real-time monitoring of radar sensitivity and antenna pointing accuracy. *Preprints, 31st Conference on Radar Meteorology*, Seattle, US-WA, Amer. Meteor. Soc., 538–541.

Dazhang, T., S. G. Geotis, R. E. P. Jr., A. L. Hansen, and C. L. Frush, 1984: Evaluation of an alternating-PRF method for extending the range of unambiguous Doppler velocity. *Preprints, 22nd Conference on Radar Meteorology*, Zurich, Switzerland, Amer. Meteor. Soc., 523–527.

Delobbe, L., and I. Holleman, 2006: Uncertainties in radar echo top heights used for hail detection. *Meteor. Atmos. Phys.*, **13**, 361–374.

Delrieu, G., S. Caoudal, and J. D. Creutin, 1997: Feasibility of using mountain return for the correction of ground-based X-band weather radar data. *J. Atmos. Oceanic Technol.*, **14 (3)**, 368–385.

Delrieu, G., J. D. Creutin, and H. Andrieu, 1995: Simulation of radar mountain returns using a digitized terrain model. *J. Atmos. Oceanic Technol.*, **12**, 1038–1049.

Divjak, M., 2009: Radar data quality-ensuring procedures at european weather radar stations. Subproject 1c/1 OPERA/WD/9/1999, OPERA-EUMETNET, 12 pp.

Dixon, M., and G. Wiener, 1993: TITAN: Thunderstorm identification, tracking, analysis, and nowcasting - a radar-based methodology. *J. Atmos. Oceanic Technol.*, **10 (6)**, 785–797.

Doviak, R. J., and D. S. Zrnič, 1984: *Doppler radar and weather observations*. 2nd ed., Dover Publications, 592 pp.

DRAO, 1990: Solar Radio Monitoring Database. National Research Council of Canada, Dominion Radio Astrophysical Observatory, solar flux data available at: [http://www.spaceweather.gc.ca/solarflux/sx-en.php].

Eastment, J. D., J. W. F. Goddard, G. J. Davies, D. N. Ladd, and K. J. Twort, 2001: Boresight pointing calibration for the Chilbolton radar using galactic radio sources and satellite targets. *Preprints, 30th Conference on Radar Meteorology*, Munich, Germany, Amer. Meteor. Soc., 23–25.

Eilts, M. D., and S. D. Smith, 1990: Efficient dealiasing of Doppler velocities using local environment constrains. *J. Atmos. Oceanic Technol.*, **7**, 118–128.

EUMETNET, 2008: Recommendation on C-band meteorological radars design to ensure global and long-term coexistence with 5 GHz RLAN. Tech. rep., 35th EUMETNET Council, Reading, UK, 1-36 pp.

Figueras i Ventura, J., and P. Tabary, 2013: The new french operational polarimetric radar rainfall rate product. *J. Climate Appl. Meteor.*, **52 (8)**, 1817–1835.

Fisher, N. I., 1993: *Statistical analysis of circular data.* 1st ed., Cambridge University Press, New York, 279 pp.

Fornasiero, A., P. Alberoni, R. Amorati, and C. Marsigli, 2006a: Improving the radar data mosaicking procedure by means of a quality descriptor. *Proceedings, 4th European Conference on Radar Meteorology and Hydrology*, Barcelona, Spain, ERAD.

Fornasiero, A., P. Alberoni, and J. Bech, 2006b: Statistical analysis and modelling of weather radar beam propagation conditions in the po valley (italy). *Nat. Hazards Earth Syst. Sci.*, **6 (2)**, 303–314.

Fornasiero, A., P. P. Alberoni, R. Amorati, L. Ferraris, and A. C. Taramasso, 2005: Effects of propagation conditions on radar beam-ground interaction: impact on data quality. *Adv. Geosci.*, **2**, 201–208.

Frech, M., 2009: Towards monitoring and assessing DualPol data quality. Contribution to OPERA WP1.4a: Evaluation of new technologies, OPERA-EUMETNET, 54 pp.

Frech, M., 2013: Monitoring the data quality of the new polarimetric weather radar network of the German Meteorological Service. *36th Conference on Radar Meteorology*, Breckenridge, US-CO, 9B.3 Online manuscript.

Frei, C., and C. Schär, 1998: A precipitation climatology of the Alps from high-resolution rain-gauge observations. *Int. J. Climatol.*, **18 (8)**, 873–900.

Friedrich, K., M. Hagen, and T. Einfalt, 2006: A quality control concept for radar reflectivity, polarimetric parameters, and Doppler velocity. *J. Atmos. Oceanic Technol.*, **23 (7)**, 865–887.

Frush, C., R. J. Doviak, M. Sachidananda, and D. S. Zrnić, 2002: Application of the SZ phase code to mitigate range-velocity ambiguities in weather radars. *J. Atmos. Oceanic Technol.*, **19**, 413–430.

Frush, C. L., 1984: Using the Sun as calibration aid in multiple parameter meteorological radar. *Preprints, 22nd Conference on Radar Meteorology*, Zurich, Switzerland, Amer. Meteor. Soc., 306–311.

Fulton, R. A., J. P. Breidenbach, D.-J. Seo, D. A. Miller, and T. O'Bannon, 1998: The WSR-88D rainfall algorithm. *Wea. Forecasting*, **13 (2)**, 377–395.

Futrell, J., and Coauthors, 2005: Water: Challenges at the intersection of human and natural systems. Tech. Rep. PNWD-3597, NSF/DOE, 50 pp.

Gabella, M., and G. Perona, 1998: Simulation of the orographic influence on weather radar using a geometric-optics approach. *J. Atmos. Oceanic Technol.*, **15 (6)**, 1485–1494.

Gayà, M., M.-C. Llasat, and J. Arús, 2011: Tornadoes and waterspouts in Catalonia (1950-2009). *Nat. Hazards Earth Syst. Sci.*, **11**, 1875–1883.

Gekat, F., P. Meischner, K. Friedrich, M. Hagen, J. Koistinen, D. B. Michelson, and A. Huuskonen, 2004: The state of weather radar operations, networks and products. *Weather Radar. Principles and Advanced Applications*, Springer, 1–51.

Genz, A. C., and A. A. Malik, 1980: Remarks on algorithm 006: An adaptive algorithm for numerical integration over an N-dimensional rectangular region. *J. Comp. Appl. Math.*, **6 (4)**, 295–302.

Germann, U., M. Berenguer, D. Sempere-Torres, and M. Zappa, 2009: REAL - Ensemble radar precipitation estimation for hydrology in a mountainous region. *Quart. J. Roy. Meteor. Soc.*, **135 (639)**, 445–456.

Germann, U., M. Boscacci, M. Gabella, and M. Schneebeli, 2016: Weather radar in Switzerland. *From weather observations to atmospheric and climate sciences in Switzerland: Celebrating 100 years of the Swiss Society for Meteorology.*

Germann, U., G. Galli, M. Boscacci, and M. Bolliger, 2006: Radar precipitation measurement in a mountainous region. *Quart. J. Roy. Meteor. Soc.*, **132 (618)**, 1669–1692.

Giangrande, S. E., S. Collis, A. K. Theisen, and A. Tokay, 2014: Precipitation estimation from the ARM distributed radar network during the MC3E campaign. *J. Climate Appl. Meteor.*, **53**, 2130–2147.

Giangrande, S. E., R. McGraw, and L. Lei, 2013: An application of linear programming to polarimetric radar differential phase processing. *J. Atmos. Oceanic Technol.*, **30**, 1716–1729.

Gjertsen, U., 2002: Gauge adjustment of precipitation estimates from the norwegian weather radar network. *COST-717 working document WDF_02_200203_3.*

Gjertsen, U., and J. I. Dahl, 2002: Challenges for precipitation estimation in mountainous regions. *Proceedings, 2nd European Conference on Radar Meteorology and Hydrology*, Delft, Netherlands, ERAD.

Gong, J., and L. Wang, 2003: A three-step dealiasing method for Doppler velocity data quality control. *J. Atmos. Oceanic Technol.*, **20**, 1738–1748.

Gourley, J. J., P. Tabary, and J. Parent du Chatelet, 2007: A fuzzy logic algorithm for the separation of precipitating from nonprecipitating echoes using polarimetric radar observations. *J. Atmos. Oceanic Technol.*, **24 (8)**, 1439–1451.

Guo, H., 2011: A simple algorithm for fitting a Gaussian function. *IEEE Signal Process. Mag.*, **28 (5)**, 134–137.

Haase, G., and T. Landelius, 2004: Dealiasing of Doppler radar velocities using a torus mapping. *J. Atmos. Oceanic Technol.*, **21**, 1566–1573.

Hampel, F. R., E. M. Ronchetti, P. J. Rousseeuw, and W. A. Stahel, 1986: *Robust Statistics. The Approach Based on Influence Functions.* 1st ed., John Wiley and Sons, New York, 511 pp.

Hengstebeck, T., D. Heizenreder, and P. Joe, 2014: Detection of atmospheric rotation by means of the DWD radar network. *Proceedings, 8th European Conference on Radar Meteorology and Hydrology*, Garmisch-Partenkirchen, Germany, ERAD.

Hitschfeld, W., and J. Bordan, 1954: Errors inherent in the radar measurement of rainfall at attenuating wavelengths. *J. Meteor.*, **11 (1)**, 58–67.

Holleman, I., 2005: Quality control and verification of weather radar wind profiles. *J. Atmos. Oceanic Technol.*, **22 (10)**, 1541–1550.

Holleman, I., and H. Beekhuis, 2003: Analysis and correction of dual PRF velocity data. *J. Atmos. Oceanic Technol.*, **20**, 443–453.

Holleman, I., and H. Beekhuis, 2004: Weather radar monitoring using the Sun. KNMI Tech. Rep. TR-272, Royal Netherlands Meteorological Institute, 40 pp.

Holleman, I., G. Galli, B. Urban, and D. Michelson, 2003: Definition of product quality descriptors. OPERA project 1c3 working document WD_05_02, OPERA-EUMETNET, 23 pp.

Holleman, I., and A. Huuskonen, 2013: Analytical formulas for refraction of radiowaves from exoatmospheric sources. *Radio Sci.*, **48 (3)**, 226–231.

Holleman, I., A. Huuskonen, R. Gill, and P. Tabary, 2010a: Operational monitoring of radar differential reflectivity using the Sun. *J. Atmos. Oceanic Technol.*, **27**, 881–887.

Holleman, I., A. Huuskonen, M. Kurri, and H. Beekhuis, 2010b: Operational monitoring of weather radar receiving chain using the Sun. *J. Atmos. Oceanic Technol.*, **27**, 159–166.

Holleman, I., D. Michelson, G. Galli, U. Germann, M. Peura, and H. Hohti, 2006: Quality information for radars and radar data. OPERA workpackage 1.2 $\mathrm{OPERA}_2005_19, OPERA - EUMETNET, 77pp.$

Homar, V., M. Gaya, R. Romero, C. Ramis, and S. Alonso, 2003: Tornadoes over complex terrain: an analysis of the 28th August 1999 tornadic event in eastern Spain. *Atmos. Res.*, **67**, 301–317.

Horváth, Z., and D. Varga, 2009: Elimination of RLAN interference on weather radars by channel allocation in 5 GHz band. *8th International Conference on Ultra Modern Telecommunications Workshops*, St. Petersburg, Russia, IEEE, 1–6.

Huuskonen, A., 2001: A method for monitoring the calibration and pointing accuracy of a radar network. *Preprints, 30th Conference on Radar Meteorology*, Munich, Germany, Amer. Meteor. Soc., 29–31.

Huuskonen, A., H. Hohti, T. Kuitunen, and M. Kurri, 2010: The use of the solar monitoring data to assess the quality and the stability of weather radar antenna systems. *TECO-2010, WMO Technical Conference on Meteorological and Environmental Instruments and Methods of Observation*, Helsinki, Finland, World Meteorological Organization, 6.

Huuskonen, A., and I. Holleman, 2007: Determining weather radar antenna pointing using signals detected from the Sun at low antenna elevations. *J. Atmos. Oceanic Technol.*, **24 (3)**, 476–483.

Huuskonen, A., M. Kurri, H. Hohti, H. Beekhuis, H. Leijnse, and I. Holleman, 2014: Radar performance monitoring using the angular width of the solar image. *J. Atmos. Oceanic Technol.*, **31**, 1704–1712.

Huuskonen, A., M. Kurri, and I. Holleman, 2016: Improved analysis of solar signals for differential reflectivity monitoring. *Atmos. Meas. Tech. Discuss.*, accepted for publication.

Huuskonen, A., M. Kurri, and J. Koistinen, 2009: Harmonized production practices for volume data, low level reflectivity and weather radar wind profile. OPERA-3 Deliverable OPERA_2008_06, OPERA-EUMETNET, 54 pp.

Iguchi, T., T. Kozu, R. Meneghini, J. Awaka, and K. Okamoto, 2000: Rain-profiling algorithm for the TRMM precipitation radar. *J. Appl. Meteor.*, **39 (12)**, 2038–2052.

Illingworth, A., 2003: Improved precipitation rates and data quality by using polarimetric measurements. *Weather Radar: Principles and advanced applications*, Springer, 130–166.

James, C. N., and R. A. J. Houze, 2001: A real-time four-dimensional Doppler dealiasing scheme. *J. Atmos. Oceanic Technol.*, **18**, 1674–1683.

Jing, Z., and G. Wiener, 1992: Two-dimensional dealiasing of Doppler velocities. *J. Atmos. Oceanic Technol.*, **10**, 798–808.

Joe, P., S. J, J. Sydor, A. Brandão, and A. Yongacoglu, 2005: Radio Local Area Network (RLAN) and C-Band weather radar interference studies. *Preprints, 32nd Conference on Radar Meteorology*, Albuquerque, NM, Amer. Meteor. Soc., 1–9.

Joe, P., and P. T. May, 2003: Correction of dual PRF errors for operational weather radars. *J. Atmos. Oceanic Technol.*, **20**, 429–442.

Joe, P., and Coauthors, 2012: Automated processing of Doppler radar data for severe weather warnings. *Doppler Radar Observations - Weather Radar, Wind Profiler, Ionospheric Radar, and Other Advanced Applications*, J. Bech, and J. L. Chau, Eds., InTech, 333–354.

Johnson, S. G., and B. Narasimhan, 2015: *Adaptive multivariate integration over hypercubes*. R Foundation for Statistical Computing, URL http://ab-initio.mit.edu/wiki/index.php/Cubature.

Jorgensen, D. P., T. R. Shepherd, and A. S. Goldstein, 2000: A dual-pulse repetition frequency scheme for mitigating velocity ambiguities of the NOAA P-3 airborne doppler radar. *J. Atmos. Oceanic Technol.*, **17**, 586–594.

Keränen, R., L. Rojas, and P. Nyberg, 2013: Progress in mitigation of WLAN interference at weather radar. *Preprints, 36nd Conference on Radar Meteorology*, Breckenridge, CO, Amer. Meteor. Soc.

Kirstetter, P.-E., G. Delrieu, B. Boudevillain, and C. Obled, 2010: Toward an error model for radar quantitative precipitation estimation in the Cévennes-Vivarais region, France. *J. Hydrol.*, **394 (1)**, 28–41.

Kirstetter, P.-E., and Coauthors, 2012: Toward a framework for systematic error modeling of spaceborne precipitation radar with NOAA/NSSL ground radar-based national mosaic QPE. *J. Hydrometeor.*, **13 (4)**, 1285–1300.

Kitchen, M., and P. M. Jackson, 1993: Weather radar performance at long range - simulated and observed. *J. Appl. Meteor.*, **32 (5)**, 975–985.

Köck, K., T. Leltne, W. Randeu, M. Divjak, and K.-J. Schrelber, 2000: OPERA: operational programme for the exchange of weather radar information. First results and outlook for the future. *Physics and Chemistry of the Earth, Part B: Hydrology, Oceans and Atmosphere*, **25 (10)**, 1147–1151.

Koistinen, J., D. B. Michelson, H. Hohti, and M. Peura, 2004: Operational measurement of precipitation in cold climates. *Weather Radar: Principles and advanced applications*, Springer, 78–114.

Kunkel, K. E., R. A. Pielke Jr, and S. A. Changnon, 1999: Temporal fluctuations in weather and climate extremes that cause economic and human health impacts: A review. *Bull. Amer. Meteor. Soc.*, **80 (6)**, 1077.

Lakshmanan, V., A. Fritz, T. Smith, K. Hondl, and G. Stumpf, 2007: An automated technique to quality control radar reflectivity data. *J. Climate Appl. Meteor.*, **46 (3)**, 288–305.

Lakshmanan, V., T. Smith, K. Hondl, G. J. Stumpf, and A. Witt, 2006: A real-time, three-dimensional, rapidly updating, heterogeneous radar merger technique for reflectivity, velocity, and derived products. *Wea. Forecasting*, **21 (5)**, 802–823.

Lehtinen, M. S., 2001: Method and system for measuring radar reflectivity and doppler shift by means of a pulse radar. United States Patent and Trademark Office (USPTO), U.S. Patent No. 6232913.

Leskinen, M., P. Puhakka, and T. Puhakka, 2002: A method for estimating antenna beam parameters using the Sun. *Proceedings, 2nd European Conference on Radar Meteorology and Hydrology*, Delft, Netherlands, ERAD, 318–323.

List, R., 1988: A linear radar reflectivity-rain rate relationship for steady tropical rains. *J. Atmos. Sci.*, **45**, 3564–3572.

Llasat, M., M. Llasat-Botija, O. Petrucci, A. Pasqua, J. Rosselló, F. Vinet, and L. Boissier, 2013: Towards a database on societal impact of Mediterranean floods within the framework of the HYMEX project. *Nat. Hazards Earth Syst. Sci.*, **13 (5)**, 1337–1350.

Llasat, M.-C., M. Barriendos, A. Barrera, and T. Rigo, 2005: Floods in Catalonia (NE Spain) since the 14th century. Climatological and meteorological aspects from historical documentary sources and old instrumental records. *J. Hydrol.*, **313 (1)**, 32–47.

Llasat, M. C., R. Marcos, M. Turco, J. Gilabert, and M. Llasat-Botija, 2016: Trends in flash flood events versus convective precipitation in the Mediterranean region: The case of Catalonia. *J. Hydrol.*, in press.

Macpherson, B., and Coauthors, 2004: Assimilation of radar data in numerical weather prediction (NWP) models. *Weather Radar*, Springer, 255–279.

Magaldi, A. V., J. Bech, and J. Lorente, 2009: A multisource scheme based on NWP and MSG data to correct non-precipitating weather radar echoes. *Meteorol. Atmos. Phys.*, **105 (3-4)**, 121–132.

Manz, A., A. H. Smith, and P. J. Hardaker, 2000: Comparison of different methods of end-to-end calibration of the UK weather radar network. *Phys. Chem. Earth.*, **25**, 1157–1162.

Marshall, J. S., and W. M. Palmer, 1948: The distribution of raindrops with size. *J. Meteorol.*, **5**, 165–166.

Mateo, J., D. Ballart, C. Brucet, M. Aran, and J. Bech, 2009: A study of a heavy rainfall event and a tornado outbreak during the passage of a squall line over Catalonia. *Atmos. Res.*, **93 (1)**, 131–146.

May, P. T., 2001: Mesocyclone and microburst signature distortion with dual-PRT radar. *J. Atmos. Oceanic Technol.*, **18**, 1229–1233.

Meischner, P., 2004: *Weather radar: principles and advanced applications*. Springer Science & Business Media.

Meneghini, R., J. A. Jones, T. Iguchi, K. Okamoto, and J. Kwiatkowski, 2004: A hybrid surface reference technique and its application to the TRMM precipitation radar. *J. Atmos. Oceanic Technol.*, **21 (11)**, 1645–1658.

Meneghini, R., T. Kozu, H. Kumagai, and W. C. Boncyk, 1992: A study of rain estimation methods from space using dual-wavelength radar measurements at near-nadir incidence over ocean. *J. Atmos. Oceanic Technol.*, **9 (4)**, 364–382.

Michelson, D., T. Einfalt, I. Holleman, U. Gjertsen, K. Friedrich, G. Haase, M. Lindskog, and A. Jurczyk, 2004: Weather radar data quality in Europe: Quality control and characterization. COST-717 Working Document WDF_MC_200403_1, European Co-Operation in the field of Scientific and Technical research (COST), 92 pp.

Miller, L. J., C. G. Mohr, and A. J. Weinheimer, 1986: The simple rectification to Cartesian space of folded radial velocities from Doppler radar sampling. *J. Atmos. Oceanic Technol.*, **3**, 162–174.

Miller, L. M., V. Lakshmanan, and T. M. Smith, 2013: An automated method for depicting mesocyclone paths and intensities. *Wea. Forecasting*, **28**, 570–585.

Mitchell, E. D. W., S. V. Vasiloff, G. J. Stumpf, A. Witt, M. D. Eilts, J. T. Johnson, and K. W. Thomas, 1998: The national severe storms laboratory tornado detection algorithm. *Wea. Forecasting*, **13 (2)**, 352–366.

Moore, R. J., V. A. Bell, and D. A. Jones, 2005: Forecasting for flood warning. *Comptes Rendus Geoscience*, **337 (1)**, 203–217.

Muth, X., M. Schneebeli, and A. Berne, 2012: A sun-tracking method to improve the pointing accuracy of weather radar. *Atmos. Meas. Tech.*, **5**, 547–555.

Norin, L., and G. Haase, 2012: Doppler weather radars and wind turbines. *Doppler Radar Observations - Weather Radar, Wind Profiler, Ionospheric Radar, and Other Advanced Applications*, J. Bech, and J. L. Chau, Eds., InTech, 333–354.

Norman, K., N. Gaussiat, D. Harrison, R. Scovell, and M. Boscacci, 2010: A quality index for radar data. *OPERA deliverable OPERA_2010_03*.

NRC, 2010: *When weather matters: Science and service to meet critical societal needs*. National Academies Press, 198 pp., [Available online at http://www.nap.edu/read/12888/chapter/1].

OPERA, 1999: Operational programme for the exchange of weather radar information - EIG EUMETNET website. http://www.eumetnet.eu/opera.

Ośródka, K., and J. Szturc, 2015: Quality-based generation of weather radar cartesian products. *Atmos. Meas. Tech.*, **8 (5)**, 2173–2181.

Ośródka, K., J. Szturc, and A. Jurczyk, 2014: Chain of data quality algorithms for 3-D single-polarization radar reflectivity (RADVOL-QC system). *Meteor. Appl.*, **21 (2)**, 256–270.

Peura, M., 2002: Computer vision methods for anomaly removal. *Proceedings, 2nd European Conference on Radar Meteorology and Hydrology*, Delft, Netherlands, ERAD, 312–317.

Peura, M., J. Koistinen, and H. Hohti, 2006: Quality information in processing weather radar data for varying user needs. *Proceedings, 4th European Conference on Radar Meteorology and Hydrology*, Barcelona, Spain, ERAD.

Pierce, C., A. Seed, S. P. Ballard, D. Simonin, and Z. Li, 2012: Nowcasting. *Doppler Radar Observations - Weather Radar, Wind Profiler, Ionospheric Radar, and Other Advanced Applications*, J. Bech, and J. L. Chau, Eds., InTech, 97–142.

Pierce, C., and Coauthors, 2004: The nowcasting of precipitation during Sydney 2000: an appraisal of the QPF algorithms. *Wea. Forecasting*, **19 (1)**, 7–21.

Pineda, N., J. Bech, T. Rigo, and J. Montanyà, 2011: A Mediterranean nocturnal heavy rainfall and tornadic event. Part II: Total lightning analysis. *Atmos. Res.*, **100**, 638–648.

Pineda, N., J. Bech, T. Rigo, and L. Trapero, 2006: Comparison of radar precipitation fields with lightning observations. *Proceedings, 4th European Conference on Radar Meteorology and Hydrology*, Barcelona, Spain, ERAD.

Pirtillä, J., M. S. Lehtinen, A. Huuskonen, and M. Markkanen, 2005: A proposed solution to the range-Doppler dilemma of weather radar measurements by using the SMPRF codes, practical results, and a comparison with operational measurements. *J. Appl. Meteor.*, **44**, 1375–1390.

Pratt, J. F., and D. G. Ferraro, 1989: Automated solar gain calibration. *Preprints, 24th Conference on Radar Meteorology*, Tallahassee, US-FL, Amer. Meteor. Soc., 619–622.

Probert-Jones, J. R., 1962: The radar equation in meteorology. *Quart. J. Roy. Meteor. Soc.*, **88 (378)**, 485–495.

Python, 2001: Python language reference. Python Software Foundation, [https://www.python.org/].

R Core Team, 2016: *R: A Language and Environment for Statistical Computing*. Vienna, Austria, R Foundation for Statistical Computing, URL https://www.R-project.org/.

Ray, P. S., and C. Ziegler, 1977: De-aliasing first-moment Doppler estimates. *J. Appl. Meteor.*, **16**, 563–564.

Reimann, C., P. Filzmoser, R. G. Garrett, and R. Dutter, 2008: *Statistical data analysis explained: Applied environmental statistics with R*. 3rd ed., John Wiley and Sons Ltd, 362 pp.

Ricard, D., V. Ducrocq, and L. Auger, 2012: A climatology of the mesoscale environment associated with heavily precipitating events over a northwestern Mediterranean area. *J. Climate Appl. Meteor.*, **51 (3)**, 468–488.

Rico-Ramírez, M. A., E. González-Ramírez, I. Cluckie, and D. Han, 2009: Real-time monitoring of weather radar antenna pointing using digital terrain elevation and a Bayes clutter classifier. *Meteor. Appl.*, **16**, 227–236.

Rigo, T., and M. C. Llasat, 2016: Forecasting hailfall using parameters for convective cells identified by radar. *Atmos. Res.*, **169**, 366–376.

Rigo, T., N. Pineda, and J. Bech, 2010: Analysis of warm season thunderstorms using an object-oriented tracking method based on radar and total lightning data. *Nat. Hazards Earth Syst. Sci.*, **10 (9)**, 1881–1893.

Rinehart, R. E., 1997: *Radar for Meteorologists*. Rinehart Publications, Grand Forks, USA, 428 pp.

Roca-Sancho, J., M. Berenguer, and D. Sempere-Torres, 2014: An inverse method to retrieve 3D radar reflectivity composites. *J. Hydrol.*, **519**, 947–965.

Rojas, L. C., D. Moisseev, V. Chandrasekar, J. Sezler, and R. Keränen, 2012: Dual-polarization spectral filter for radio frequency interference suppression. *Proceedings, 7th European Conference on Radar Meteorology and Hydrology*, Toulouse, France, ERAD.

Rossa, A. M., 2000: COST-717: Use of radar observations in hydrological and NWP models. *Phys. Chem. Earth, Part B: Hydrology, Oceans and Atmosphere*, **25 (10)**, 1221–1224.

Sachidananda, M., and D. S. Zrnić, 1999: Systematic phase codes for resolving range overlaid signals in a doppler weather radar. *J. Atmos. Oceanic Technol.*, **16**, 1351–1363.

Sachidananda, M., and D. S. Zrnić, 2000: Clutter filtering and spectral moment estimation for Doppler weather radars using staggered Pulse Repetition Time (PRT). *J. Atmos. Oceanic Technol.*, **17**, 323–331.

Saltikoff, E., J. Y. N. Cho, P. Tristant, A. Huuskonen, L. Allmon, R. Cook, E. Becker, and P. Joe, 2016: The threat to weather radars by wireless technology. *Bull. Amer. Meteor. Soc.*, in press.

Saltikoff, E., A. Huuskonen, H. Hohti, J. Koistinen, and H. Järvinen, 2010: Quality assurance in the FMI Doppler weather radar network. *Boreal Environ. Res.*, **15 (6)**, 579–594.

Sánchez-Diezma, R., 2001: Optimización de la medida de lluvia por radar meteorológico para su aplicación hidrológica. Ph.D. thesis, Centre de Recerca Aplicada en Hidrometeorologia, Universitat Politecnica de Catalunya, 330 pp., [Available online at http://www.crahi.upc.edu/en/publications/others/118-tesis].

Sánchez-Diezma, R., D. Sempere-Torres, J. Bech, and E. Velasco, 2002: Development of a hydrometeorological flood warning system (EHIMI) based on radar data. *Proceedings, 2nd European Conference on Radar Meteorology and Hydrology (ERAD)*, Delft, Netherlands, 619–622.

Sánchez-Diezma, R., D. Sempere-Torres, G. Delrieu, and I. Zawadzki, 2001: An improved methodology for ground clutter substitution based on a pre-classification of precipitation types. *Proceedings, 30th International Conference on Radar Meteorology*, Munich, Germany, 271–273.

Sancho Alcázar, D., 2009: Implementació del mòdul d'anàlisi de funcionament de radar. B.S. Thesis, Universitat Politècnica de Catalunya, Barcelona, [Available online at http://upcommons.upc.edu/handle/2099.1/6873].

Sandford, C., and N. Gaussiat, 2011: Evaluation of an error-based quality index for compositing using UK radar data. *OPERA deliverable OPERA_2011_12*.

Schneider, U., A. Becker, P. Finger, A. Meyer-Christoffer, M. Ziese, and B. Rudolf, 2014: GPCC's new land surface precipitation climatology based on quality-controlled in situ data and its role in quantifying the global water cycle. *Theor. Appl. Climatol.*, **115 (1-2)**, 15–40.

Sempere-Torres, D., R. Sánchez-Diezma, M. Berenguer, R. Pascual, and I. Zawadzki, 2003: Improving radar rainfall measurement stability using mountain returns in real time. *Preprints, 31st Int. Conf. on Radar Meteorology, Seattle, WA, Amer. Meteor. Soc.*, 220–221.

Silberstein, D. S., D. B. Wolff, D. A. Marks, D. Atlas, and J. L. Pippitt, 2008: Ground clutter as a monitor of radar stability at Kwajalein, RMI. *J. Atmos. Oceanic Technol.*, **25 (11)**, 2037–2045.

Sirmans, D., D. Zrnić, and B. Bumgarner, 1976: Extension of maximum unambiguous Doppler velocity by use of two sampling rates. *Preprints, 17th Conference on Radar Meteorology*, Seattle, US-WA, Amer. Meteor. Soc., 23–28.

Skolnik, M. I., 1980: *Introduction to radar systems.* McGraw-Hill, New York.

Smith, J. A., and W. F. Krajewski, 1993: A modeling study of rainfall rate-reflectivity relationships. *Water Resour. Res.*, **29**, 2505–2514.

Smith, T. M., K. L. Elmore, and S. A. Dulin, 2004: A damaging downburst prediction and detection algorithm for the WSR-88D. *Wea. Forecasting*, **19 (2)**, 240–250.

Soriano Romero, J. d. D., J. Á. Núñez Mora, C. Jiménez Alonso, F. Polvorinos Pascual, and J. Riesco Martín, 2015: Climatología de tornados en España Peninsular y Baleares.

Steiner, M., J. A. Smith, S. J. Burges, C. V. Alonso, and R. W. Darden, 1999: Effect of bias adjustment and rain gauge data quality control on radar rainfall estimation. *Water Resour. Res.*, **35 (8)**, 2487–2503.

Stensrud, D. J., and Coauthors, 2009: Convective-scale warn-on-forecast system: A vision for 2020. *Bull. Amer. Meteor. Soc.*, **90**, 1487–1499.

Stumpf, G. J., A. Witt, E. D. Mitchell, P. L. Spencer, J. T. Johnson, M. D. Eilts, K. W. Thomas, and D. W. Burgess, 1998: The National Severe Storms Laboratory Mesocyclone Detection Algorithm for the WSR-88D. *Wea. Forecasting*, **13 (2)**, 304–326.

Sun, J., 2005: Convective-scale assimilation of radar data: progress and challenges. *Quart. J. Roy. Meteor. Soc.*, **131 (613)**, 3439–3463.

Sun, J., and N. A. Crook, 2001: Real-time low-level wind and temperature analysis using single WSR-88D data. *Wea. Forecasting*, **16**, 117–132.

Szturc, J., K. Ośródka, and A. Jurczyk, 2011: Quality index scheme for quantitative uncertainty characterization of radar based precipitation. *Meteor. Appl.*, **18 (4)**, 407–420.

Tabary, P., F. Guibert, L. Perier, and J. Parent-Du-Chatelet, 2006: An operational triple-PRT Doppler scheme for the French radar network. *J. Atmos. Oceanic Technol.*, **23**, 1645–1656.

Tapping, K., 2001: Antenna calibration using the 10.7cm solar flux. *Workshop on Radar Calibration*, Albuquerque, US-NM, Amer. Meteor. Soc., 1–32.

Torres, D. S., J. M. Porrà, and J. D. Creutin, 1998: Experimental evidence of a general description for raindrop size distribution properties. *J. Geophys. Res.*, **103**, 1785–1797.

Torres, S. M., Y. F. Dubel, and D. S. Zrnic, 2004: Design, implementation, and demonstration of a staggered PRT algorithm for the WSR-88D. *J. Atmos. Oceanic Technol.*, **21 (9)**, 1389–1399.

Trapero, L., J. Bech, T. Rigo, N. Pineda, and D. Forcadell, 2009: Uncertainty of precipitation estimates in convective events by the meteorological service of catalonia radar network. *Atmospheric Research*, **93 (1)**, 408–418.

Trenberth, K. E., 2011: Changes in precipitation with climate change. *Climate Res.*, **47 (1-2)**, 123–138.

Uijlenhoet, R., 2001: Raindrop size distributions and radar reflectivity-rain rate relationships for radar hydrology. *Hydrol. Earth Syst. Sci.*, **5**, 615–627.

Vaisala, 2014a: Suncal utility. *UTILITIES MANUAL: IRIS and RDA*, Vaisala Oyj, chap. 11, 251–264.

Vaisala, 2014b: *USER'S MANUAL: Digital IF receiver/Doppler signal processor, RVP8.* Helsinki, Finland, Vaisala Oyj.

Vaisala, 2014c: *USER'S MANUAL: Radar Control Processor, RCP8.* Helsinki, Finland, Vaisala Oyj.

Vega, M. A., V. Chandrasekar, C. Nguyen, K. V. Mishra, and J. Carswell, 2012: Calibration of the NASA dual-frequency, dual-polarized, doppler radar. *International Geoscience and Remote Sensing Symposium (IGARSS)*, Munich, Germany, IEEE Geoscience and Remote Sensing Society, 4625–4628.

Velasco-Forero, C. A., D. Sempere-Torres, E. F. Cassiraga, and J. J. Gómez-Hernández, 2009: A non-parametric automatic blending methodology to estimate rainfall fields from rain gauge and radar data. *Adv. Water Resour.*, **32 (7)**, 986–1002.

Villarini, G., and W. F. Krajewski, 2010: Review of the different sources of uncertainty in single polarization radar-based estimates of rainfall. *Surv. Geophys.*, **31 (1)**, 107–129.

Vivoni, E. R., D. Entekhabi, R. L. Bras, V. Y. Ivanov, M. P. Van Horne, C. Grassotti, and R. N. Hoffman, 2006: Extending the predictability of hydrometeorological flood events using radar rainfall nowcasting. *J. Hydrometeor.*, **7 (4)**, 660–677.

Vulpiani, G., P. Tabary, J. Parent du Chatelet, and F. S. Marzano, 2008: Comparison of advanced radar polarimetric techniques for operational attenuation correction at C band. *J. Atmos. Oceanic Technol.*, **25 (7)**, 1118–1135.

Waldteufel, P., and H. Corbin, 1979: On the analysis of single-doppler radar data. *J. Appl. Meteor.*, **18 (4)**, 532–542.

Wapler, K., T. Hengstebeck, and P. Groenemeijer, 2016: Mesocyclones in central europe as seen by radar. *Atmos. Res.*, **168**, 112–120.

Whiton, R. C., P. L. Smith, and A. C. Harbuck, 1976: Calibration of weather radar systems using the Sun as a radio source. *Preprints, 17th Conference on Radar Meteorology*, Seattle, US-WA, Amer. Meteor. Soc., 60–65.

Wilson, J. W., and E. A. Brandes, 1979: Radar measurement of rainfall - a summary. *Bull. Amer. Meteor. Soc.*, **60 (9)**, 1048–1058.

WMO, 2008: Measurement of radiation; useful formulae. *Guide to meteorological instruments and methods of observation - WMO No.8*, 7th ed., Publications Board, World Meteorological Organization, 37–38.

Xu, Q., K. Nai, L. Wei, P. Zhang, S. Liu, and D. Parrish, 2010: A VAD-based dealiasing method for radar velocity data quality control. *J. Atmos. Oceanic Technol.*, **28**, 50–62.

Yatagai, A., K. Kamiguchi, O. Arakawa, A. Hamada, N. Yasutomi, and A. Kitoh, 2012: APHRODITE: Constructing a long-term daily gridded precipitation dataset for Asia based on a dense network of rain gauges. *Bull. Amer. Meteor. Soc.*, **93 (9)**, 1401–1415.

Zawadzki, I., 1984: Factors affecting the precision of radar measurements of rain. *Conference on Radar Meteorology, 22 nd, Zurich, Switzerland*, 251–256.

Zrnič, D. S., and R. J. Doviak, 1976: Effective antenna pattern of scanning radars. *IEEE Trans. Aer. Electronic Systems*, **12**, 551–555.

Zrnic, D. S., and A. V. Ryzhkov, 1999: Polarimetry for weather surveillance radars. *Bulletin of the American Meteorological Society*, **80 (3)**, 389.

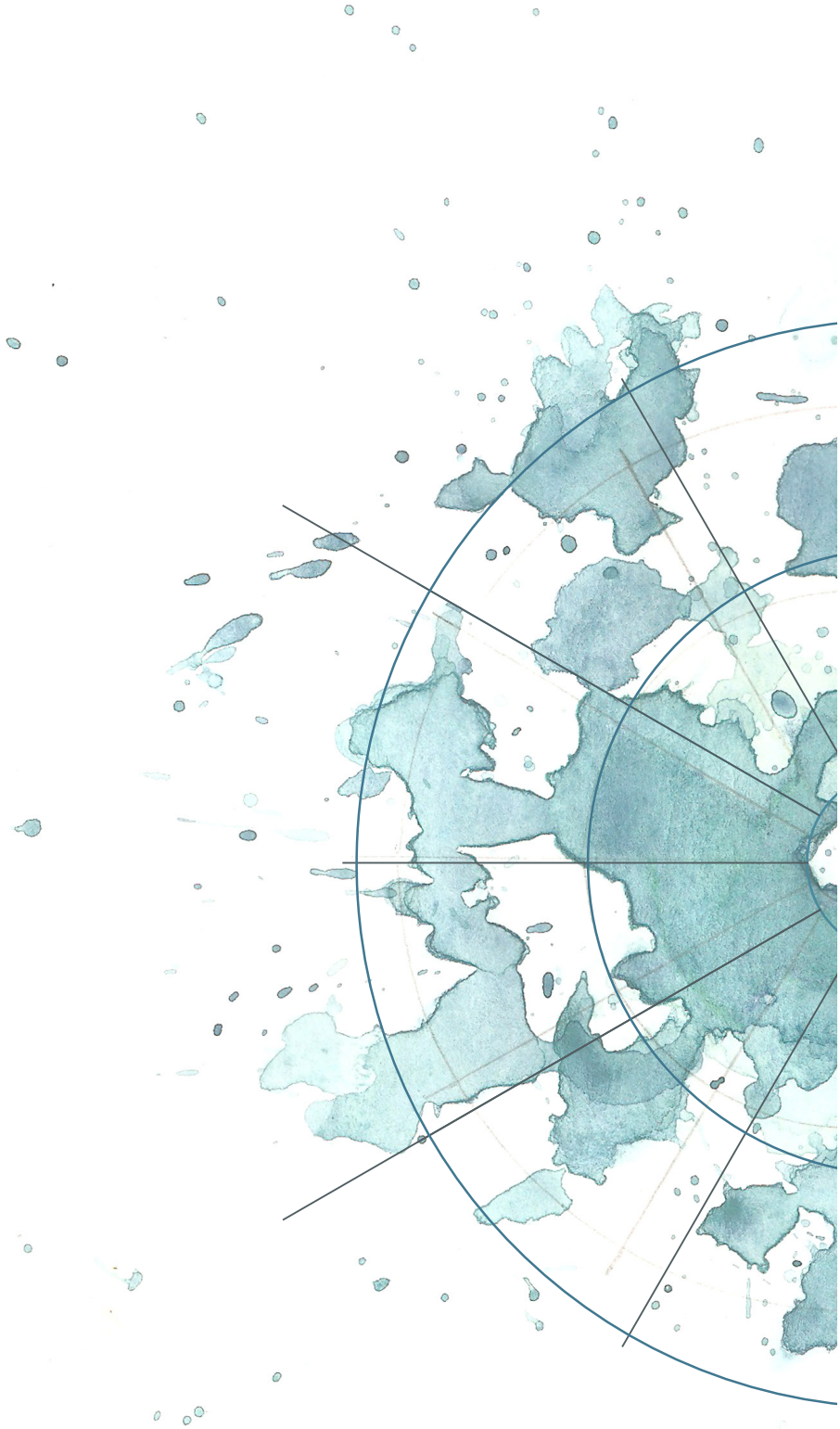

meteo.cat

Universitat de Barcelona

Generalitat de Catalunya